NON CONTACT MECHANICAL TESTING AT HIGH TEMPERATURE USING ELECTROMAGNETIC FORCES

by

Sindhura Gangireddy

A dissertation submitted in partial fulfillment
of the requirements for the degree of
Doctor of Philosophy
(Materials Science and Engineering)
in The University of Michigan
2012

Doctoral Committee:

Professor John W. Halloran, Chair
Professor Anthony M. Waas
Associate Professor Anton Van der Ven
Assistant Professor Samantha Daly

To my parents and sister-
For your love, support and encouragement.

Acknowledgements

Aided by a Subcontract from Advanced Ceramic Manufacturing, Tucson, AZ from
American Air Force Office of Scientific Research
Research STTR Contract

TABLE OF CONTENTS

LIST OF FIGURES

LIST OF TABLES

CHAPTER 1

INTRODUCTION

1.1. Motivation and Outline of the Thesis

This research concerns the development of a new non-contact mechanical testing technique that loads specimens using electromagnetic Lorentz force. This new method, called Electro Magnetic Mechanical Apparatus (EMMA), can be used for any electrically conductive material, and is particularly appropriate for very high temperature testing of brittle materials like ceramics for which conventional testing is difficult.

Conventional mechanical testing procedures for ductile materials are typically conducted in tension or compression, but brittle materials are typically tested in flexure (3-pt or 4-pt). Carried out using a loading fixture set up inside a furnace, these procedures face temperature limitations due to the operating temperature limit of the furnace and loading fixtures. Further problems arise from contamination reactions at the location of contact of the loading fixtures with the material at high temperatures.

Materials like Ultra High Temperature Ceramics (UHTCs) (discussed in more detail in the next subsection 1.2) are intended for application in extreme environments where the temperature can exceed 2000 °C. These materials cannot be easily tested with standard procedures at their expected use temperatures. Thus their mechanical properties are usually determined at lower temperatures, and only extrapolations to high temperatures are available for designers.

Another limitation with these methods is the long time duration of the test. The furnaces can allow only slow heating and cooling rates. To reach high temperatures, the ramp-up time and the ramp-down time are typically of the order of hours. The total time of a high temperature test, for example a creep experiment can take an entire day. In addition, the slow heating time to the target temperature is itself a heat treatment process and can affect the material properties.

There has been interest in developing new mechanical testing techniques to address these issues, especially non-contact methods that overcome the temperature limitation. Our research was aimed towards this goal of developing a mechanical testing procedure which is non-contact in nature and can operate at ultra high temperatures > 2500 °C. The successful development of EMMA allows experiments with short test durations (on the order of minutes) that can be conducted in an easily operable inexpensive table top apparatus. This dissertation details the working principles and theory of EMMA, the design and fabrication of the apparatus, and results from creep testing of Zirconium Diboride – Silicon Carbide composites.

The subsequent sections in Chapter 1 give a brief introduction to UHTCs and describe how EMMA is particularly beneficial for these materials, cover generic creep test results and characteristics, and discuss possible creep deformation mechanisms in ceramics. Also included is a literature review of creep studies and other high temperature properties of UHTCs using conventional testing procedures. The last subsection explains the ribbon method of resistive heating and how we utilize this method in our technique EMMA.

Chapter 2 introduces the EMMA technique and the use of electromagnetic forces for mechanical testing. The correlation of the operating variables of the test (temperature and stress) to the directly controllable experimental variables in this technique (current and magnetic field) is discussed.

Chapter 3 details the EMMA apparatus and the functions of the different equipment employed. The first prototype, made by simple modification of the ribbon method, demonstrated the feasibility of the technique. Later, a more complex apparatus with multiple components was designed using CAD and assembled from externally manufactured equipment. A comparison and justification of each component with the other available options is presented.

Chapter 4 explores the electromagnetic Lorentz forces that can be generated using EMMA and analyzes the resultant stresses from it. An interesting outcome of using

Lorentz forces is the dynamic evolution of stress state with continuing deformation. Finite Element Method is usedowing to the complexity of analyzing these ever changing stress and resultant creep deformations. The deflection profile of the deforming ribbon is simulated and can be compared with the empirical results to obtain the relevant mechanical properties.

Chapter 5 presents the results from high temperature creep experiments performed using EMMA on the UHTC ZrB2-SiC composite from 1700 °C to 2200 °C. The kinetic parameters of creep – Activation Energy and Stress Exponent- are derived in this temperature range and are used to infer the deformation mechanism in creep. This creep data from EMMA is compared to the literature data from conventional testing.

Chapter 6 is composed of observations from microstructure of the post creep ZrB2-SiC UHTC material. The effect of oxidation during ultra high temperature testing, discoveries from investigations for evidence of grain deformations and damage in the interior are presented.

Chapter 7 concludes the dissertation with possible future applications of EMMA for extending its use for other high temperature mechanical tests such as fatigue, fast fracture and modulus. It also explores the applicability of this technique to test other high temperature materials including most UHTCs and several high temperature metals.

1.2 Ultra High Temperature Ceramics

Ultra High Temperature Ceramics (UHTCs) are the materials for which this technique is originally invented. UHTCs are a broad class of refractory materials including transition metal borides, carbides and nitrides e.g. ZrB_2, HfB_2, ZrC, HfC, TaC, HfN and ZrN. They recently captured interest as potential materials to be used in supersonic and hypersonic vehicles as re-usable thermal protection systems and other components [1-2]. The designs of these future generation vehicles incorporate sharp aero-surfaces that require reliability in the extreme re-entry environments, like oxidizing atmospheres, at very high temperatures.

Refractory borides like ZrB_2 and HfB_2 have extremely high melting temperatures (over 3000 °C), along with other desirable properties like high thermal conductivity, high hardness, retained strength and chemical stability at elevated temperatures [3]. But borides are very poor in oxidation resistance, due to the nature of their oxides: Non-protective ZrO_2 or HfO_2 and volatile liquid B_2O_3. Addition of SiC to these materials can greatly improve their oxidation resistance by the formation of a passivating layer of silica on the outer surface. SiC addition has also been found improve densification during sintering, thermal shock resistance [4-9] and room temperature strength without sacrificing high temperature strength [10]. HfB_2 has a slightly higher melting point, but ZrB_2 has the additional advantages of a lower theoretical density and better thermal shock resistance. It is less expensive and has high thermal conductivity to allow more energy to be

conducted away [4]. Therefore ZrB_2-SiC has been considered a potential UHTC candidate for these applications.

The UHTCs can also operate as structural components for a range of other short and long lifetime applications. Short lifetime applications include weapons system components such as rocket nozzles, nosetips, and leading edges for hypersonic missiles and hypersonic flight vehicles. The long lifetime applications include turbine, missile launchers, guns, and others. [11] Despite intense recent research efforts, UHTCs are still far from being used routinely as hypersonic aero-surfaces because some do not have the required set of properties, and in others the microstructure-processing property relationship is still not well understood. The latter is particularly true of the high-temperature mechanical properties in the creep and pre-creep regimes. Most studies on UHTCs have centered on investigating lower temperature sintering, resistance to oxidation and thermal shock, and room temperature mechanical properties. [12-18]

Both non-eroding rocket nozzles and sharp leading edges for hypersonic vehicles require materials that will survive service conditions over 2200 °C for minutes to hours. Meeting these needs will require significant improvements in our fundamental understanding of the response of materials at such high temperatures, especially their resistance to creep. However, conventional methods for measuring creep of these materials have severe limitations that often restrict designers to extrapolating properties from lower-temperature tests. [11,19] EMMA is therefore particularly designed for

mechanical testing of UHTCs at extreme temperatures using non contact loading using electromagnetic Lorentz forces to exploit the fact that UHTCs are metallic conductors.

1.3. Creep at High Temperatures

Apart from the obvious expectation for a high temperature material to be chemically and physically stable at elevated temperatures, it is also required to retain mechanical properties like strength, toughness, and creep-resistance at the intended use temperatures. Creep deformation is one of the important criteria for structural applications at high temperatures, and has to be understood in order to predict material behavior. [11]

Creep is defined as a time-dependent permanent deformation of a material occurring under a stress lower than its yielding stress when subjected to a temperature which is a significant fraction, a rule of thumb for ceramics being 40-50%, of its absolute melting point. Diffusion, which atomic mobility is related to and increases with temperature as given by Norton -Arrhenius Equation [20]:

$$D = D_o e^{-\frac{Q}{RT}} \qquad \text{……. (1)}$$

where D is the diffusion rate, Do is a constant, Q is the activation energy for atomic motion (J/mol), R is the universal gas constant (8.314J/mole K) and T is the absolute temperature. Diffusion-controlled mechanisms like dislocation climb, new slip systems, and grain boundary sliding gain significance at high temperatures and will affect

high temperature mechanical behavior causing slow permanent creep deformation. The deformation mechanisms during creep are discussed in detail in Section 1.4.

Although conceptually a creep test is rather simple, to apply a force to a test specimen and measure its dimensional change over time with exposure to a relatively high temperature, in practice is more complicated. Temperature control, uniformity of the applied stress, resolution and stability of the extensometer all are important concerns and are critical for creep data interpretation. Environmental effects can complicate creep tests by causing premature failures unrelated to elongation and thus must either mimic the actual use conditions or be controlled to isolate the failures to creep mechanisms. Figure 1.1 shows a typical creep testing setup in flexure for ceramics. There are several standard creep testing procedures for advanced ceramics for various testing test conditions including ASTM C1161-90, C 1121-92, C 1341-95. [21]

The basic result of a creep test is the strain versus time curve shown schematically in Figure 1.2. A creep curve measures the resistance of a material to time-dependent deformation under load. The initial strain is simply the elastic response to the applied load (stress). The rest is the creep strain which is inelastic/ permanent. Despite the differences among various creep mechanisms, creep behavior generally can be divided into three stages based on their different creep rate characteristics.

During stage I, the creep rate decreases with time. This is termed primary creep. During Stage II of the curve, the creep rate approaches a stable minimum value which

relatively constant over time. Stage II is called secondary creep or steady-state creep, i.e. $\frac{d\varepsilon}{dt}$ is constant. This steady-state creep rate is an important engineering property, because most deformations are dominated by this – including UHTCs. In stage III, termed tertiary creep, the creep rate accelerates with time due to necking and usually leads to failure by creep rupture. Although the three stages represent the creep behavior in most materials, the primary creep stage can be absent for some materials. The extension during the tertiary creep stage can be limited in brittle materials like ceramics and very extensive in ductile materials like metals.

The creep rate is affected by various factors, such as material properties, temperature, and applied stress. Thus creep is not an intrinsic material response, but a performance based behavior. It is usually of concern when evaluating components that operate under high stresses or high temperatures. Creep Characteristics:

(a) Time

A time scale is always involved in a creep test. The main reason for the time dependence of creep is the involvement of thermally activated time-dependent processes. In certain application designs, the design lives are much longer than the range of the experimental data, which usually goes up to order of thousand hours. In these situations some means of extrapolating the data to long lives is necessary, and a common method of doing this is the use of time-temperature parameters which relate the stress and temperature to the time to failure. The most widely used parameter is the Larson-Miller parameter,

$$\text{L-M Parameter} = T\,[C' + \log t_f] \quad \ldots\ldots\ldots (2)$$

where C' is a constant. C' is approximately equal to 20 when the temperature (T) is expressed in degrees Kelvin and the time (t_f) is expressed in hours. This parameter is plotted against the stress to obtain a master curve of the creep rupture behavior. By knowing the L-M Parameter for a given stress it is possible to determine the time to failure at a given temperature. By running experiments at the design stress, but at a higher temperature, creep rupture will occur in a reasonable length of time, and the L-M Parameter can be found by using the above equation.

(b) Temperature

At high temperatures, the mobility of atoms or vacancies increases rapidly with temperature so that they can diffuse through the lattice of the materials along the direction of the hydrostatic stress gradient, which is called self-diffusion. The self-diffusion of atoms or vacancies can also help dislocations climb (a motion of dislocation toward the direction perpendicular to its slip plane). At low temperatures, creep becomes less diffusion-controlled but can occur in local high mobility areas like grain boundaries and phase interfaces, which is called grain-boundary diffusion. Because creep is strongly temperature dependent, a measurement of the temperature dependence of creep is important. The temperature dependence of steady state creep rate is usually given by an Arrhenius rate equation:

$$\dot{\varepsilon}_{ss} = \dot{\varepsilon}_{min} = c.e^{\left(\frac{-Q}{RT}\right)} \quad \ldots\ldots\ldots (3)$$

where Q is the activation energy for creep, R is the universal gas constant, T is the absolute temperature and c is some constant.

(c) Stress

Creep rate is very sensitive to the applied stress level and stress state. With an increase of applied stress, the primary and secondary (steady state) stages are shortened or even eliminated, and the tertiary stage dominates in the creep process. Different stress states can be used for creep tests and creep rupture tests, such as simple tension, simple compression, simple shear, simple torsion, and in some special cases, multiaxial stresses**.** The difference in the results at the same stress level in simple tension and simple compression indicate the creep rate to the direction of stress. The stress dependence of $\dot{\varepsilon}_{ss}$, at a constant temperature is usually given by a power-law relationship:

$$\dot{\varepsilon}_{ss} = \dot{\varepsilon}_{min} = B.\sigma^{n} \quad \text{……. (4)}$$

where n is the stress exponent, σ is the applied stress. In principle, the creep deformation should be linked to an applied stress. Thus, as the specimen elongates, the cross sectional area decreases, and thus the load needs to be decreased to maintain a constant stress. In practice it is simpler to maintain a constant load and when reporting creep test results the initial applied stress is used. The effect of constant load vs. constant stress only really manifests itself in the tertiary region due to the necking phenomena. However this is beyond the general region of interest, i.e. the secondary region.

(d) Microstructure

Creep properties of materials are intrinsically determined by the microstructure of the materials. Grain size affects creep rate in all three creep stages. Precipitates and impurity particles initiate creep cavities. These microstructural effects can be superimposed and

can affect creep properties of materials in various complex ways. In ceramics, the effect of grain size can be termed by the equation, [23]

$$\dot{\varepsilon}_{ss} = \dot{\varepsilon}_{min} = \left(\frac{b}{d}\right)^{p} \text{ ..... (5)}$$

where b is the burger's vector of the material and d is the grain size and p is the exponent of inverse grain size. Porosity due to sintering is another microstructure effect, particularly in ceramic materials. Both the volume percentage and the shape of the pores directly influence the creep property of ceramic materials. [24] In order to understand the relations between the microstructural effects and the creep properties of materials, the microstructural creep mechanisms are discussed in the next section.

Combining the three factors, a general creep rate equation is given by:

$$\dot{\varepsilon}_{ss} = \dot{\varepsilon}_{min} = A\sigma^{n}.\left(\frac{b}{d}\right)^{p} e^{\left(\frac{-Q}{RT}\right)} \text{ ..... (6)}$$

$$log\ \dot{\varepsilon}_{ss} = log\dot{\varepsilon}_{min} = \log(A) + n.\log(\sigma) - p.log(d) - \frac{Q}{RT}\ loge \quad \text{..... (7)}$$

To determine the unknown terms in the above equation, like stress exponent n, grain size exponent p, activation energy Q, constant A, several creep tests would be required. Iso-stress creep tests of same material at different temperatures are used to derive the activation energy (Q) which is the slope of $log\ \dot{\varepsilon}_{ss}$ vs 1/T plot. Similarly isothermal creep tests of the same material at different stress levels yield the stress exponent (n) which is the slope of $log\ \dot{\varepsilon}_{ss}$ vs $\log(\sigma)$ graph. Iso-stress and isothermal creep tests of samples with similar composition but different grain sizes give the grain size exponent p as slope of $log\ \dot{\varepsilon}_{ss}$ vs $\log(d)$ graph. The rate-controlling creep

mechanism in a polycrystal is usually determined by reference to the experimental values of n, p and Q. The general types of deformation mechanisms during creep as well as specific literature for ZrB_2-SiC UHTC system's creep mechanism are discussed in the next section 1.4.

1.4. Micromechanical Deformation Mechanisms during Creep

The microstructural deformation mechanisms observed in creep can be divided into two types:

- Intra-granular creep deformation
- Inter-granular creep deformation.

If the dominant mechanism is intra-granular, there is no dependence on the presence of grain boundaries so that $p = 0$; whereas if the deformation process involves the grain boundaries, the value of p is in the range from 1 to 3. These two types of process, termed lattice and boundary mechanisms, respectively, are considered in the following subsections.

1.4. 1. Lattice mechanisms

Lattice mechanisms are based on the intragranular motion of dislocations and, by definition, they require $p = 0$. The values of n and Q for the various kinds of lattice mechanisms are listed in the Table 1.1. Q_1, Q_{ci} and Q_p are activation energies for lattice

self-diffusion, chemical inter-diffusion of solute atoms and pipe diffusion along the dislocation cores, respectively. [25]

These theories lead to a stress exponent of n and activation energy for lattice self-diffusion, Q_1, at high temperatures, and a stress exponent of (n + 2) and activation energy for pipe diffusion, Q_p, at low temperatures. A similar transition to (n + 2) and Q_p is also believed to occur in dislocation glide and climb controlled by climb.

1.4. 2. Boundary mechanisms

Boundary mechanisms are based on deformation processes associated with the presence of grain boundaries so that, by definition, $p >\sim 1$. Table 1.2 lists several boundary mechanisms in terms of the predicted values for n, p and Q, where Q_{ph} is the activation energy associated with the presence of a grain boundary liquid phase. [23]

A consequence of all boundary mechanisms is that adjacent grains become displaced with respect to each other, with the displacement occurring at, or close to, the grain boundary plane. It is convenient to make a distinction between those boundary mechanisms in which the displacement, or grain boundary sliding, occurs in association with grain elongation in the tensile direction and those mechanisms in which the displacement is not associated with an elongation of the grains. These two processes are generally termed Lifshitz sliding and Rachlinger sliding, respectively.

(a) Lifshitz sliding: Requires full accommodation by either vacancy flow or intragranular flow extending completely across the grains. For the former accommodation, vacancies diffuse between grain boundaries where the vacancy concentration is either higher or lower than the equilibrium concentration, respectively. As indicated in Table 1.2, this process gives n = 1 but different values of p and Q depending on whether the vacancies diffuse through the lattice (Nabarro- Herring creep) or along the grain boundaries (Coble Creep). In practice, this process may be considered *either* in terms of grain elongation *or* in terms of the sliding displacement. For the latter accommodation, plastic flow takes place between triple points on either side of the grains, giving n = 1, p = 1 and $Q = Q_{gb}$.

(b) Rachinger sliding: Grain boundary sliding without concomitant grain elongation may arise in two distinct ways depending on whether there is a glassy phase at the boundary or the crystalline nature of the lattice is continuous up to the boundary plane. In the absence of a glassy phase, sliding may be accommodated locally by the opening up of grain boundary cavities or by the formation of short folds at the triple points. During deformation with a grain boundary glassy phase, the grain shape accommodation results in cavitations too.

A significant consequence of the presence of cavitations/folds at the grain boundaries is creep asymmetry. Symmetric creep occurs when the creep rate in tension is same as the creep rate in compression. This is important in flexural testing, as in EMMA or conventional 3-pt or 4-pt tests, where the outer side experiences tensile stresses and the inner side experiences compressive stresses. But materials like SiN, siliconized SiC and

SiAlONs have glassy phase boundaries that result in cavitation under tensile stresses which are absent in compressive stresses. The creep rate in tension can therefore be significantly higher than in compression in these materials as discovered by Wiederhorn et al. [26-28] The differential creep laws in tension and compression result in a shift of the neutral axis in the flexure specimen and complicate the stress-strain analysis. This is not a serious problem with the ZrB_2-SiC UHTC material because of the clean (free of amorphous phases) grain boundaries and absence of gross cavitation. Figure 1.7 compares the grain boundaries through high resolution electron images of Si_3N_4 [25] and ZrB_2-SiC. [29] The Si_3N_4 shows the glassy phase (in dark contrast) in the cavities and as thin films at the grain boundaries. ZrB_2-SiC on the other hand shows clean ZrB_2-SiC as well as ZrB_2- ZrB_2 grain boundaries.

Presence of a glassy phase and the reports of intergranular cavitations and triple point cracking suggest the occurrence of some form of Newtonian viscous sliding with stress exponent $n = 1$. Diffusion creep is well understood in simple metallic systems, but there is an additional complication in ceramics because of the presence of two ionic species. Since the cations and anions both participate in the diffusive process, it is necessary to consider ambipolar diffusion and mass transport along parallel diffusion paths. Finally, it should be noted that some possible boundary mechanisms are not included in Table 1.2: for example, the viscous or diffusive growth of intergranular cavities, the role of a solution precipitation process through the intergranular glassy phase and elastic or compliance creep arising from cavity formation and crack growth.

1.5. Previous Creep Studies on UHTCs and Current Research Scenario

Of the very limited literature existing on creep of the ZrB_2 based UHTC systems, the earliest was reported by Spivak et al in 1974. [30] Hot pressed (2200 °C) ZrB_2-ZrN two phase systems with 20-75% ZrN were tested at 2000-2300 °C under 5-20 MPa stress in non oxidizing atmosphere of He. They found the 50% composition to exhibit highest creep rate 8%/hour (~ 2×10^{-5} /s) at 2300 °C. The relative density of all their compositions was very low, varying from 65-75% of theoretical density, and this could have caused sufficient degradation of mechanical properties.

In 1981, Kats et al [31] published their work on flexural creep of another two phase system ZrB_2-ZrC with ZrB_2 content varying from 0-100%. Their bending creep tests were performed on a graphite fixture at 1700-2400 °C under 5-30 MPa stress in He atmosphere. All their mixture compositions were characterized by a creep rate (100%/hour or 2.8×10^{-4} /s at 2400 °C) one or two orders exceeding that of the individual components, and intergranular slip was considered to be the most probable mechanism. The similar creep rates of all the two phase alloys suggests a single creep mechanism in that temperature and stress range with an activation energy of 280 ± 29 kJ/mole. But the authors also reported considerable contamination from WC, with the possibility to form a solid solution of WC in ZrC which was more creep resistant than pure ZrC.

There were no further investigations reported on this topic for another two decades since the high temperature studies on UHTCs showed them to be poor in

oxidation resistance and hence unsuitable for hypersonic vehicle application. Later when addition of SiC has been discovered to improve the oxidation resistance of the UHTC-SiC composite, new research interest spurred. Around this time Martinez et al [32] studied several high temperature mechanical properties, including compressive creep testing of 86.5% dense ZrB_2 and 98% dense ZrB_2 + 4% Ni, in 2002. Their creep tests were performed in argon atmosphere between 1400 -1600 °C under 47- 473.2 MPa stress for pure ZrB_2 and 10-63.5 MPa for the ZrB_2 + 4% Ni. This large difference in the applied stress levels was due to the dramatic strength degradation with the Ni rich phases dominating the fracture behavior. They reported a creep rate of ~ 10^{-6} /s for the porous ZrB_2 at 1600 °C under 408 MPa and the stress exponent of this material was derived to be 1.5. The authors believe the high porosity of the material to significantly affect the properties.

During 2002, a widely accredited and well cited work was published by Levine et al. [4] evaluating the use of UHTCs for aero-propulsion use. Their study included the flexural creep deformation of ZrB_2-SiC UHTCs. Their materials, ZrB_2-20 vol% SiC and ZrB_2-14 vol% SiC-30vol%C, showed significantly smaller creep rates than Spivak and Kats all in the range 10^{-10} – 10^{-8} /s, in air under 180-250 MPa stress, but of course at lower temperatures of 1127 and 1327 °C. These materials also had high retained strength; ZrB_2-20 vol% SiC's flexural strength at 1327 was 356MPa which was over 90% of its room temperature strength of 390 MPa and ZrB_2-14 vol% SiC-30vol%C's flexural strength at 1327 was 183MPa which was over 90% of its room temperature strength of 286 MPa.

In 2008 Talmy et al. published comprehensive research on high temperature creep of the ZrB_2/SiC system [11]. In this work, flexural creep of ZrB_2/0–50 vol% SiC ceramics was characterized in an oxidizing atmosphere as a function of temperature (1200 –1500 °C), stress (30–180 MPa), and SiC particle size (2 and 10 μm). They reported that the creep behavior strongly depended on each of these factors. Their creep rates were faster at higher SiC content but the activation energy was also higher, increasing from about 130 to 511 kJ/mol for 0 and 50 vol% 2-μm SiC. These anomalous results (since creep rate is Arrhenius, higher activation energies should lead to lower creep rates) have not been explained. They also noticed faster creep in systems with decreasing SiC particle size, more significantly at temperatures above 1300 °C. They suggested that the leading creep mechanism in ZrB_2 - 50 vol% SiC was grain boundary sliding based on the stress exponent of ~ 2, which was derived from only three data points. Similarly they suggest diffusional creep for ZrB_2 containing 0 – 25vol% SiC based on a stress exponent of ~ 1 from another three data points. The repeatability of the results was not discussed and hence the error in the measurements can easily affect the slope of the lines and give different values of stress exponent. A bigger data set is therefore essential to make conclusive statements on the value of stress exponent and hence to infer the creep mechanism.

An interesting observation by these researchers was the effect of tensile and compressive stresses (flexural creep specimen) on the oxidation rate. Cracking and grain shifting were observed on the tensile side of the samples containing 25 and 50 vol% SiC,

owing to the stresses pulling the material apart. They observed oxidation of material in the cracks as grain boundaries were opened for oxygen diffusion. The compressive side also showed faster oxidation, though not as high as the tensile side, than the unstressed side. The presence of stress, either compressive or tensile, was found to enhance the oxidation rate. The thickness of the oxidation layers in the zero stress area of the bar was 30 mm, on the compressive side 50 mm, and on the tensile side 80 mm, in a ZrB_2/50 vol% 10-μm SiC ceramic after creep testing at 1300 °C and 100 MPa for 4 hours.

Currently White et al from University of Houston are also investigating ZrB_2-20%SiC, but using 4-pt flexure tests in 1400-1800 °C under 50-100 MPa stress range in oxidation protected Ar atmosphere (unpublished results - courtesy: Prof. Ken White, University of Houston). Their creep rates were on the order of ~ 10^{-9} /s at 1400 °C and increased 4 orders of magnitude to 10^{-5}/s at 1800 °C. Their lower temperature creep rates were much slower (2 orders of magnitude) than any other literature values. They report two temperature dependent activation energies – at low temperatures 1400-1500 °C Q ~ 300 kJ/mol and at higher temperatures Q ~ 700 kJ/mol. Their stress exponent values were also temperature dependent - at low temperatures 1400-1600 °C ~ n =1 and at higher temperatures n ~ 2. The measurement accuracy of strain rates as low as 10^{-9}/s also involves error. The testing temperatures although higher than Talmy are still not as high as those of the application requirement. There is a lack of sufficient number of data points to corroborate their non-uniform results with temperature dependence of Q and n.

Most of these recent investigations have focused on material-property relationships, particularly how SiC composition, other additives, SiC grain size, and property-processing relationships affected the creep rate at elevated temperatures. However, their maximum testing temperatures were less than 1700 °C and nowhere close to ultra high regime, > 2000 °C where the materials are targeted to sustain. The earlier works by Spivak and Kats [26-27], though were in this temperature range of application environment, were not sufficiently comprehensive (with data that did not cover a wide range of temperature, stress spectrum and no repeated results) from a designing perspective. Besides, the authors themselves acknowledged heavy contamination in their materials due to contact with fixtures.

1.6. Other High Temperature Properties

UHTC materials are expected to retain mechanical properties like strength, elastic modulus, hardness and toughness at the intended use temperatures, apart from good creep resistance. The literature in this area has been very limited with barely any investigations focusing primarily on the high temperature mechanical properties of UHTCs. Recently this lack of empirical data at elevated temperatures has been recognized, and numerous studies have been initiated by researchers around the world with several publications in 2010, some of which are summarized in this section. These studies have all found degradation at elevated temperatures, though the extent varied between individual investigations.

There was great variation in the material behavior at elevated temperatures reported in literature. This is due to the different processing conditions and initial material composition and microstructure. Despite the differences, all the reports conclude that mechanical behavior, especially the strength, will degrade to some extent. It should be noted that none of the investigations studied the properties at the expected application temperature, > 2000 °C. Conventional testing has been limited to about 1700 °C due to the reaction with test fixtures which lead to formation of unwanted phases that can affect the material performance. For example, the early creep researchers reported considerable contamination from WC, [31] which could have formed a solid solution of WC in ZrC and this phase was more creep resistant than pure ZrC therefore giving misleading results.

Grigoriev et al. studied the bending strength of ZrB_2 - 18.6 vol% SiC in the temperature range from 20-1400 °C, and reported a significant drop in the strength between 1200 °C and 1400 °C, accompanied by considerable non linearity of stress-strain curve at 1400 °C. They attributed this to the sintering aid $ZrSi_2$ forming amorphous layers at the grain boundary, thus aiding the grain boundary creep. [33] Ramirez-Rico et al reported compressive strength degradation of ZrB_2-20 vol% SiC from 3.1GPa at room temperature to 0.9GPa at 1400 °C, evaluated in air. They also observed that the material exhibited higher strength in slower strain rates than at faster strain rates. [34] Martinez et al have studied high temperature strength, apart from compressive creep mentioned in previous section, with observation of steep drop in flexural strength of ZrB_2 above 800 °C. [32] Levine et al have also explored high temperature flexural strength of their ZrB_2-15%SiC, apart from the creep testing. However these researchers reported quite

significant strength retention; ZrB_2-20 vol% SiC's flexural strength at 1327 °C was 356MPa which was over 90% of its room temperature strength of 390 MPa and ZrB_2-14 vol% SiC - 30vol%C's flexural strength at 1327 °C was 183 MPa which was over 90% of its room temperature strength of 286 MPa. [4] There has been another study at Italy by Alida Bellosi et al. with pressure-less sintered ZrB_2-$MoSi_2$ composites which showed elasticity until fracture and had an increased flexural strength at 1200 °C and high strength retention at 1500 °C. [35-36]

Hu and Wang at Harbin Institute of Technology, China, compared the effect of grain size of starting materials and SiC content on flexural strength and fracture behavior of ZrB_2-15 vol% SiC and ZrB_2-30 vol% SiC composites. Their fine grained specimens (ZrB_2 and SiC of 2μm and 0.5 μm sizes respectively) showed significant reduction in flexural strength at 1800 °C. The strength retention of the 15 and 30 vol% SiC at the elevated temperature was 13% and 7% of their RT strength respectively. [37]

Guicciardi et al published on temperature dependence of dynamic Young's modulus of ZrB_2-$MoSi_2$ by Impulse Excitation Technique up to 1427 °C under non-oxidizing conditions. They found rapid decline in Young's modulus above 1327 °C, associated with grain boundary sliding, but overall retention at 1327 °C was still over 75%. [38]

Hardness testing of ZrB_2 - 18.6 vol% SiC by Grigoriev et al [33] showed the region of brittle fracture of these ceramics to extend up to 1600–2000 °C whereas at higher

temperatures (2000 – 3200 °C), the mechanical behavior was determined by plastic deformation that lead to fracture. However the high temperature results are quite dubious since the ZrB_2 – SiC system has a eutectic melting point at 2210 °C. [39, 40]

To be able to reach the ultra high temperature regime, there has been an interest to develop non – contact mechanical testing techniques. So far only one other such technique is being developed by Hyers et al. at University of Massachusetts. [41] Hyers uses Electrostatic Levitation (ESL), developed by Lee et al. [42] to levitate spherical specimens under high vacuum where laser beam is used to heat and rotate the sample very fast, resulting in sufficient centrifugal load to cause sample to creep. The strains are derived from the deformed shape of the spherical sample captured with high speed digital cameras. Their initial work estimated creep rates of pure ZrB_2 and ZrB_2-25 vol% SiC specimens at 1900 °C under a Von Mises stress of 108 MPa over the entire time period of over 3 hours to be 3.2×10^{-7} 1/s and 2.05×10^{-5} 1/s respectively. Electrostatic levitation requires very high vacuum levels and the equipment is quite expensive. Also this project is yet in the initial stages and the technique has not been validated with the data from conventional methods. EMMA is the other non-contact testing technique which is aimed to be inexpensive and simple to use.

1.7. Ribbon Method

The novel method of resistively heating the electrically conducting UHTCs plays a key role in the development of our mechanical testing procedure. Resistive heating for

oxidation testing was proposed by Karlsdottir et al. at University of Michigan in 2006. [43] It was designed to solve the problems of oxidation testing in conventional laboratory furnaces, where it is hard to reach temperatures above 1600 °C. Thus most studies have been limited to temperatures below 1500 °C [7-9, 44-45]. Resistive heating also allowed for fast heating (~450°C/min) and free cooling rates (~700°C/s), [43] closer to the actual application's environment for these materials.

UHTC materials are metallic conductors [46-47] and can be resistively heated by passing current through the material. A thin cross section, hence called a "Ribbon", can be resistively heated by a modest current – making a self- heated sample. What we term, the ribbon apparatus; as shown in Figure 1.9, is a table top apparatus that by supplying the specimen with appropriate current controls the temperature.

The ribbon samples have a special geometry. A thin cross section is created in the middle of a small match-stick sized bar by reducing the thickness in the center using machining to make a ribbon region supported by the thicker ends on either side. The bar dimensions are in the range, length of 6 mm, breadth of 2mm and thickness of 2 mm. The machined ribbon section has a thickness of 400-500 μm (See Figure 1.10). As the thicker ends have smaller resistance, they remain relatively cool (~100 °C). The thin section has much higher resistance and will heat to 900-2500 °C, depending on the input current. This geometry of a self-heated and self-supported sample also eliminates the problem of contamination by contact with a foreign material in the hot region. Due to the small size

of the sample and small amount of power, the ribbon apparatus reaches high temperatures without creating a difficult–to-manage heat load.

The fact that the material is being heated by passing current gives an opportunity to generate electromagnetic mechanical Lorentz forces if a perpendicular magnetic field is applied, as shown schematically in Figure 1.11. If the current I_x (Amp) is applied in the x-direction along the length of the sample and the magnetic flux density B_y (Tesla) is applied from the side in the y-direction (out of the plane of the paper), there with be a Lorentz force experienced by the ribbon as a distributed mechanical load in the vertical z-direction: $w_z = I_x B_y$ (N/m).

This opportunity is exploited in our novel testing method, called EMMA (Electro Magnetic Mechanical Apparatus). The length of the ribbon thin section has been increased several fold, from 6mm in ribbon method to 37.5 mm in EMMA, since the stress was directly proportional to the square of length. Since UHTCs are metallic conductors, they require only modest amounts of current on the order of 50 amperes to heat these long ribbons to target temperatures. If a perpendicular magnetic field of 1 Tesla is applied, a electromagnetic Lorentz force of 50N/m is generated. This distributed electromagnetic load is used to apply stress on the material and conduct mechanical tests. The stress resulting in a ribbon specimen from this load and the strain calculation from resulting deformation are derived in the next chapter.

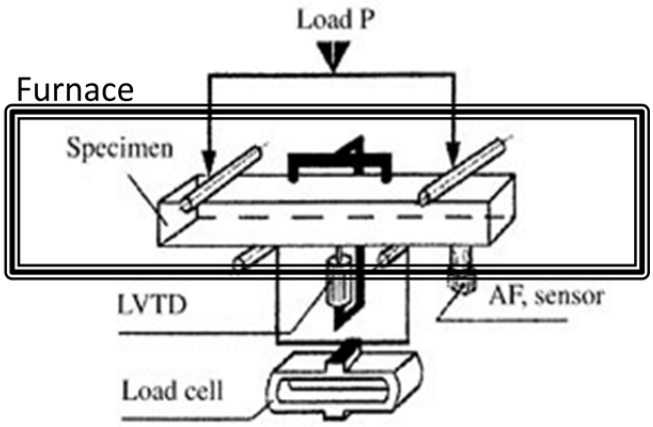

Figure 1.1: Typical flexural creep test set up inside furnace. [22]

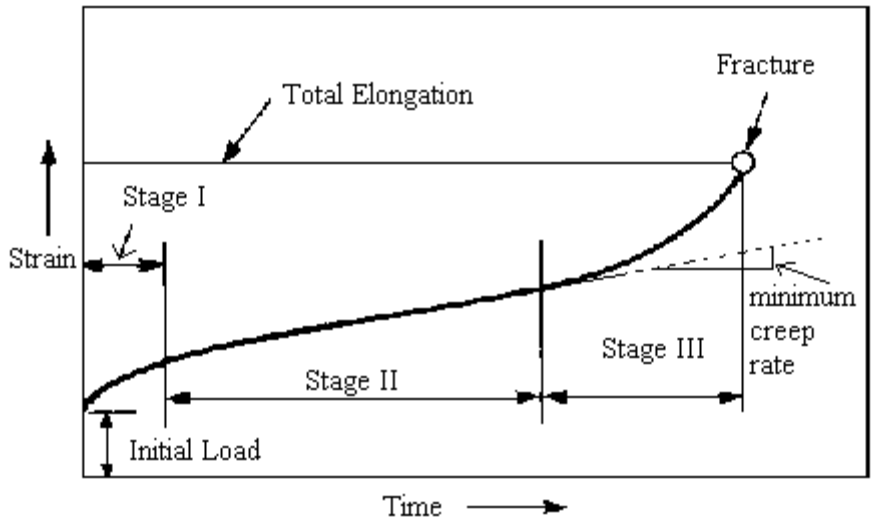

Figure 1.2: General constant stress strain-time curve of a creep test under constant load and temperature

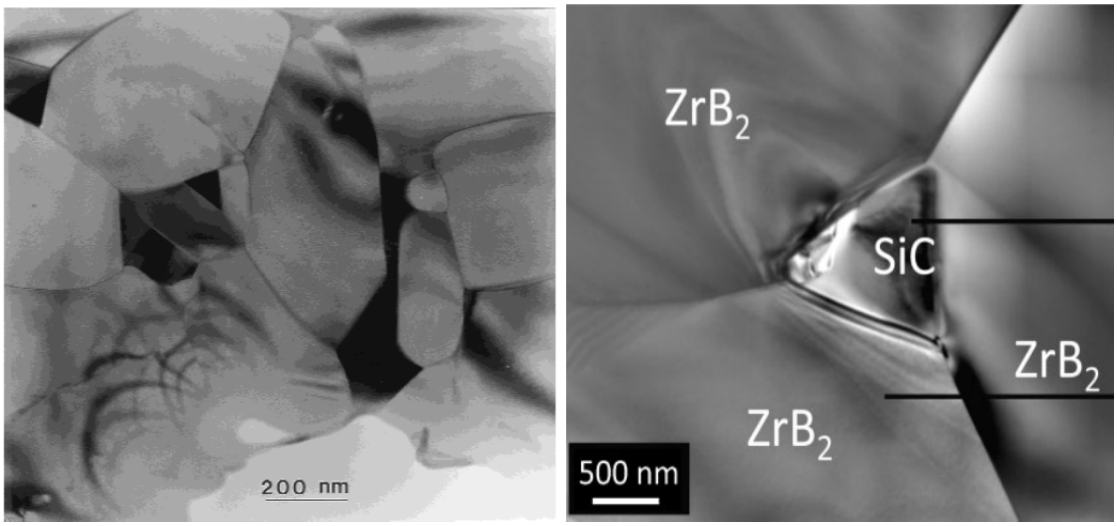

Fig. 1.3: Left: Typical microstructure of a sintered Si_3N_4 showing facet contact percolation of the b-Si_3N_4 grains (light regions). Amorphous phase (dark regions) exists in both large pockets between the grains and as thin films along grain boundaries. [25] Right: Microstructure of sintered ZrB_2-10 vol.%SiC composite showing clean grain boundaries free from glassy phases or cavitations [29]

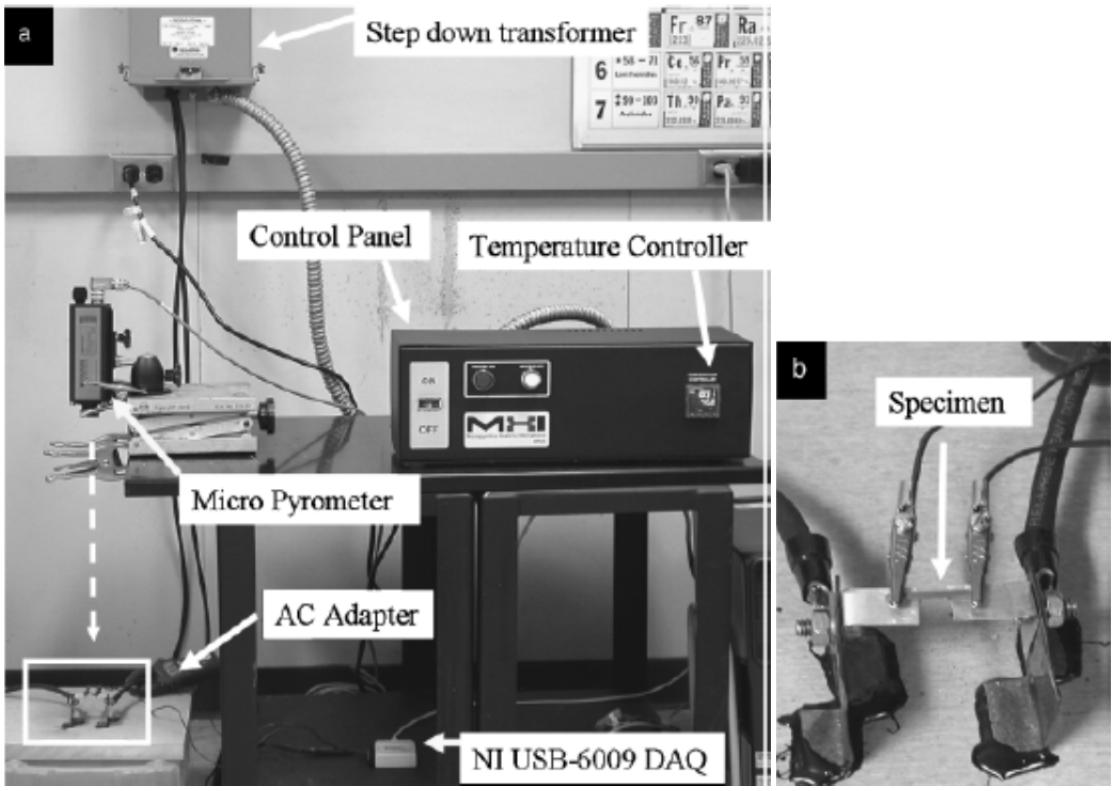

Figure 1.4: (a) Ribbon Apparatus showing all the components with the specimen heating (highlighted) (b) Closer view of the heating component with ribbon specimen sitting on silver plates with two alligator clips holding it together. [43]

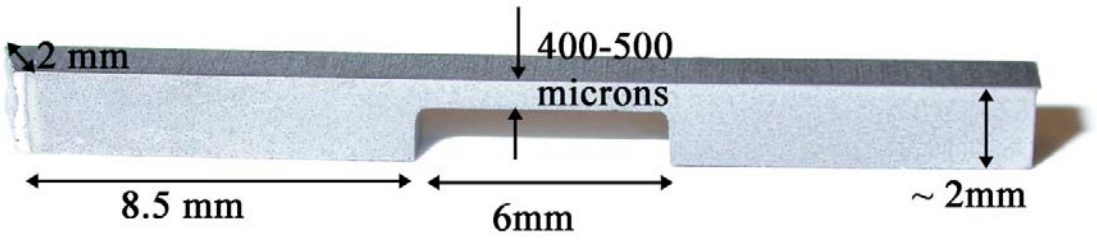

Figure 1.5: Photograph of the miniature ribbon specimen made of ZrB_2-15%SiC [43]

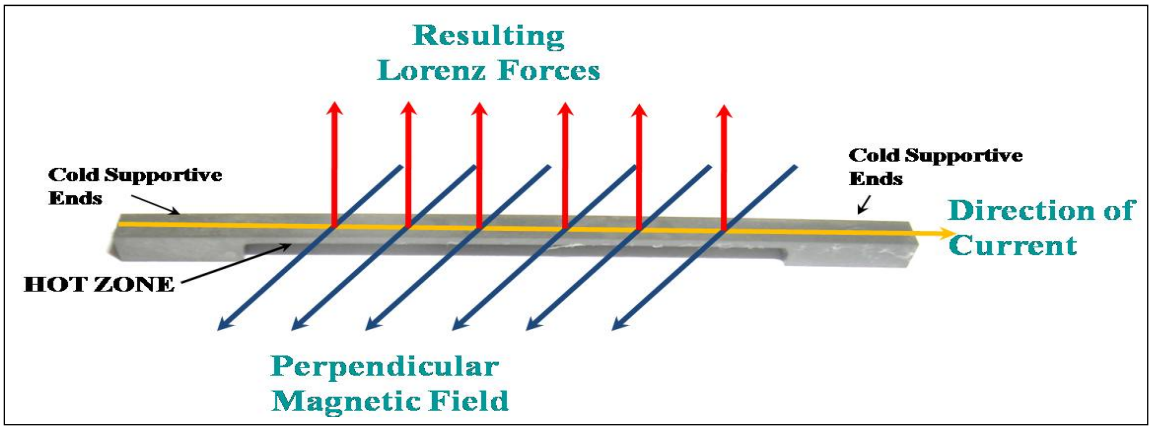

Figure 1.6: Electromagnetic forces (I×B) generated in the current (I) carrying ribbon upon application of a perpendicular magnetic field (B).

Table 1.1: The values of stress exponent "n" and Activation Energy "Q" for various lattice or intra-granular creep mechanisms. Independent of grain boundary, these have a grain size exponent p =0. Q_l, Q_{ci} and Q_p are activation energies for lattice self-diffusion, chemical inter-diffusion of solute atoms and pipe diffusion along the dislocation cores, respectively. [23]

Mechanism	n	Q
Dislocation glide and climb, controlled by climb	4.5	Q_l
Dislocation glide and climb, controlled by glide	3	Q_{ci}
Dissolution of dislocation loops	4	Q_l
Dislocation climb from Bardeen–Herring sources	3 5	Q_l * Q_p
Non-conservative motion of jogged screw dislocations	3†	Q_l
Nabarro–Herring creep at subgrain boundaries	3	Q_l
Climb of dislocations in two-dimensional subgrain boundaries	3	Q_l
Climb of dislocations in subgrain boundaries of finite width	4	Q_l
Recovery creep assuming slip distance is independent of mesh size	4	Q_l
Recovery creep including distribution of dislocation link lengths	3	Q_l
Network coarsening by jog-controlled climb	3	Q_l
Climb of dislocation links within a three-dimensional network:		
(i) Average slip distance equals mesh spacing of network	3 5	Q_l * Q_p
(ii) Slip distance is independent of mesh size	4 6	Q_l * Q_p

Table 1.2: The values of stress exponent "n", grain size exponent "p" and Activation Energy "Q" for various boundary or intergranular creep mechanisms. Q_l, Q_{gb} and Q_{ph} are activation energies for lattice self-diffusion, grain boundary diffusion and grain boundary liquid phase, respectively. [23]

Mechanism	n	p	Q
(i) *Lifshitz sliding*			
Sliding accommodated by diffusion:			
(a) Nabarro–Herring creep	1	2*	Q_l
(b) Coble creep	1	3	Q_{gb}
Sliding accommodated by intragranular flow across the grains	1	1	Q_{gb}
(ii) *Rachinger sliding*			
With a continuous glassy phase at the boundary	1	1	Q_{ph}
Without a glassy phase:			
(a) sliding accommodated by formation of grain boundary cavities	2	1	Q_l
(b) sliding accommodated by formation of triple-point folds	3.5†	2	Q_l

References

1. J. Fuller, "Guest Editorial: Ultra-high temperature ceramics", *Journal of Materials Science Letters*, **39**, 5885, 2004.

2. M.M. Opeka, I.G. Talmy, and J.A. Zaykoski, "Oxidation-Based Materials Selection for 2000 °C + Hypersonic Aerosurface: Theoretical Considerations and Historical Experience", *J. of Mater. Sci.,* 39 [19] 5887-5904 (2004)

3. R. Telle, L.S. Sigl, and K. Takagi, "Transition Metal Boride Ceramics", pp 803-945 in *Handbook of Ceramic Hard Materials*, Vol. 2 Edited by R. Reidel R. Wiley- VCH, Germany, Weinheim (2000).

4. S. R. Levine, E.J. Opila, M.C. Halbig, J.D. Kiser, M. Singh and J. A. Salem. "Evaluation of Ultra High Temperature Ceramics for Aero-Propulsion Use," *J. Eur. Ceram Soc*., 22 2757-2767 (2002)

5. Q. N. Nguyen, E. J. Opila, and R.C. Robinson: Oxidation of Ultrahigh Temperature Ceramics in Water Vapor", *Journal of the Electrochemical Society*, 151 [10] B 558-562 (2004).

6. F. Monteverde, S. Guicciardi, and A. Bellosi "Advances in Microstructure and Mechanical Properties of Zirconium Diboride Based Ceramics," *Materials Science and Engineering*, A 346 310-319 (2003).

7. F. Monteverde, "The Thermal Stability in Air of Hot Pressed Diboride Matrix Composites for Uses at Ultra High Temperatures", *Corrosion Science* 47 2020-2033 (2005).

8. I.G. Talmy, J.A. Zaykoski, M. M. Opeka, S. Dallek, "Oxidation of ZrB2 ceramics modified with SiC and Group IV-VI transition metal diborides" Proceedings of the International Symposium on "High Temperature Corrosion and Materials Chemistry III" edited by M. McNallan and E. Opila, *The Electrochemical Society*, 12, p.144 (2001).

9. I.G. Talmy, J.A. Zaykoski, M. M. Opeka,"Properties of Ceramics in the ZrB2/ZrC/SiC System Prepared by Reactive Processing", *Ceramic Engineering and Science Proceedings,* 19 [3] 105-112 (1998).

10. E. Clougherty, R. Hill, W. Rhodes and E. Peters, "Research and Development of Refractory Oxidation- Resistant Diborides, Part II, Vol. II: Processing and Characterization", Technical Report No. AFML-TR-68-190 (1970).

11. I.G. Talmy, J.A. Zaykoski, C.A. Martin, "Flexural Creep Deformation of ZrB2/SiC Ceramics in Oxidizing Atmosphere", *J. Am. Ceram. Soc*., 91 [5] 1441–1447 (2008).

12. M. M. Opeka, I. G. Talmy, E.J. Wuchina, J. A. Zaykoski and S. J. Causey, "Mechanical, Thermal, and Oxidation Properties of Refractory Hafnium and Zirconium Diboride-Based Composites", *J. Eur. Ceram. Soc*., 22 279-288 (2002).

13. I.G. Talmy, J.A. Zaykoski, M. M. Opeka and S. Dallek, "Oxidation of ZrB2 Ceramics Modified with SiC and Group IV-VI Transition Metal Borides," in High Temperature Corrosion and Materials Chemistry III, edited by M. McNallan and E. Opila (The Electrochemical Society, Inc., Pennington, NJ, 2001) p. 144.

14. A.L. Chamberlain, W.G. Fahrenholtz, G.E. Hilmas, "High Strength Zirconium Diboride-Based Ceramics", *J. Am. Ceram. Soc*., 87 [6] 1170-1172 (2004).

15. A.L. Chamberlain, W.G. Fahrenholtz, G.E. Hilmas, "Pressureless Sintering of Zirconium Diboride", *J. Am. Ceram. Soc*., 89 [2] 450-456 (2006).

16. A. Rezaie, W.G. Fahrenholtz, "Effect of Hot Pressing Time and Temperature on the Microstructure and Mechancial Properties of ZrB2-SiC", *J. Mater. Sci*., 42 2735-2744 (2007).

17. F. Monteverde, "Beneficial Effects of an Ultra-Fine α-SiC Incorporation on the Sinterability and Mechanical Properties of ZrB2", *J. Appl. Phys*., A82 329-337 (2006).

18. A. Rezaie, W.G. Fahrenholtz and G.E. Hilmas "Evolution of Structure during the Oxudation of Zirconium Diboride – Silicon Carbide in Air upto 1500 °C", *J. Eur. Ceram. Soc*., 27 2495-2501 (2007).

19. J.J. Melendez-Martinez, A. Dominguez-Rodriguez, F. Montervede, C. Melandri, G. De Portu, "Characterization and high temperature mechanical properties of zirconium boride-based materials", *J. Eur. Ceram. Soc.* [22] 2543–9 (2002).

20. W.F. Smith, *Foundations of Materials Science and Engineering 3rd ed.*, McGraw-Hill (2004).

21. D.C. Cranmer, *Mechanical testing methodology for ceramic design and reliability*, CRC Press, p. 175 (1998)

22. G.A. Gogotsi, "Mechanical behaviour of yttria- and ferric oxide-doped zirconia at different temperatures", *Ceramic International* 24[8] 589-595 (1998).

23. W.R. Cannon, T.G. Langdon, "Review: Creep of Ceramics – Part1 Mechanical Characteristics" *J. Mater. Sci*., 18 1-50 (1988).

24. J. Li, A. Dasgupta, "Failure-Mechanism Models for Creep and creep Rupture", *IEEE Trans on Reliability* 42[3] 339-353 (1993)

25. D. S. Wilkinson, "Creep Mechanisms in Multiphase Ceramic Materials", *J. Am. Ceram. Soc*., 81 [2] 275-99 (1998).

26. S.M. Wiederhorn, B.J. Hockey and J.D. French "Mechanisms of Deformation of Silicon Nitride and Silicon Carbide at High Temperatures", *J. Eur. Ceram. Soc.* 19 [13-14] 2273–2284 (1999).

27. B. A. Fields, S. M.Wiederhorn, "Creep Cavitation in a Siliconized Silicon Carbide Tested in Tension and Flexure", *J. Am. Ceram. Soc.* 79 [4] 997–86 (1996).

28. T. Chuang, "Improved Analysis for Flexural Creep with Application to Sialon Ceramics", *J. Am. Ceram. Soc.* 73 [8] 2366–73 (1990).

29. D. D. Jayaseelan, Y. Wang, G. E. Hilmas, W. Fahrenholtz, P. Brown and W. E. Lee "TEM investigation of hot pressed -10 vol% SiC-ZrB2 composite", Adv. Appl. Cer., 110 [1] 1-7 (2011).

30. I. I. Spivak, R. A. Andrievsky, V. V. Klimenko, and V. D. Lazarenko, ''Creep in the Binary Systems TiB2–TiC and ZrB2–ZrN,'' *Soviet Powder Metallurgy Metal Ceram*, 13 [8] 617–20 (1974).

31. M. Kats, S. S. Ordan'yan, and V. I. Unrod, ''Compressive Creep of Alloys of the ZrC–ZrB2 and TiC–TiB2 Systems,'' *Soviet Powder Metallurgy Metal Ceram*, 20 [12] 886–90 (1981).

32. J.J. Melendez-Martinez, A. Dominguez-Rodriguez, F. Montervede, C. Melandri, G. De Portu, "Characterization and high temperature mechanical properties of zirconium boride-based materials", *J. Eur. Ceram. Soc.* [22] 2543–9 (2002).

33. O.N. Grigoriev, B.A. Galanov, V.A. Kotenko, S.G. Ivanov, A.V. Koroteev and N.P. Brodnikovsky, "Mechanical Properties of ZrB_2-SiC ($ZrSi_2$) Ceramics", *J. Eur. Ceram. Soc.* [30] 2173-2181 (2010).

34. J. Ramirez-Rico, M.A. Bautista, J. Martinez-Fernandez and M.Singh, "Compressive Strength Degradation in ZrB_2-Based Ultra High Temperature Ceramic Composites", *J. Eur. Ceram. Soc.* (2010) in press.**

35. D. Sciti, S.Guicciardi and A. Bellosi, "Properties of a Pressureless – Sintered ZrB2-MoSi2 Ceramic Composite", *J. Am. Ceram. Soc.* 89 [7] 2320-2322 (2006).

36. A. Bellosi, F. Montervede and D. Sciti, "Fast Densification of Ultra High Temperature Ceramics by Spark Plasma Sintering", *Int. J. Appl. Ceram. Technol.* 3 [1] 32-40 (2006).

37. P. Hu, Z. Wang, "Flexural strength and fracture behavior of ZrB2–SiC ultra-high temperature ceramic composites at 1800 °C", *J. Eur. Ceram. Soc.* [30] 1021-1026 (2010).

38. S. Guicciardi, A.K. Swarnakar, O. V. Biest and D. Sciti, "Temperature Dependence of the Dynamic Young's Modulus of ZrB2-MoSi2 Ultra-Refractory Ceramic Composites", *Scripta Materialia* (62) 831-834 (2010).

39. L. Kauffman, "Calculation of Multicomponent Refractory Composite Phase Diagrams", Manlabs, Cambridge MA Final rept. Naval Surface Weapons Center, NSWC TR-86-242, ADA192293, 1 June 1986.

40. R. Tu, H. Hirayama and T. Goto "Passive oxidation behavior of ZrB2-SiC eutectic composite prepared by arc melting", *Key Eng. Mat.,* 403 217-220 (2009).

41. X. Ye, R.W. Hyers, "Computational methods for the analysis of, non-contact creep deformation, in ZrB2–SiC composites", *J. Eur. Ceram. Soc.* [30] 2191-2196 (2010).

42. J. Lee, R.C. Bradshaw, R.W. Hyers, J.R. Rogers, T.J. Rathz, J.J. Wall, H. Choo, P.K. Liaw, "Non-Contact Measurement of Creep Resistance of Ultra-High Temperature Materials", *Mater Sci. Eng A: Struct. Mater.: Prop, Microstruct. Process*; 463(1–2):185–96 (2007).

43. S. Karlsdottir, J.W. Halloran, "Rapid Oxidation Characterization of Ultra High Temperature Ceramics" *J. Am. Ceram. Soc*., 90 [10] 3233–3238 (2007)

44. W.C. Tripp and H.C. Graham, "Thermogravimetric Study of Oxidation of ZrB2 in Temperature Range of 800 Degrees to 1500 Degrees", *Journal of the Electrochemical Society*, 118, 1195-1971 (1971).

45. M. M. Opeka, I. G. Talmy, E.J. Wuchina, J. A. Zaykoski and S. J. Causey, "Mechanical, Thermal, and Oxidation Properties of Refractory Hafnium and Zirconium Diboride-Based Composites", *J. Eur. Ceram. Soc*., 22 279-288 (2002).

46. NASA Ames Research Center. TPSX Material Properties Database, "Zirconium Diboride, ZrB2-SiC" http://tpsx.arc.nasa.gov/

47. W.C. Tripp, H.H. Davis, and H.C. Graham, "Effect of SiC addition on Oxidation of ZrB2", *Am. Ceram. Soc. Bull*., 52 [8] 612-616 (1973).

CHAPTER 2

ELECTROMAGNETIC MECHANICAL APPARATUS – THE TECHNIQUE

2.1. Electromagnetism

Electromagnetism is one of the fundamental forces of nature arising from the interaction of electrically charged particles. The Lorentz force is the force on a point charge due to electromagnetic fields, given in terms of the electric and magnetic fields by the following equation:

$$F = q[E + (v \times B)]$$

where F is the force (N), E is the electric field (V/m), B is the magnetic field (T), q is the electric charge of the particle (C) and v is the instantaneous velocity of the particle (m/s). In the absence of electric field,

$$F = q(v \times B)$$

This could be rewritten for a current carrying conductor in purely magnetic field as **F**= **I** x **B**. Since $q.v$ = I, a moving charge is equivalent to current. When the ribbon

specimen is resistively heated, all that is required to create a mechanical load is the application of a magnetic flux density **B**, to create a Lorentz force per unit length

$$\mathbf{F} = \mathbf{I} \times \mathbf{B}. \quad \text{----- (1)}$$

If the current is applied in the x-direction along the length of a sample L_T, and the magnetic flux density is applied from the sides in the y-direction, there will be a distributed mechanical load (w in N/m) directed vertically in the z-direction: $w_z = I_x B_y$. For example, if the current required to heat the ribbon is 50 amps and the applied magnetic flux density is 10,000 G (or 1 T or 1 N/m-A), there will be a uniform loading w=50 N/m. The total force on a 30 mm long specimen (L_T = 0.030m) will be 1.5N, or about 0.34 pounds of force. This is not a large force, so it will be easy to keep specimen attached to a support structure.

2.2 Relation of Current to Temperature

Consider the geometry of the UHTC Ribbon Specimen, as illustrated in Figure 2.1. This is a small bar UHTC specimen, such as a standard ASTM "B-bar" used for flexural testing [1], with thickness t_T, width Y and total length L_T. The center section is machined away using a surface grinder to leave a ribbon of length L and thickness t. The ribbon is the hot section. It is supported by the thicker ends (the cold support). When an electrical current I passes down the length of the specimen, the current density is low in the cold support (current density =I/Yt_T) and it remains cool. But the current density is much higher in the thin ribbon (current density = I/Yt), and it is heated to incandescence. Thus we can have a very hot ribbon (1400-2200 °C) self-supported by its cold ends.

The temperature T of the ribbon varies across the ribbon section, depending on the current *I*, electrical resistivity ρ, and heat transfer conditions by conduction, convection, and radiation. For significantly long ribbons the temperature will be approximately uniform if most of the heat transfer is radiation or convection, except for the regions near the thick ends where there will be longitudinal gradients from conductive loss. At high temperatures where radiation dominates, the temperature variations can be estimated by equating the power input by Joule heating to the power lost by radiation:

In radiation, energy radiated per second: $= \varepsilon\sigma AT^4$ [2]

where ε = emissivity (0-1)

σ= Stefan-Boltzmann constant = 5.67 x 10^{-8} J/(s-m^2-K^4)

A = surface area of object = L.Y

T = Kelvin temperature

And power input = $I^2R = I^2.\rho.L/A$ where A = Cross-sectional area. = Y.t

At steady state, all the power should be radiated away,

$$T \approx \frac{\rho^{1/4}\beta}{(\varepsilon)^{1/4}} I^{1/2} \qquad \text{------- (2)}$$

where $\beta = \frac{1}{(Y^2 t)^{1/4}}$ is a term involving geometric factors width and thickness. Notice that the temperature depends on the square root of the current and fourth root of the resistivity.

The uniformity of the temperature across the length of the ribbon is also an important criterion. Due to the geometry of the ribbons, the two thick ends act as heat sinks and there will be a temperature gradient from their edge towards the center of the ribbon. In short ribbons such as the ones used earlier for oxidative studies, the total length of the thin section is 6mm. Only 2mm of the center is at uniform temperature (error of ± 20 °C) and the rest has temperature gradients. To have a longer portion of uniform temperature, the thin section has to be much longer. This ensures that there will be a lot of material away from the two heat sinks and therefore at temperatures within a few degrees from the target. Therefore EMMA requires a relatively long region of the ribbon to be at a uniform temperature. The temperature distribution was calculated numerically in a 37.5mm long thin section with 6.25mm thick ends. The width and thickness of this specimen were taken to be 2.5mm and 0.35 mm respectively. A one dimensional finite element model is used with the dimension along the thin section's length. Figure 2.2 shows an element with vertical heat loss by radiation and axial heat loss by conduction.

The current along the length of the ribbon is taken to be 60 amperes and the resistivity of the material was known to be ~ 2.66×10^{-7} Ω-m. The heat thus resistively generated in any section of the thin ribbon (such as highlighted in Figure 2.2) is considered to dissipate through radiation from the upper and lower surfaces. Additionally heat conduction from the neighboring elements due to temperature gradients is also considered. This temperature profile solved using 1-D Finite Element Model is presented in Figure 2.3 (B).

The model is verified by measurements taken along the length of the ribbon at 0.25mm intervals. However, the infrared pyrometer which was used for these measurements can read only above 900 °C, therefore there is a discontinuity in the region with the temperature gradients near the thick ends. The temperature of the thick ends was measured using a thermocouple and was rather uniform at ~ 100 °C (± 5 °C). The model fits quite well with the measured values and proves that this sample geometry has a 25mm long region in the center of the ribbon where the temperature is rather uniform and has temperature gradients near the thick ends over a length of 6mm on each side.

2.3 Relation of Current and Flux Density to Stress

If the entire specimen is exposed to a transverse magnetic flux density B_y, it will experience a uniform distributed mechanical load w_z, as described above. But the section modulus of the specimen changes dramatically in the thin ribbon section, so that if the cold support ends are held in place, the thin ribbon behaves like a beam of length L. The mechanical behavior of the thin section as a beam is highly dependent on the nature of fixation of the ends. The moment generated by the mechanical load is the cause for stress experienced in the ribbon. This moment can be altered by the reaction moments that certain types of end fixations can generate and hence affect overall stress experienced in the ribbon. There were three types of behavior possible with the end supports acting as – Fixed-Fixed ends, Pinned-Pinned ends, and Fixed-Pinned ends.

2.3.1. Fixed Ends

If the thick edges of the ribbon are held in place without allowing any lateral movement, the mechanics are similar to a beam with fixed ends. The mechanics of such a beam is illustrated in Figure 2.4 of the uniformly loaded beam with fixed supports.

A fixed end – fixed end beam under distributed load is a commonly studied structural analysis problem [3,4,5]. M_R, R_x and R_y are unknown reaction moments and forces generated at the fixed ends, which can be obtained by balance of all the forces and moments in the above free body diagram. The distributed load causes bending moments in the ribbon given by:

$$M(x) = \frac{w_z}{2}x(L-x) - \frac{w_z L^2}{12}$$

where *x* is the distance from one of the fixed ends. This moment is largest at the center of the span, M (L/2):

$$M\left(\frac{L}{2}\right) = w_z \frac{L^2}{24}$$

This moment generates stress in the ribbon which varies linearly with moment and the distance from neutral axis, c [5]:

$$\sigma(x) = \frac{M(x) \times c}{I}$$

Therefore the maximum stress is experienced by the outermost fibers (thus farthest from neutral axis, c = t/2) in the center. The Moment of Inertia, *I*, for a rectangular cross section such as our ribbon is also known.

$$\sigma_{\max} = \frac{Mc}{I} = \frac{M\left(\frac{L}{2}\right)\times t}{2I} = \frac{\frac{w_z L^2}{24}t}{2\frac{Yt^3}{12}} = \frac{w_z L^2}{24}\frac{6}{Yt^2}$$

and since the distributed force $w_z = I_x B_y$, the maximum flexural stress on the ribbon is related to the current, magnetic flux, and ribbon dimensions:

$$\sigma_{\max} = 0.25\frac{L^2}{Yt^2}\left(I_x B_y\right) \qquad \text{--------- (3)}$$

2.3.2. Pinned Ends

On the other hand if the thick edges of the ribbon are allowed any lateral movement, the ribbon behaves very differently and the mechanics are similar to a beam with pinned ends. The mechanics of such a beam are illustrated in Figure 2.5 under uniform loaded beam with roller supports.

A pinned beam under distributed load is also a commonly studied structural analysis problem [3,4]. These ends do not support any reaction moments and horizontal reaction forces. Therefore only reaction forces are vertical, R_y, which can be obtained by the balance of vertical forces. The distributed load causes bending moments in the ribbon given by:

$$M(x) = \frac{w_z}{2}x(L-x)$$

where *x* is the distance from one of the ends. This moment is largest at the center of the span, M (L/2):

$$M\left(\frac{L}{2}\right) = w_z \frac{L^2}{8}$$

The stress generated by this moment in the ribbon is [5]: $\sigma(x) = \frac{M(x) \times c}{I}$. Therefore the maximum stress experienced by the outermost fibers will be:

$$\sigma_{\max} = \frac{Mc}{I} = \frac{M\left(\frac{L}{2}\right) \times t}{2I} = \frac{\frac{w_z L^2}{8} t}{2\frac{Yt^3}{12}} = \frac{w_z L^2}{8} \frac{6}{Yt^2}$$

In terms of current and magnetic flux, the maximum flexural stress:

$$\sigma_{\max} = 0.75 \frac{L^2}{Yt^2} \left(I_x B_y\right) \qquad \text{--------- (4)}$$

Therefore if the supports are allowed lateral movement stresses would be three times higher than when restricted.

2.3.3. Fixed End + Pinned End

If one of the thick edges of the ribbon is restricted from any lateral movement and the other edge is allowed to move horizontally, then the ribbon behaves as a fixed-pinned ended beam. The mechanics of such a beam under uniform load are illustrated in Figure 2.6. Although the mechanics of this situation are not as commonly studied, structural analysis of this problem has been explored in a few books [6,7]. The distributed load causes bending moments in the ribbon given by:

$$M(x) = w_z x \left(\frac{3L}{8} - \frac{x}{2}\right)$$

where x is the distance from the pinned end. The moment is not largest at the center as was in the previous cases, but instead is largest at $x = \frac{3L}{8}$:

$$M\left(\frac{3L}{8}\right) = w_z \frac{9L^2}{128}$$

The location of this largest moment also experiences the largest stress:

$$\sigma_{\max} = \frac{Mc}{I} = \frac{M\left(\frac{3L}{8}\right) \times t}{2I} = \frac{\frac{9w_z L^2}{128} t}{2\frac{Yt^3}{12}} = \frac{w_z L^2}{64} \frac{27}{Yt^2}$$

and since the distributed force $w_z = I_x B_y$, the maximum flexural stress on the ribbon is,

$$\sigma_{\max} = \frac{27}{64} \frac{L^2}{Yt^2} \left(I_x B_y\right) \text{ --------- (5)}$$

smaller than that of a pinned-pinned beam but larger than that in a fixed-fixed beam.

2.4. Strain and Deformation in EMMA

The previous section derived the stress conditions in the ribbon section from the bending moments caused by the distributed mechanical load, w_z. This section covers the solution for elastic deformation in these ribbons which can also be obtained from the bending moments. The curvature at any location is directly related to the bending moment, M, at that location as:

$$\frac{d^2y}{d^2x} = \frac{M(x)}{EI} \qquad --------(6)$$

Therefore the deflection locus is given by integration,

$$y(x) = \int_0^x \int_0^x \frac{M(x)}{EI} \qquad ------(7)$$

The moment profile M(x) was calculated for all the support systems in the previous chapter. The deflection profile can be derived using the different boundary conditions for each case. The location of the maximum deflection occurs where $\frac{dy}{dx} = 0$ and so can be derived easily as well. In conventional flexural creep testing, like 3-point bending or 4-point bending, the strains are derived from the maximum deformation which can be empirically measured. A similar attempt is done here and the strains are derived from the maximum deflection by replacing the Elastic Modulus (E) with $\frac{\sigma(max)}{\varepsilon}$. This equation will relate the strain caused by the flexural bending with distributed load to the maximum deflection.

2.4.1. Fixed Ends

For a fixed-fixed ended beam the moment profile, $M(x) = \frac{w_z}{2}x(L-x) - \frac{w_z L^2}{12}$. The boundary conditions for these supports are that the the deflection and the slope are zero at the edges. Then integrating *M(x)* twice gives the deflection profile to be:

$$y(x) = \frac{w_z x^2}{24EI}(L-x)^2$$

The maximum deflection occurs where $\frac{dy}{dx} = 0$, i.e. at the center,

$$y_{max} = y\left(\frac{L}{2}\right) = \frac{w_z L^4}{384.EI}$$

Replacing the Elastic Modulus (E) with $\frac{\sigma(L/2)}{\varepsilon}$, i.e., $\frac{0.25\frac{L^2}{Yt^2}w_z}{\varepsilon}$:

$$y_{max} = \frac{w_z L^4}{384.\frac{0.25\frac{L^2}{Yt^2}w_z}{\varepsilon}.\frac{Yt^3}{12}} = \frac{\varepsilon L^2}{8t}$$

Therefore the strain in fixed-fixed ended beam is related the maximum deflection as:

$$\varepsilon = 8\frac{y_{max}t}{L^2} \qquad ---------(8)$$

2.4.2. Pinned Ends

The moment profile of this beam was $M(x) = \frac{w_z}{2}x(L-x)$. The boundary conditions for these supports are that the deflection would be zero at the edges and the center. Then integrating the *M(x)* twice gives the deflection profile to be:

$$y(x) = \frac{w_z x}{24EI}(L^3 - 2Lx^2 + x^3)$$

The maximum deflection occurs where $\frac{dy}{dx} = 0$, i.e. at the center,

$$y_{max} = y\left(\frac{L}{2}\right) = \frac{5w_z L^4}{384.EI}$$

Replacing the Elastic Modulus (E) with $\frac{\sigma(L/2)}{\varepsilon}$, i.e., $\frac{0.75\frac{L^2}{Yt^2}w_z}{\varepsilon}$:

$$y_{max} = \frac{5\,w_z L^4}{384.\frac{0.75\frac{L^2}{Yt^2}w_z}{\varepsilon}.\frac{Yt^3}{12}} = \frac{5\varepsilon L^2}{24t}$$

Therefore the strain in pinned beam is related the maximum deflection as:

$$\varepsilon = 4.8\frac{y_{max}t}{L^2} \qquad ---------(9)$$

2.4.3. Pinned-Fixed Ends

The moment profile of this beam was $M(x) = w_z\, x\left(\frac{3L}{8} - \frac{x}{2}\right)$. The corresponding deflection profile is:

$$y(x) = \frac{w_z x}{48EI}(L^3 - 3Lx^2 + 2x^3)$$

The maximum deflection occurs where $\frac{dy}{dx} = 0$, at $x = \frac{L}{16}\left(1 + \sqrt{33}\right)$

$$y_{max} = y\left(\frac{L}{2}\right) = \frac{w_z L^4}{185.EI}$$

Replacing the Elastic Modulus (E) with $\frac{\sigma(max)}{\varepsilon}$, i.e., $\frac{\frac{27\,L^2}{64\,Yt^2}w_z}{\varepsilon}$:

$$y_{max} = \frac{w_z L^4}{185.\frac{27}{64}\frac{L^2}{Yt^2}\frac{w_z}{\varepsilon}.\frac{Yt^3}{12}} = \frac{256}{1665}\frac{\varepsilon L^2}{t}$$

Therefore the strain in pinned-fixed ended beam is related the maximum deflection as:

$$\varepsilon = 6.5\frac{y_{max}t}{L^2} \qquad ---------(10)$$

From comparison of the strain with respect to maximum deflection in the three support systems, it can be noticed that the $\frac{\varepsilon}{y_{max}}$ is largest for the fixed-fixed beam, followed by pinned-fixed beam, and smallest for pinned-pinned beam. The significance is that although large deflections can occur in pinned beams, the strain is not as high. On the other hand, in the fixed beams the apparent deformation may not be large, but the corresponding strain could be.

Figure 2.7 is the predicted deformation profile of a ribbon under same amount of distributed load, but with different support systems. This trend can be explained by the fact that the fixed ends generate reaction moments that counter the bending moment caused by the load. The pinned ends cannot support reaction moments, and therefore even a similar load causes larger stresses causing it to deform more. They also do not resist deformation at the edges leading to large y_{max} values. The fixed supports cannot deform at the edges placing further resistance to deformation, leading to smaller y_{max} values. Fixed-free behavior falls midway between the two. Figure 2.8 summarizes the stress and the strain conditions in ribbons under distributed load with each of the above support types. The supports used in EMMA were spring loaded contacts (miniature alligator clips) which acted in all the three different ways discussed above at different times due to the manufacturing variation in the spring constant and hence the applied by these contacts.

The creep rates, $\dot{\varepsilon}$, in EMMA can be derived from the rate of change of the maximum deflection. In conventional testing, the rate of change of the maximum deflection is same as the load head speed. The load head which applies weight load on the sample has an extensometer to measure the deflection. In EMMA where there is no load head, the deflection is measured empirically in a non-contact manner using a laser micrometer (discussed in detail in Chapter 3 later).

2.5. Relation of Stress and Temperature

The current I_x cannot be changed without changing the temperature. In order to vary the stress at constant temperature, either the magnetic flux or specimen dimensions must change. We can approximately model this from Equation 2 by using $\Theta \approx \frac{\rho(\Theta)^{1/4}\beta}{(\varepsilon)^{1/4}} I^{1/2}$ to express the current as an implicit function of temperature, given by equation 11:

$$I \approx \sqrt{\frac{\varepsilon}{\rho\beta}}\Theta^2 \qquad \text{---------- (11)}$$

Which can be substituted into the expression for stress to give:

$$\sigma_{max} \approx x\sqrt{\frac{\varepsilon}{\rho\beta}}\Theta^2\left[\frac{L^2}{Yt^2}\right]B_z \qquad \text{---------- (12)}$$

Thus at any magnetic field, B, the stress (σ) and the temperature (Θ) are related and are dependent on the resistance (ρ), emissivity (ε) and specimen dimensions.

For a typical case where I= 50 amps, and B= 1 Tesla (or 1 N/Am or 10000 Gauss), with a ribbon with L= 25 mm, Y=2 mm and t=0.2 mm, the maximum stress is about 150 MPa. This is sufficient to cause significant creep deflection at 1500^{o}C or above for most ZrB_2-SiC composites, based on Inna Talmy's data [6]. A specimen twice as long (L=50 mm), should experience 600 MPa, probably enough for fracture. Therefore applying a 1.5N force, it is possible to generate substantial stresses, which gives EMMA unique advantage.

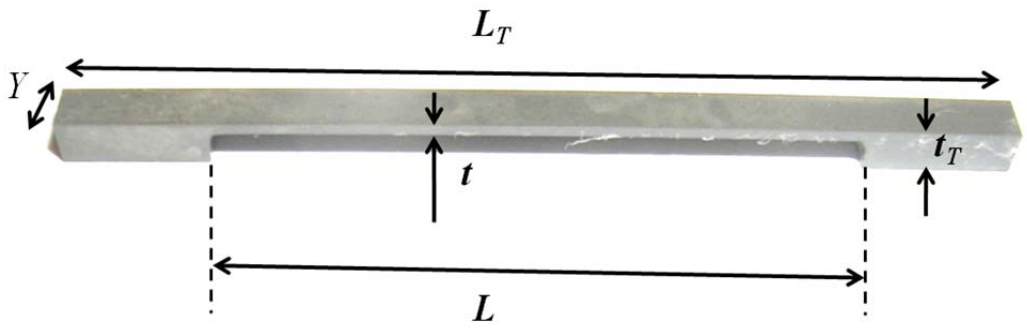

Figure 2.1: Ribbon specimen illustration with notations for dimensions marked.

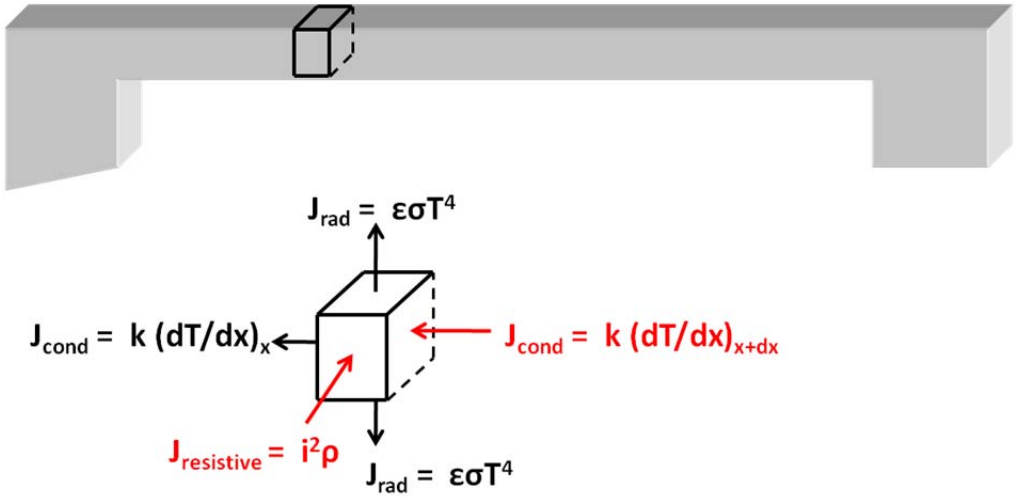

Figure 2.2: Heat flow diagram of a single element in the 1-D finite element model for temperature profile across the ribbon specimen. Resistively generated heat is dissipating through radiation from upper and lower surfaces. Additionally the heat conduction from temperature gradients with neighboring elements is also considered.

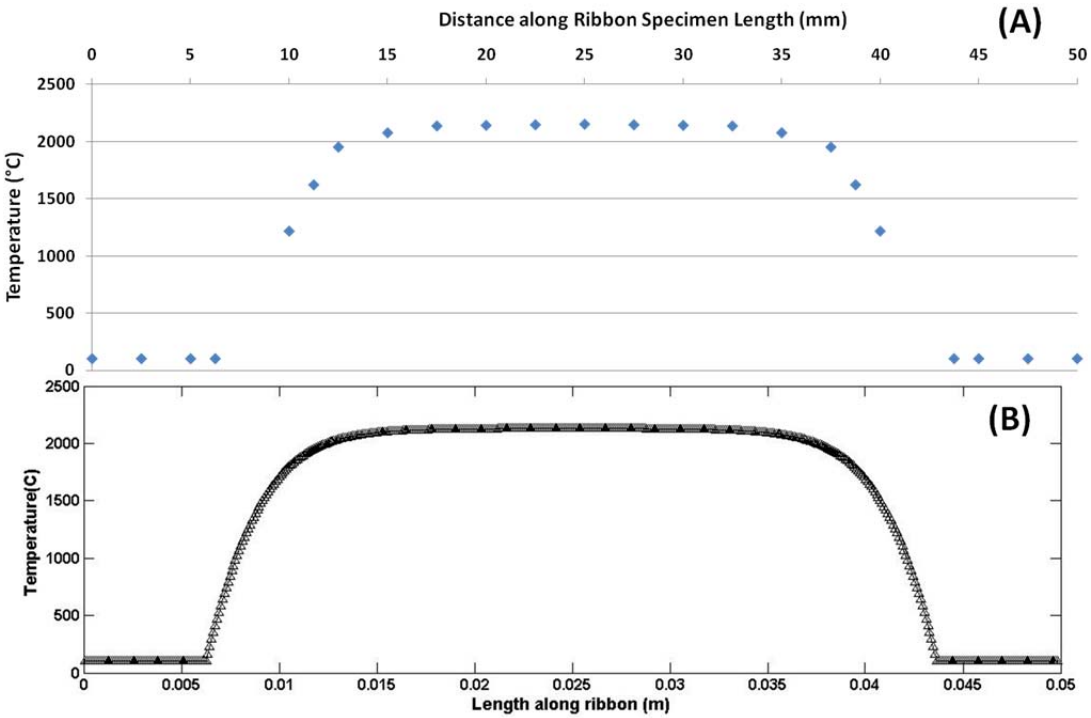

Figure 2.3: Temperature profile across a ribbon specimen with 37.5mm long thin section and 6.25mm long thick ends. (A) Measured temperature profile using an infrared pyrometer (B) Calculated using a 1-D Finite Element Model considering heat dissipation through radiation and conduction across temperature gradients.

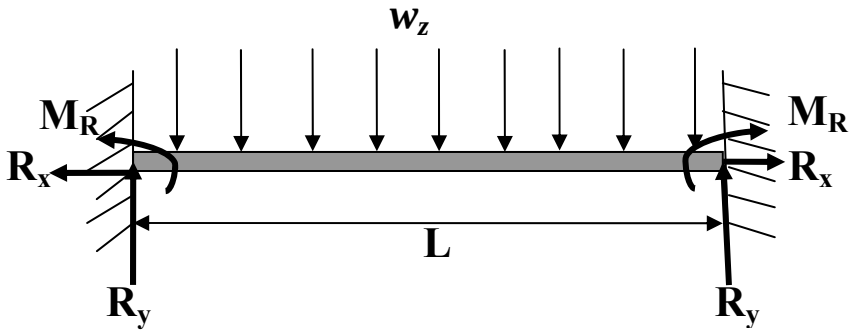

Figure 2.4: Free body diagram of the fixed ended beam, uniform load w_z will be I×B (cross product).

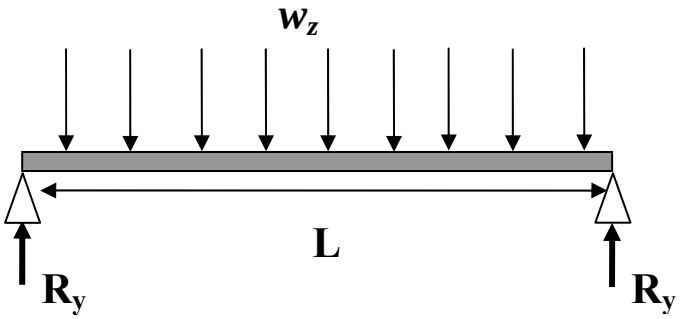

Figure 2.5: Free body diagram of the pinned beam, uniform load w_z will be I×B.

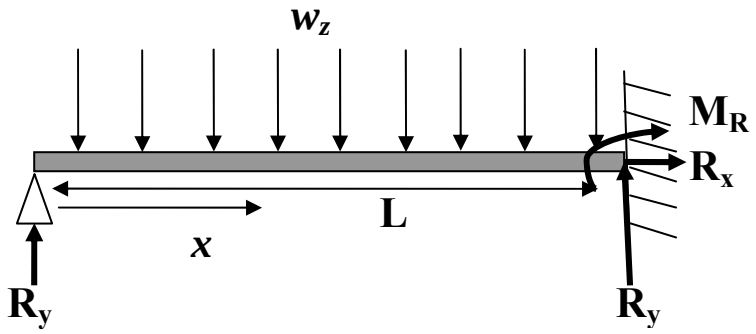

Figure 2.6: Free body diagram of pinned-fixed ended beam, uniform load w_z will be I×B.

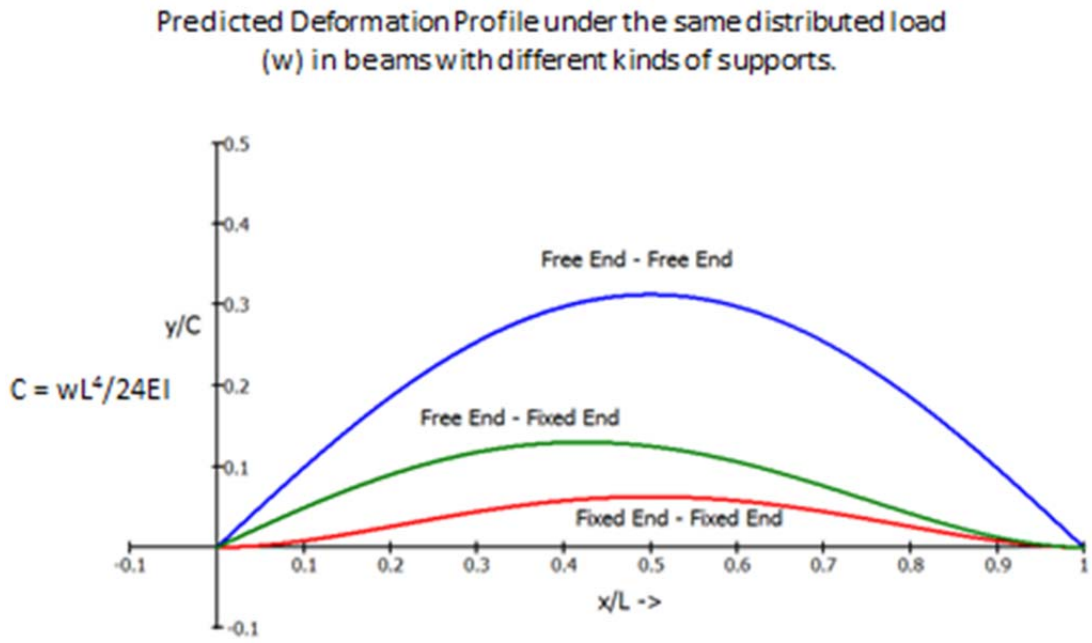

Figure 2.7: Predicted shape of the ribbon after elastic deformation under an equal distributed load with different end supports.

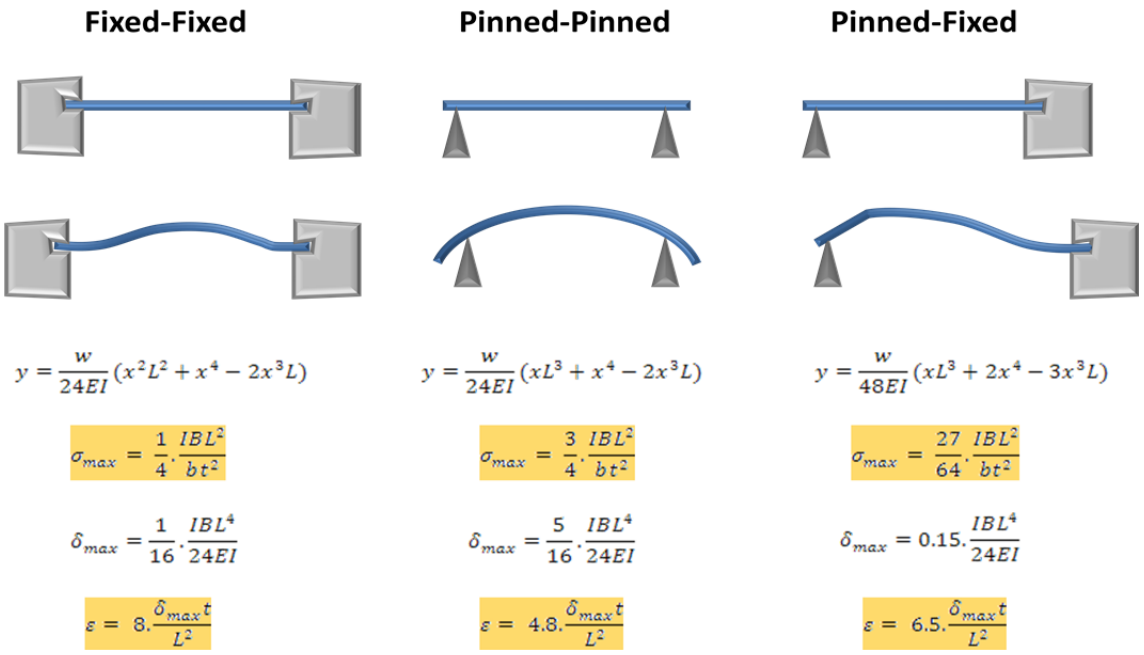

Figure 2.8: Summary of the stress and the strain conditions in the ribbons under distributed load (w= IB) with different support systems.

References

1. http://www.astm.org/Standards/A370.htm

2. Robert Siegel and John Howell, "Thermal Radiation Heat Transfer", 4th edition, © *Taylor and Francis, London* (2002).

3. Harry West, "Analysis of Structures: An integration of classical and modern methods", second edition, John Wiley and Sons, Inc. (1989).

4. D. Lenczner, "Deflections of Beams and Composite Subject to Creep", *Build. Sci.* Vol. 6, pp-45-51.

5. R. C. Coates, M. G. Coutie, F. K. Kong "Structural Analysis", 3rd Edition, © *Chapman and Hall, London*, UK (1997).

6. W.C. Young, Roark's Formulas for Stress and Strain , 6th edition, © McGraw-Hill (1989).

7. W.D. Pilkey, Formulas for Stress, Strain, and Structural Matrices, 2nd edition, © John Wiley & Sons, New York (2005).

CHAPTER 3

ELECTROMAGNETIC MECHANICAL APPARATUS – THE EQUIPMENT

3.1. Prototype Apparatus

For Phase-I of this project,* a prototype apparatus was built whose main purpose was to demonstrate the feasibility of the idea. Due to a lack of resources, notably time and initial funding, this apparatus, named EMMA1, was mainly a modification of the Ribbon Method discussed in the Chapter 1, section 1.7. It was made of rather crude components which could be quickly obtained. We emphasized small and low cost components, since we envisioned a compact table-top device for the later phases as well. The EMMA1 apparatus was limited to the two essential elements: 1) controllable electrical current, with fast feedback so that temperature could be controlled; 2) a means to expose the sample to a magnetic flux density on the order of ~ 0.2-0.5 Tesla, which we call magnetic flux assembly.

---

* The early stages of EMMA1 was included in the thesis written for Master of Science and Engineering degree: S. Gangireddy "*In situ* Optical Microscopy of Ultra High Temperature Oxidation of Zirconium Diboride and Silicon Carbide Ceramic Composites" – 10 April 2009

The Ribbon Method set up was modified (Figure 3.1) to accommodate longer ribbons, since the stresses were found to be proportional to the square of ribbon length, as given by equations 3,4,5 in the previous chapter. The thick ends of the sample were held onto the silver contact plates using alligator clips. The plates were in turn connected to cables of controllable power supply using brass bolts, completing the electric circuit. In EMMA1, the ribbon was in the gap between two permanent magnets. Figure 3.2 is a photograph of the EMMA1 magnetic flux assembly, showing the two Nd-B-Fe permanent magnets, attached to rigid steel plates using a brass fixture. These were Grade N52 block magnets with surface field of 6325 Gauss and $B_{r\,max}$ of 14,800 Gauss.

The brass fixture was a magnetically transparent means to hold the block magnets to the plate against the rather strong attractive force, 400N, and a high thermal conductivity sink for heat radiated from the hot specimen to prevent the Nd-Fe-B from getting hot. The steel plates were attached to the jaws of a small machinist's vise which served two functions:

a. The iron body of the vice completed the magnetic circuit.
b. The adjustable gap between its jaws allowed varying the magnetic flux density.

The magnets were opposed north face against south face so they strongly attracted each other and created a magnetic flux density in the air gap.

Magnetic flux density in the air gap at a distance along the axis between a pair of rectangular magnets with steel path could be simply calculated from superimposition of the magnetic fields from either magnet

$$B = B_1 + B_2 \qquad \text{---------- (1)}$$

where B_1 is the flux density for a rectangular block magnet at distance $x_1 = (d/2 + x)$, B_2 is the flux density for a rectangular block at distance $x_2 = (d/2 - x)$, d being the distance between the magnets. The field density was also dependent on the dimensions of the magnets (width W, length L, thickness T). The flux density at a distance x from a magnet was given as:

$$B(x) = \frac{B_r}{\pi}.\left[\tan^{-1}\left(\frac{W.L}{2x.[4x^2 + W^2 + L^2]^{1/2}}\right) - \tan^{-1}\left(\frac{W.L}{2\,(x+2T).[4(x+2T)^2 + W^2 + L^2]^{1/2}}\right)\right]$$

Therefore the flux density between two magnets at distance x1 from one and x2 from the other, from equation 1, would be

$$B = B(x_1) + B\,(x_2)$$

=> The flux density experienced by our specimen sitting at a distance x_1 and x_2 from the magnets is:

$$B(x) = \frac{B_r}{\pi}.\left[\tan^{-1}\left(\frac{W.L}{2x_1.[4{x_1}^2 + W^2 + L^2]^{1/2}}\right) - \tan^{-1}\left(\frac{W.L}{2\,(x_1+2T).[4(x_1+2T)^2 + W^2 + L^2]^{1/2}}\right) + \tan^{-1}\left(\frac{W.L}{2x_2.[4{x_2}^2 + W^2 + L^2]^{1/2}}\right) - \tan^{-1}\left(\frac{W.L}{2\,(x_2+2T).[4(x_2+2T)^2 + W^2 + L^2]^{1/2}}\right)\right] \qquad ---(2)$$

Therefore the magnetic flux density changed both as a function of the air gap and also across the air gap at set gap distance. Calculations showed that the magnetic flux was highest at the surface of the magnets and the next highest at the center of the air gap. Since it is not possible to have a hot specimen in contact with the magnets, the latter is chosen. Figure 3.3 is a calculated plot of the magnetic flux density at the center of the gap for different air gap distances.

Karlsdottir et al [2] used an AC power supply, therefore the Lorentz forces (I×B) in the DC magnetic field of the permanent magnets would be cyclic with frequency same as the AC power, that is 60 Hz. Therefore this circuit can be used for fatigue testing. To generate a continuous load, the DC magnetic field has to be coupled with an electric supply for DC current. For EMMA1, we used a manually controlled DC power supply (courtesy of Prof. Diann Brei, Mechanical Engineering, University of Michigan) through which flexural creep at ultra high temperatures was achieved. Figure 3.4 is a top view of the ribbon apparatus inside the magnetic flux assembly. Since this set up is done in open air, all the EMMA1 tests yield oxidative creep results.

Figure 3.5 shows an incandescent hot sample of ZrB_2-29%SiC-3% Y_2O_3 at 1750 °C in this set up while undergoing creep test. The stress on this sample was calculated, using Equation 5, to be 20 MPa. The image captures the clear deformation of the sample which was about 3mm after 240 seconds of test duration. In terms of strain, this is equivalent to 0.175. This gives the approximate creep rate to be 9×10^{-6} /sec, in the same range as Talmy et al.'s conventional results for ZrB2-50% SiC at 1600 °C. [3]

Further creep tests at isothermal and iso-stress conditions with varying time durations were used to understand the time dependent creep behavior. For a given fixed temperature and constant specimen geometries, the current was constant and by maintaining same separation between the permanent magnets, the magnetic field could also be maintained constant. Figure 3.6 shows the creep strain in ZrB_2-29%SiC-3% Y_2O_3 sample at 1600 °C under 20 MPa stress as a function of time. The curve shows a larger initial slope which gradually reduced reaching a steady state value. This behavior seems to indicate the transition from primary creep domain with reducing creep rates to secondary creep domain with a steady minimum creep rate. This transition time point could be noted from the graph to be ~ 200 seconds after the load is placed.

Several more in-air creep tests were performed using EMMA1 at 1600-1900 °C, temperatures higher than any existing conventional testing literature. The specimens showed obvious creep deformation, thereby demonstrating the feasibility of using electromagnetic forces for flexural creep testing of UHTCs.

3.2 Design and Fabrication of Beta-Prototype Apparatus

For the II-Phase of this project, a more sophisticated apparatus intended as an easy-to-use, pre-commercial product was designed. This beta-prototype apparatus was called EMMA2 which is substantially improved from the cruder previous version EMMA1. This section discusses the design and fabrication of EMMA2.

3.2.1. Magnetic Flux Assembly

The magnetic flux assembly assembled out of permanent magnets inside brass fixtures bolted to machinist vice in EMMA1 is replaced with an electromagnet. Albeit bulkier, electromagnets can reach much higher magnetic flux density, above 1 Tesla, and provide better control of the flux density. In an electromagnet, the magnetic flux density can be varied by changing the air gap distance as well as altering the current passing through the coils – we use the latter method. This allows the entire assembly to be fixed in place, hence the possibility to be enclosed, and still manipulate the magnetic flux.

The electromagnet, model EMU-75, procured from Silicon Valley Science Labs (Saratoga, CA) is a U-shaped soft iron yoke with dead annealed soft iron pole pieces. The pole pieces are 75mm in diameter. The air gap is continuously variable from 0-75mm with two way knobbed wheel screw adjusting system. The energizing coils are wound on non-magnetic formers with uniform layers of S.E. grade copper wire. A power supply DPS-175 designed to be used with EMU-75 as a constant current power supply allowing smoothly adjustable current in the range 0-3 Amperes per coil, i.e., a total of 6Amps coil current. Figure 3.7 is a photograph of the electromagnet showing the pole pieces, yoke, the wheel screw system and the constant DC power supply that supplies current into the coils. The flat pole pieces would generate a magnetic field up to 10 KGauss or 1 Tesla with the maximum 3 Amps current and an air gap of 10 mm. [4] To amplify the flux density in the air gap further, the pole pieces were tapered. However, the higher flux

density comes at the expense of smaller uniform field space. The balance is struck by having the size of the tapered poles the same as the expected length of ribbons, 25mm.

The tapered pole pieces resulted in the magnetic flux density of 1.5 Tesla with 3 Amps current and 10mm air gap, a 50% increase from that by untapered/flat pole pieces The flux density in the center of the 10mm air gap was measured as a function of different amounts of current passed through the coils, as plotted in Figure 3.8. Compared with the magnetic flux assembly of EMMA1 which could reach only 0.34 Tesla, the flux density in the new electromagnet is 340% times larger. Thus the applied stresses in EMMA2 can be 4.4 times larger than in EMMA1.

3.2.2. Digital Gaussmeter

The magnetic field in the air gap of an electromagnet is more complex than that generated by the permanent magnets. Therefore theoretically calculating the flux density at a given location in the air gap is not easy. A digital gaussmeter based on the Hall Effect in semiconductors is employed to empirically measure the flux density at the ribbon location. It operates on the principle that a semiconductor carrying current develops an electromotive force when placed inside a magnetic field, in a direction perpendicular to the direction of both electric current and magnetic field. And the magnitude of this E.M.F. is proportional to the field intensity if the current is kept constant. The DGM-103 model shown in Figure 3.9 can measure in the range 0-20 KGauss with a resolution of 1 Gauss.

3.2.3. Controlled DC Power Supply

The DC current supply used in EMMA1 was borrowed and also with a manual control. A pyrometer was used to measure the temperature of the ribbon surface and the current was adjusted accordingly by hand. The manual operation limited the extent of control and relatively large temperature fluctuations of the order of ±50 °C were inevitable. This situation is remedied by a control-loop with a PID controller to modify the current driven by the DC power supply to maintain constant temperature of the ribbon.

The control loop, depicted in Figure 3.10, consists of the pyrometer reading the temperature of the ribbon and feeding it to the PID controller, which then depending on the difference between this measured value and the set point generates an error signal to give out a control output to the DC power supply and it modifies the output current accordingly. We used a Eurotherm PID temperature controller, model 2408, and Mikron Infrared pyrometer, model MS-140, that can measure from 900-3000 °C. The current required to heat the ribbon specimen from 0-3000 °C ranges between 0-60 amperes. However, the UHTC materials being conducting required small voltages 2-4 volts even for the long ribbons. Therefore, the power supply should operate in small voltages and large amperage.

Therefore a 1500W TDK-Lambda DC Power Supply, model Genesys Gen 12.5-120 was obtained. It operates in 0-120 Amps and 0-12.5Volts completely suitable for our

heating requirements. Additionally a programmable feature is also indispensable to perform in the control loop. Figure 3.11 is a photograph of the power supply coupled with the temperature controller during a heating test. The bottom value indicates the set point and the top value indicates the measured/point value of temperature in degrees Celsius. They both are designated at 1500 °C since the steady state of temperature was reached. It could be noted from the power supply's display that 58 amperes of current and 3 volts were required.

3.2.4. *In Situ* Deflection Measurement

In conventional flexural creep tests, the fixture that applies the load has a location sensor and thus tracks the mid span deflection as the sample deforms. However the fixtures being in contact with the hot material place a major limitation on temperature of testing. EMMA was designed to overcome these constraints by working with non contact forces and thus can operate at ultra high temperatures. Therefore any deflection measurement system in EMMA should also necessarily be non-contact.

Previously in EMMA1, the mid-span deflection was measured after the creep test. To have *in situ* deflection measurement is more practical because a single isothermal, iso-stress test can collect the required information instead of several such experiments with varying time durations. Some of the non contact measurements techniques include:

a. Microscopy: EMMA is table top and compact equipment where the deforming sample is out in the open and visible to the eye. However, the pole pieces of the

electromagnet block the side view of the sample. Therefore the microscope view would be skewed and although such a view could be calibrated into real measurements, owing to the uncertainty in repeating the exact position for all the tests, this technique was not pursued.

b. Laser Micrometer: The completely unrestricted view of the sample in EMMA is from the top. Therefore the movement of the ribbon surface is along the line of sight. Such a displacement is usually hard to measure. Therefore laser triangulation principle is employed.

Laser triangulation sensors determine the position of a target by measuring reflected from the target surface. A 'transmitter' (laser diode) projects a laser spot on the target, and its reflection is focused via an optical lens on a light sensitive device or 'receiver'. If the target changes its position from the reference point, the position of the reflected spot of light on the detector changes as well. Schematic of triangulation laser measurement system is depicted in Figure 3.12.

The receiver is the most critical component of laser micrometers and it is typically a Charge Coupled Device (CCD). A CCD is a digital pixelised array detector, as shown in Figure 3.12, with discrete voltages representing the amount of light falling on each pixel of the detector. It finds the one single pixel with the highest light intensity and identifies this as the spot of the reflected laser light. The signal conditioning electronics detect this spot position and, following linearization and additional digital or analogue

signal conditioning, provides an output signal proportional to position of the target surface.

In high temperature applications, there is another radiation involved, i.e. the incandescence radiation of the hot objects. Thus the light reaching the CCD panel is composed both of the reflected laser and that of incandescence. Since the CCD cannot discern between the two, the functioning of the laser depends on the dominating radiation. If the laser power exceeds the incandescent radiation reaching the CCD, the pixels where the laser hits still record the highest intensity and the incandescence becomes background noise. Then the laser performance will be accurate. On the other hand if the incandescence is larger, the pixel which is closest to the hot object or "sees" most of that radiation is identified as the spot. Then the output of the location of the target surface corresponds to this wrong pixel. The laser will not be able to establish the target surface.

Thus, the comparison of laser power with incandescent radiation is critical to the viability of laser micrometers as an *in situ* deflection measurement system for EMMA. Commercially available class-II lasers have a power of ~ 5mW, which can be operated in the open. The other classes of lasers with higher energies will have to be accompanied by extreme safety gear. Therefore class-II is preferred and the following comparison assumes the laser power to be 5mW. The incandescent radiation emitted by unit area of a hot surface is described by Planck's law [8] to be both temperature and wavelength dependent, the Matlab-generated surface plot of which is depicted in Figure 3.13:

$$I(\lambda, T) = \frac{2hc^2}{\lambda^5} . \frac{1}{\left(e^{\frac{hc}{\lambda kT}} - 1\right)} \quad ---(3)$$

The radiation reaching a certain spot on the receiver is a multiple of I with the solid angle the emitting surface subtends at the receiver point.

$$P_s = \Omega . A . \int_{\lambda_{min}}^{\lambda_{max}} I(\lambda, T) . d\lambda$$

where A is the area of the emitting surface Ω is the solid angle. Since the CCD pixels record radiation at every wavelength, the incandescence radiation has to be integrated across the entire black body radiation spectrum. Hence the integration limit, λ_{min} -> λ_{max} , is 0 -> ∞. When the distance between the sample and the receiver is much larger than the emitting area, then the solid angle subtended can be approximated as:

$$\Omega = \frac{A}{4\pi R^2}$$

$$P_s = \frac{A^2}{4\pi R^2} \int_{\lambda_{min}}^{\lambda_{max}} I(\lambda, T) . d\lambda \quad ---(4)$$

This model predicts that the incandescent radiation reaching the sensor increases almost exponentially with temperature, as shown in Figure 3.14. It predicts that above 1850 K or ~ 1600 °C, the incandescence exceeds the laser power. A regular industrial red laser from Keyence, model LK-G 157, was capable of establishing the position of a ribbon sample surface at 1600 °C, but at 1750 °C showed larger incandescence leading to erroneous results. Figure 3.15 is a screen shot taken of the intensities recorded by the array of pixels in the CCD. The x-axis of the graph is the panel location of the CCD

receiver and the y-axis is the intensity of light reaching that panel. At room temperature, the laser micrometer showed the position of the sample to be corresponding to reflected laser light reaching, panel-A. With the sample undisturbed, but resistively heated to 1750 °C, the broad incandescent radiation peak reaching over a large area of the CCD is seen. The signal electronics now detect the peak in that radiation, panel-B, and predicts the corresponding distance as the sample location.

Laser micrometers for ultra high temperature applications are rare and expensive, but operate exploiting the dissimilarities between the incandescence and laser radiations to distinguish and eliminate the incandescence. There are two important differences between the characteristics of the two radiations.

i. The laser beam is a single wavelength radiation where as the incandescence is similar to black body radiation, spanning the entire wavelength spectrum**.** Therefore optical filters can be used to eliminate incandescence in other wavelengths.

ii. The incandescent radiation is not uniform across the wavelength spectrum but has temperature dependent peak intensity. The wavelength at which peak intensity occurs decreases with increase in temperature. Planck's model predicts that the peak radiation from an object at 1000K occurs at 2901 nm while that from an object at 2500K occurs at 1160 nm. Figure 3.13 shows that below 500nms the incandescence is very little. Therefore ultra high temperature applications seek lasers that operate at blue/violet wavelengths, with filter to block the other wavelengths and thus most of the incandescence.

iii. The laser is also a spatially focused light beam. The reflected laser typically hits very few pixels and hence is a sharp peak in the intensity vs. panel graph. The incandescence is emitted from the source object in all directions, it spreads radially outward. Therefore incandescence will be a wide peak covering large portions of the receiver. Smart signal electronics can detect such large peaks, generate a modeled intensity peak and eliminate that to leave the laser spot.

A high accuracy blue laser sensor, model MRL-DS, working at a wavelength of 405nms with an inbuilt optical filter was procured from Metrology Resource Co [9] as the *in situ* deflection measurement system for EMMA. This *in situ* measurement technique apart from the time efficient data collection has further advantage of higher resolution than a naked eye. This particular model has a resolution of 10 microns, however more expensive models with resolution < 1micron are available. Data collection from the beginning of the test is beneficial since the primary creep domain can also be observed. The tertiary creep domain is rather short as the sample failure is quick. The exact time when the tertiary creep starts is hard to register with eye observation. High resolution *in situ* measurements can pin point the time duration of creep before the destructive tertiary domain sets in, which is an important mechanical characteristic from a designing perspective.

3.2.5. Sample Holder Set Up

The components of the equipment that hold the resistively heated ribbon sample in the magnetic field were collectively called the sample holder set up. Karlsdottir et al.'s [2] previous design, composed of silver plate contacts on which the thick ends of the sample were held on with alligator clips, was used in the EMMA1 prototype. But this system had several draw backs. (See Figure 3.4)

i. The magnetic flux density in the electromagnet decreases exponentially with increasing air gap distance. Realizing a magnetic flux density of > 1Tesla requires the air gap to be of < 10mm. The silver plate-alligator design's width is 40mm and fails to comply with this space constraint.

ii. Replacing the samples after each test required the disassembly of several components and reassembly with the new sample. This process is time consuming and not desirable in a commercial apparatus.

iii. Although the alligator clips were made of copper, a non magnetic material, the springs were steel and were subject to attractive forces in the magnetic field. Movement of the clips was further augmented when the heat transfer from the thick ends reduced the spring constants. This has several undesirable consequences, such as loss of contact with the silver plates ceasing the test or erratic variations in the behavior of the end supports. The alligator clips if properly functioning are expected to act like fixed/pinned ends whereas the lateral movement makes them roller-end type. This can cause significant impact on the

stresses experienced by the thin section/ribbon, as will be explained in detail in chapter 4.

iv. The large current densities employed in EMMA require current supply cables to be 2-4 AWG gauges. These thick cables have large stiffness with the capability to shift the position of the entire sample holder attached to them during a test, leading to unpredictable variations in the Lorentz load.

This compels the need to design a new sample holder set-up that will overcome the above concerns for the next beta prototype. This design was envisioned to be a slide-in design with two separable components, Part 1 and Part 2 the schematics of which are illustrated in Figure 3.16. Part 1 consists of two supports (Part 1-A) to hold up the ribbon in the gap between them. Their bases are attached to an electrically insulating and high temperature (400 °F) resistant material like Transite cement board or MACOR or Phenolic (Part 1-B). These supports are not simply standing on this board, but pass through slots made in it and glued with high temperature (450 °F) epoxy. Therefore they leave two electrical contact points underneath Part-1.

The whole Part-1 slides onto the larger structure (Part 2) made of similar material as the Part1-B with electrical cables attached to the spring loaded contact points (Part 2 - A) on its surface. These cables are attached to the DC power supply, therefore the two contact points act as the interface for current supply. As the Part 1 slides into place these two electrical contacts touch the bases of the pillars completing the electrical circuit. This structure is attached to the yoke of the bulky electromagnet (280 lbs) Part2-B.

Two versions of Part 1 were designed. The first design attempted, depicted in Figure 3.17, was two brass pillars with grooves for the thick ends of the sample to sit in. It had two brass lids (that also can fit into the slots) to hold the sample in the groove. An L-bracket fitted to the brass pillar had a thumbscrew to apply vertical force on each lid and fasten the ribbon like a C-clamp. However, there was excessive heat conduction through the brass pillars, leading to large temperature gradients in the hot zone. As a result the region at target temperatures is much shorter (6mm) than the length of the thin section (37mm). This subsequently lead to lower creep rates that were unable to cause deformation. This problem was solved by reducing the cross-section of the support pillars which linearly reduced the path for thermal conduction. The second version of Part 1, depicted in Figure 3.18, was made from silver plates attached to thin copper pillars. The sample was fastened using alligator clips.

The effect of thermal conduction is illustrated by Figure 3.19 which showed the ribbons after creep testing at 2000 °C in both versions. The oxide scale formed on the UHTC at this elevated temperatures is usually non porous and white in color and therefore is easily distinguishable from the oxide scale formed at lower temperatures, ≤ 1800 °C. The length of the hot zone at 2000 °C was several folds larger in Version2 than that in Version1. Similarly, the deformation was evident in ribbon of Version2 which eventually lead to breaking of the sample. On the other hand the deformation in Version1 was insignificant.

All the components, other than Version2, of the set up were precision machined at Ltek industries, Ann Arbor, based on the assembly diagrams prepared in Auto CAD. A colored side view of the assembly drawing was illustrated in Figure 3.20 showing the set up inside a 10mm air gap between the pole pieces of the electromagnet. The mechanism of current cables connection to the contact points in Part 2 was detailed. The O-ring terminal from the current cables was fastened between two brass bolts to a spring loaded brass screw. The top of the screw acted as the contact point for the Part 1.

This design solved all the issues of the previous design discussed above. The detachment of the sample holder from the rest of the equipment made new sample replacement convenient, eliminating the need to disturb any other components. The thick current cables from the power supply were attached to Part 2 fastened to the massive electromagnet and hence no longer a threat to sample immobility. The slide-in design had another benefit; it presents the opportunity to isolate the space around the sample location. Thus an environmental chamber inside which the atmosphere can be regulated as desired is made feasible. The related components are detailed in the next subsection.

3.2.6. Environmental Chamber

Rapid oxidation occurs when performing creep tests above 1800 °C. At such high oxidation rates, the thin cross section of the ribbon sample can not last long. This is not true for ZrB_2 and several ultra high temperature ceramics. High temperature creep testing in ambient air is typically accompanied by oxidation resulting in the formation of

complex oxide scales.[10-13] Figure 3.22 is an SEM image of the cross-section of a ribbon sample after 30 seconds of oxidative-creep testing at 2100 °C under a stress of 30 MPa showing heavy oxidation. After this point, the ribbon was oxidized through its thickness causing the test to cease. So oxidation during creep testing with EMMA has two fold effects:

1. The duration of the test is limited to the time before the sample is oxidized through its thickness. Since the oxide scales are not electrically conductive like the UHTC, the test will cease.
2. Large oxidation scales change the mechanical behavior of the ribbon itself. The stress and strains during the creep testing in EMMA, and any conventional test, are derived from elastic beam analysis. However, the presence of thick oxide scale on either side of the material and its different mechanical characteristics requires this to be treated as a cladding problem. The oxide scales are typically more brittle and cause faster failure, as was observed in the above mentioned test.

Therefore it is sometimes desirable to have nonreactive atmosphere during creep tests that are performed at temperatures above 1700 °C so as to understand the mechanical behavior of the material itself without interference from oxidation effects. This inspired the design and subsequent fabrication of an environmental chamber with controlled atmospheric conditions. This chamber was envisioned to be a completely enclosed space around the sample holder area, where the sample will undergo oxidation. It was made feasible by the slide-in design of the resistive heating set up where the

sample holder parts can be completely detached from the rest of the set up with the current leads to the DC power supply. A CAD diagram of the environmental chamber is displayed in Figure 3.23.

The environmental chamber required several ports to allow access for the current leads, outlet to vacuum pump, inlets for the target gas, oxygen sensor and pressure meter. It also needed a front door for the slide-in of sample holder and an IR-window on the top for the laser micrometer and the pyrometer to be able to record the sample. Apart from these, there were two large ports on either side were essential to allow the pole pieces of the electromagnet approach close to the sample. This was indispensable since the target air gap is about 10mm to be able to reach high magnetic flux densities of > 1 Tesla. Thus, although the design aimed for complete enclosure, there are inevitably several possible locations for leaks to occur in this system and need to be corrected. The amount of oxygen present in the chamber was tracked by an Illinois Instruments Oxygen Analyzer, model 910, and the gas flow designs include an unknown leak rate, $\dot{V}_{Leak}$. Two different gas flow set ups were attempted to purge the ambient atmosphere inside the chamber and replace it with non-oxidizing gas like Nitrogen. One of these utilized a vacuum pump to aid in the faster purge of the existing atmosphere, and the other gas flow set up relied on gas exchange.

a. Arrangement 1:

This set up included three major components: a nitrogen cylinder to supply the inlet gas, a vacuum pump that drew the atmosphere in the chamber and an oxygen sensor

to record the oxygen content in the chamber. The inlet gas is connected through a flow meter to regulate the in-gas flow rate. And the outlet to the oxygen sensor is fitted with a pressure gauge to read the pressure in the chamber.

The inlet gas flow rate was controlled through the regulator, hence $\dot{V}_{inlet}$ is a user defined variable. The suction rate of the vacuum pump depended on the pressure inside the chamber. But as the pressure gauge did not record any noticeable fluctuation in the internal pressure, $\dot{V}_{Vacuum}$, can be assumed to be a fixed quantity, corresponding to atmospheric pressure. Flow rate through the sensor, $\dot{V}_{Sensor}$, cannot be directly controlled but will depend on the pressure conditions inside the chamber. The flow meter in the sensor records this value. The fourth possible gas flow is the unknown leak rate, which will depend on the other three terms. All the gas flow rates coming into the system (the chamber) are counted positive and those going out as negative. Since no fluctuations in the chamber pressure were monitored, the gas flow is at balance.

$$\dot{V}_{inlet} - \dot{V}_{Vacuum} - \dot{V}_{Sensor} \pm \dot{V}_{Leak} = 0 \quad ---(5)$$

The sign of the leak rate term will depend whether the incoming gas flow is relatively larger or smaller than the outgoing flow. Let "*a*" be the ratio of gas inlet rate and vacuum pump suction rate, $a = \frac{\dot{V}_{inlet}}{\dot{V}_{Vacuum}}$. When $\dot{V}_{inlet}$ is set smaller than $\dot{V}_{Vacuum}$, i.e. $a < 1$, the system exists under slight vacuum and leak rate is positive with ambient air leaking into chamber. When $\dot{V}_{inlet} > \dot{V}_{Vacuum}$ or $a > 1$, the leak rate is negative and the atmosphere inside the chamber leaks to the atmosphere.

The gas exchange process inside the chamber can be treated as a continuously stirred tank reactor CSTR problem. [14] The volume of the EMMA's chamber, V is 2 ×10^{-3} m^3 and the vacuum pump rate $\dot{V}_{Vacuum}$ was measured to be 4 ×10^{-5} m^3/s. Then the oxygen concentration as a function of time for the two cases is given by:

$$x = 0.2 - 0.2\,a\left(1 - e^{\frac{\dot{V}_{Vacuum}}{V}t}\right) for\ a < 1$$

$$x = 0.2\,e^{\frac{a\dot{V}_{Vacuum}}{V}t}\ for\ a \geq 1 \qquad ---(6)$$

Figure 3.25 compares the results of these two scenarios in the plot of oxygen concentration as a function of time for different values of *a*. When a < 1, since ambient air is leaking in there is a lower limit on the oxygen concentration = 0.2(1-*a*), as can be seen from the plot. Whereas *a* > 1 ensures leak rate is negative and oxygen content will fall exponentially with time.

b. Arrangement2:

The above set up could be simplified by removing the vacuum pump but the gas flow conditions were replicated - the nitrogen inflow rate was set larger than the gas flow rate going out through the sensor. This ensured the leak rate would be negative. This second set up relies entirely on gas exchange process to purge the chamber of oxygen with incoming nitrogen gas. The set up is illustrated in Figure 3.26. Since the oxygen sensor had no pump, the flow rate of the gas going out through the sensor, $\dot{V}_{Sensor}$, was much smaller than the incoming gas flow rate, $\dot{V}_{inlet}$. As a result the system is under

slight pressure which causes the leaking gas would be negative, $-\dot{V}_{Leak}$, or going out of the system.

$$\dot{V}_{inlet} - \dot{V}_{Sensor} - \dot{V}_{Leak} = 0 \quad ---(7)$$

This set up if considered as an CSTR problem is estimated to have an oxygen concentration as a function of time is given by:

$$x = 0.2\, e^{\frac{\dot{V}_{inlet}}{V}t} \quad ---(8)$$

which is similar to the second case scenario of the earlier set up. So either of the two set ups can be used to purge the ambient air with desired atmosphere. Figure 3.27 shows the empirical oxygen content measured by the oxygen analyzer as a function of time for a =1.2, i.e. gas inlet rate of 6 SCFH or 4.8×10^{-5} m^3/s.

With the incoming gas as Nitrogen, the steady state oxygen content could be brought under 0.2% which is sufficiently low to suppress oxidation of the UHTC materials. Other gases like Ar+5% H_2 could also be used to replace the air in the chamber and bring Oxygen concentration even lower at shorter time durations. While Argon is considered non-reactive with UHTCs even at high temperature, Hydrogen would react with the oxygen in the chamber to form water vapor. The reactivity of oxygen with hydrogen is greater than that with hot UHTC and therefore the presence of hydrogen would prevent oxidation of the material. 5% Hydrogen is under the explosive limit. On the other hand water vapor is considered to affect the stability of the oxide scale of

UHTC. Both B_2O_3 and SiO_2 forming compounds such as $Si(OH)_{4\,(g)}$ suffer volatilization, thereby enhancing the oxidation rate.

An optical window with high transmission was embedded using an O-ring on the top plate of the environmental chamber so as to allow the laser micrometer and the micro-pyrometer to view the sample surface and record its position and temperature respectively. Despite the high transmission, the presence of the window in the optical paths affects the results of both the laser micrometer and the pyrometer.

The laser micrometer readings indicate a shift in the position of the sample surface despite the ribbon sample being stationary. This phenomenon can be explained by the refraction of the laser light at the two surfaces of the optical window. Figure 3.28 compares the optical paths travelled by the laser light in air and through the window. The double diffraction leads to a shift in the location where the laser light hits the CCD sensor and a corresponding shift in the sample positioning is recorded. However, since this shift does not vary with the working distance between the micrometer and the sample, it is not difficult to accommodate for this shift and obtain the real position of the sample from the shifted readings. Similarly, the optical window acts like a filter absorbing and reflecting some of the radiation from the sample from reaching the pyrometer. The pyrometer works by measuring the thermal irradiance from the hot object and identifies the temperature. Suppose the optical window has a transmission of t%, the irradiance seen by the pyrometer would be t% of the actual irradiance.

$$J_{shifted} = J_{actual} * \frac{a}{100} \quad ---(9)$$

where J is the irradiance given by $J = \varepsilon\sigma T^4$. So,

$$T_{shifted} = T_{actual} * \left(\frac{a}{100}\right)^{1/4} \quad ---(10)$$

Therefore an optical window of 91.1% transmission causes the pyrometer temperature to shift by 2.3% from the actual temperature. At elevated temperatures like 1500 °C, this corresponds to a difference of 35°C. Therefore this factor of $\left(\frac{a}{100}\right)^{1/4}$ was accounted for obtaining the exact temperature of the ribbon from the measured value.

3.3. Complete EMMA System

Figure 3.29 is a photo of the entire EMMA2, "Beta" version of the Electro Magnetic Mechanical Apparatus. It occupies about 2 meters of bench space including the power supply for the electromagnets (on left) and the power supply and control for the DC resistive heating current. The specimen in the environmental chamber, within the sample holder, is in the center between the poles of the electromagnet. The pyrometer for measuring temperature and the laser micrometer for measuring deflection are on rigid vertical supports. These supports are fabricated from standard Aluminum sections (80/20 Inc. Columbia City, IN) and rigidly attached to the heavy iron yoke of the electromagnet.

Operation of EMMA involves several steps:

i) Ribbon sample mounting on sample holder with alligator clips (~ 30 seconds)

ii) Sample holder inserted into the Part 2-A (~ 15 seconds)

iii) For controlled atmosphere testing – exchanging ambient air with desired gas (~ 3 minutes)

iv) Set electromagnet coil current for desired magnetic flux density (~ 15 seconds)

v) Check alignment of the pyrometer (~ 15 seconds)

vi) Apply specimen current to reach target temperature (~ 30 seconds)

vii) Creep test duration (1-5 minutes)

viii) Cool to room temperature (~ 1 minute)

The entire time duration of a creep test in EMMA is therefore only ~ 5-10 minutes. The total cost of the beta apparatus was approximately $25,000 and included several components of equipment which were either procured from vendors or custom designed. Major components include an Electromagnet which can attain a magnetic field of 1.5 Tesla, a Digital Gaussmeter to monitor magnetic flux density, a programmable DC power supply with a PID controller, an Infrared Pyrometer to measure the temperature, a violet Laser Micrometer to measure deflection *in situ* and an Oxygen Analyzer to monitor the oxygen content inside the environmental chamber which were purchased from manufacturers. Other components such as the slide-in sample holder, its base, the environmental chamber were precision designed using Computer Aided Design (CAD) and custom machined.

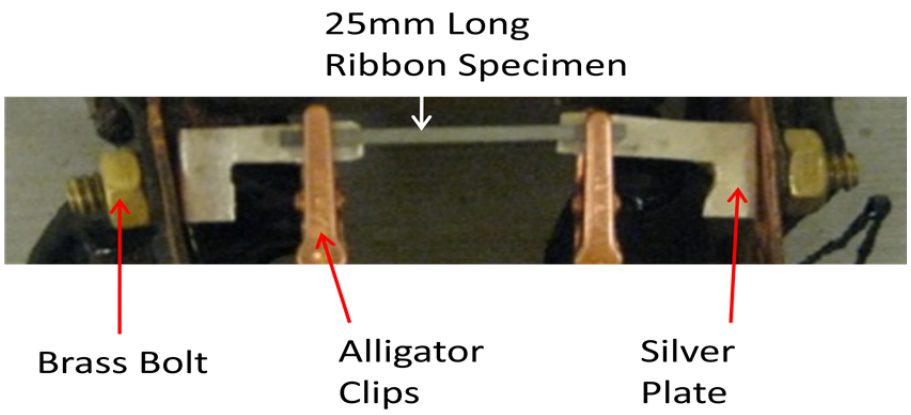

Figure 3.1: Image of the Ribbon Method set up with a long ribbon sample.

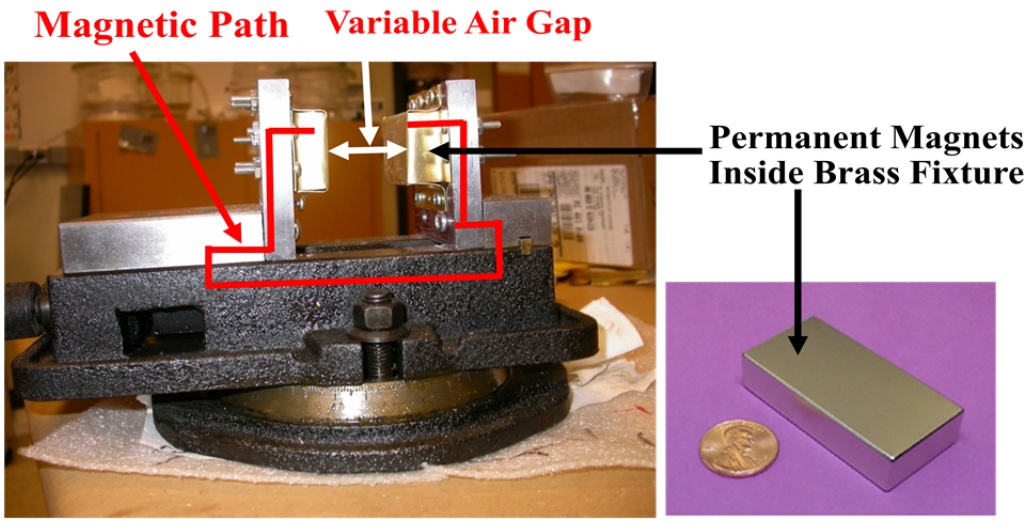

Figure 3.2: Left: EMMA1 Magnetic flux assembly, with two opposing Nd-Fe-B permanent magnets, attached with a brass fixture to rigid steel plates on a machinists vise. Right: Image of one Grade N52 NdFeB permanent block magnet with surface field of 6325 Gauss and $B_{r\ max}$ of 14,800 Gauss [1].

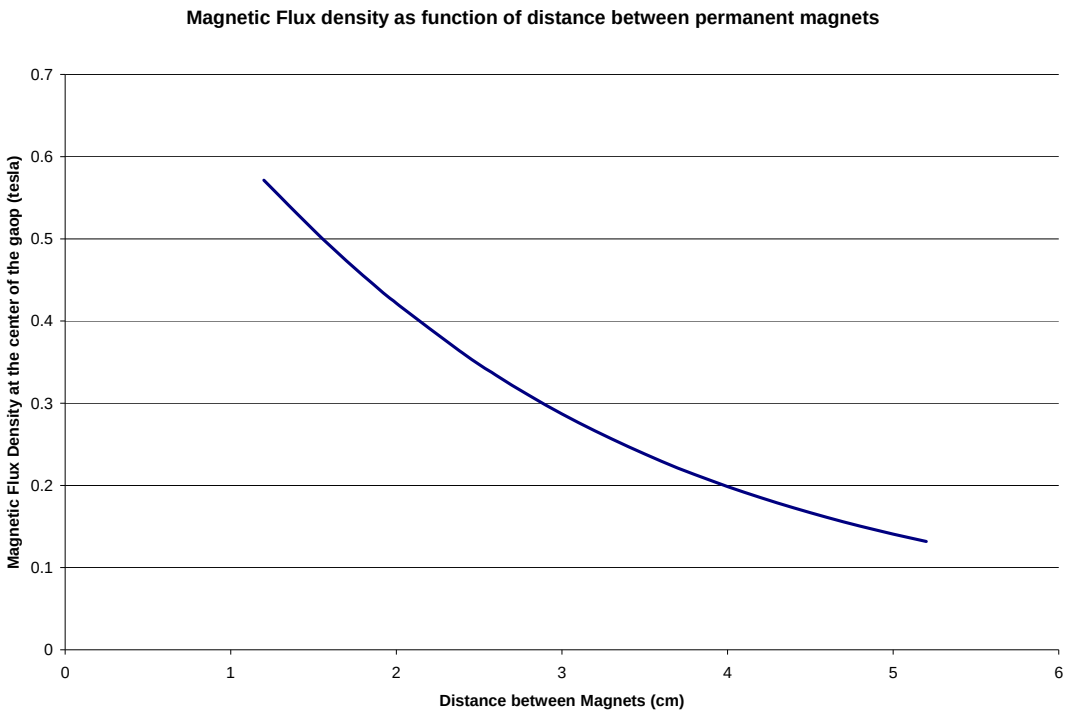

Figure 3.3: Mid-gap magnetic flux density vs. air gap distance for EMMA1

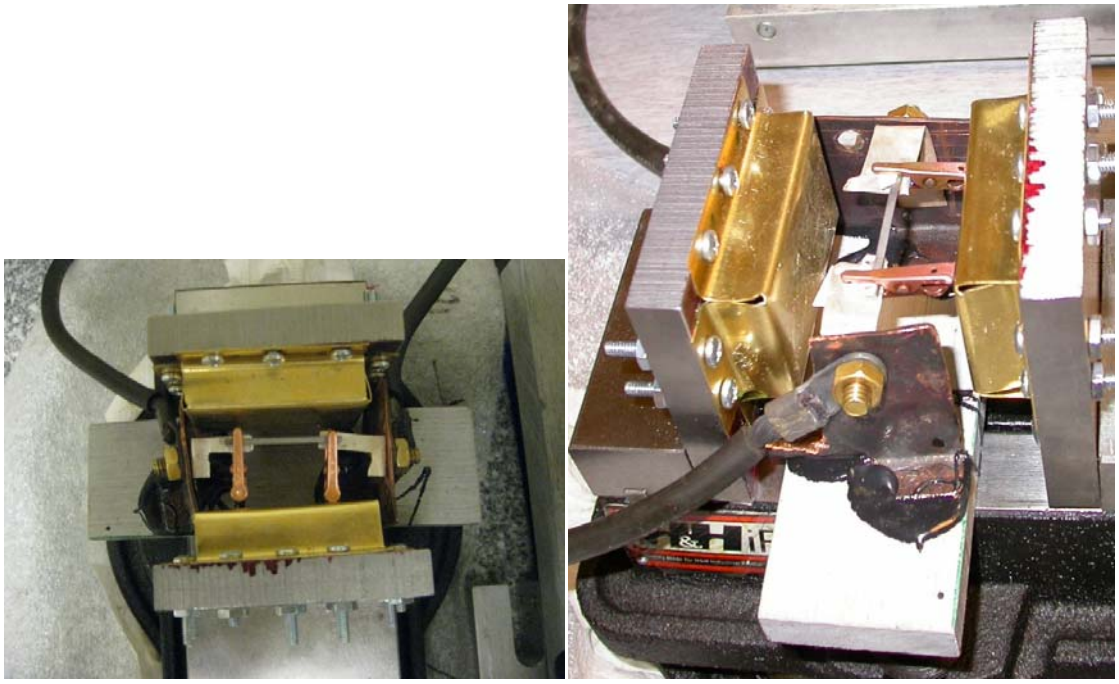

Figure 3.4: Top view of ZrB_2-SiC ribbon sample on the current conducting plate (L-shaped silver feature) in the gap of the EMMA1 magnetic flux assembly (Left) Side view (Right).

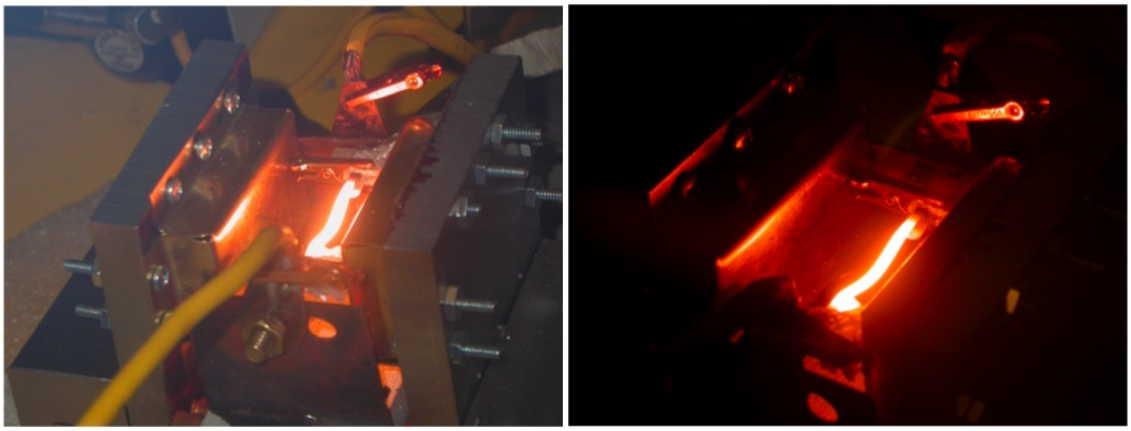

Figure 3.5: Deformed ribbon specimen in EMMA1 set up at 1750 °C under 20 MPa can be seen to be bent downwards and deflection is clearly visible. Both images show the same specimen but with lights ON and then OFF (for clearer perception).

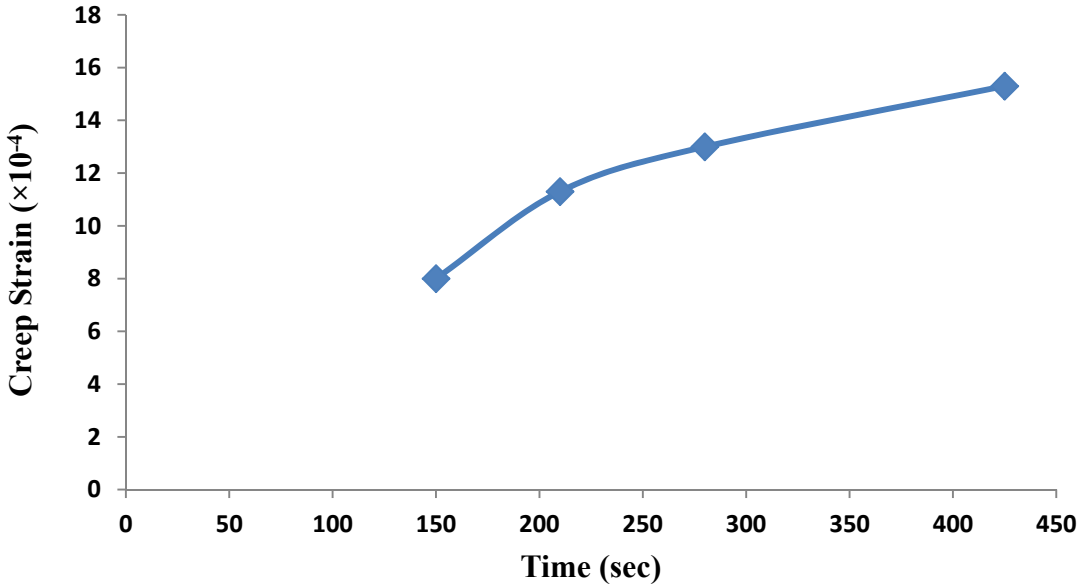

Figure 3.6: Creep strain vs. time graph at 1600 °C 20 MPa in EMMA1

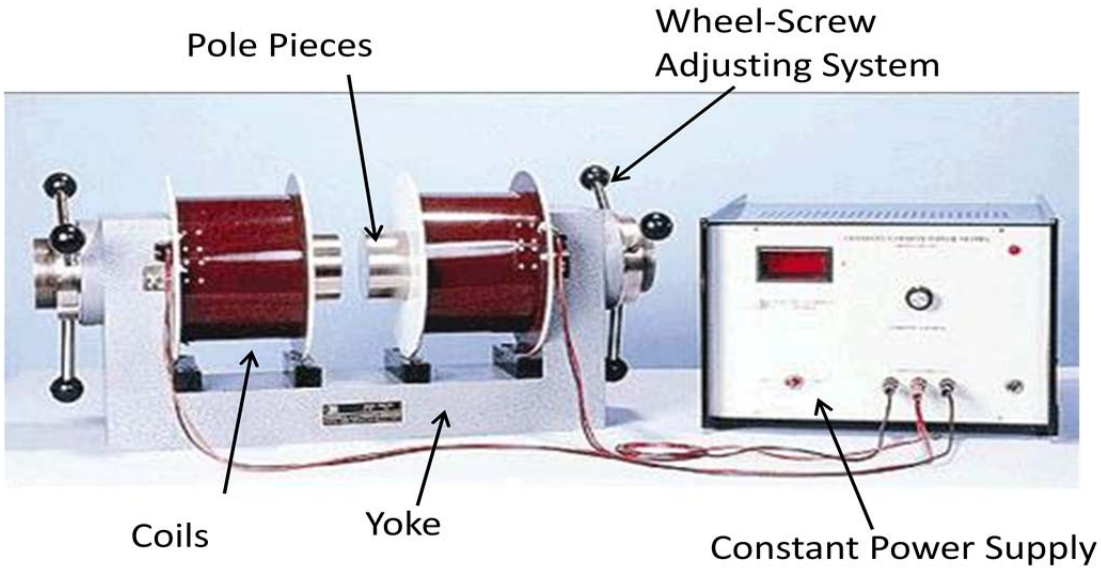

Figure 3.7: EMMA2 Electromagnet EMU-75 showing the pole pieces, yoke, wheel screw adjusting system and constant DC power supply DPS-175.[4]

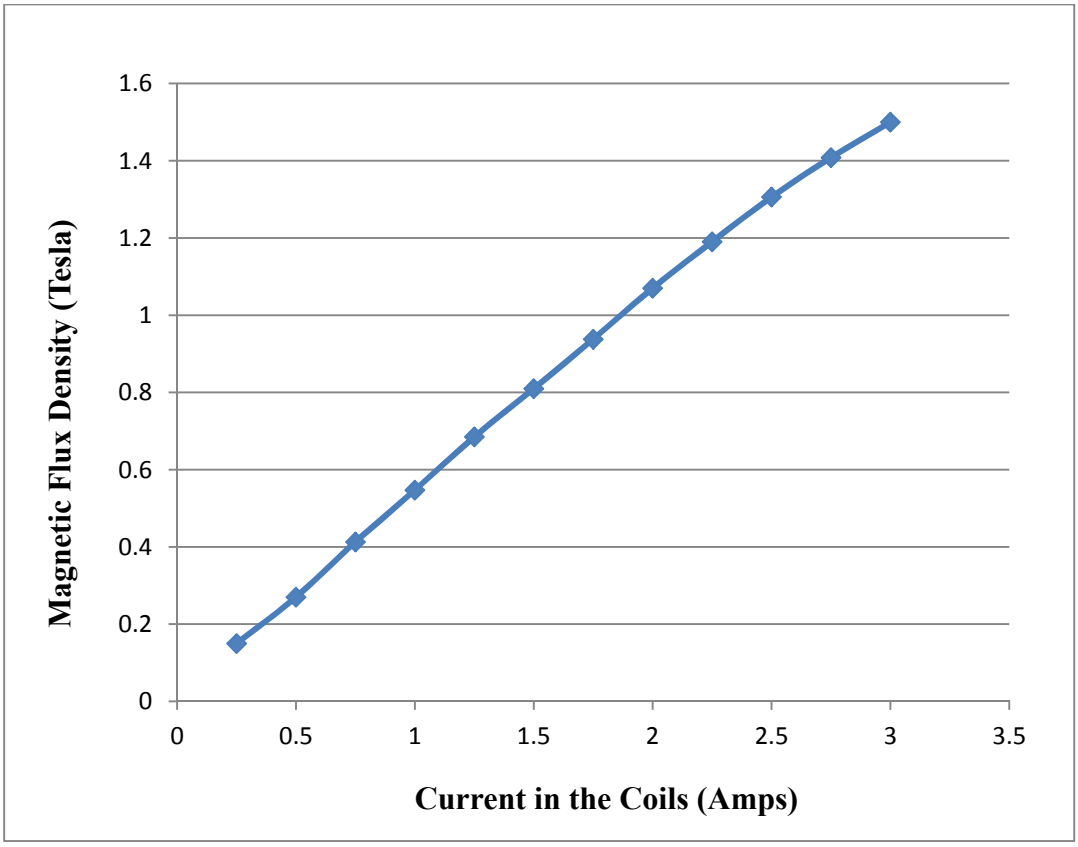

Figure 3.8: Magnetic flux density at the center of the 10mm air gap in EMU-75 with 25mm tapered pole pieces as a function of current in the coils. The maximum flux density achieved was 1.5 Tesla, 50% larger than that by untapered/flat pole pieces. The measurements were taken using a digital gaussmeter.

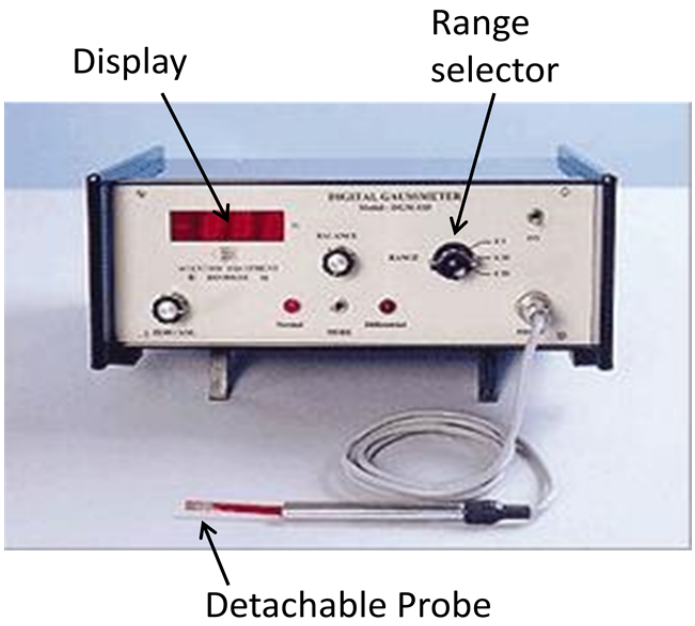

Figure 3.9: Digital gaussmeter– Model DGM 103 showing the probe and the display.

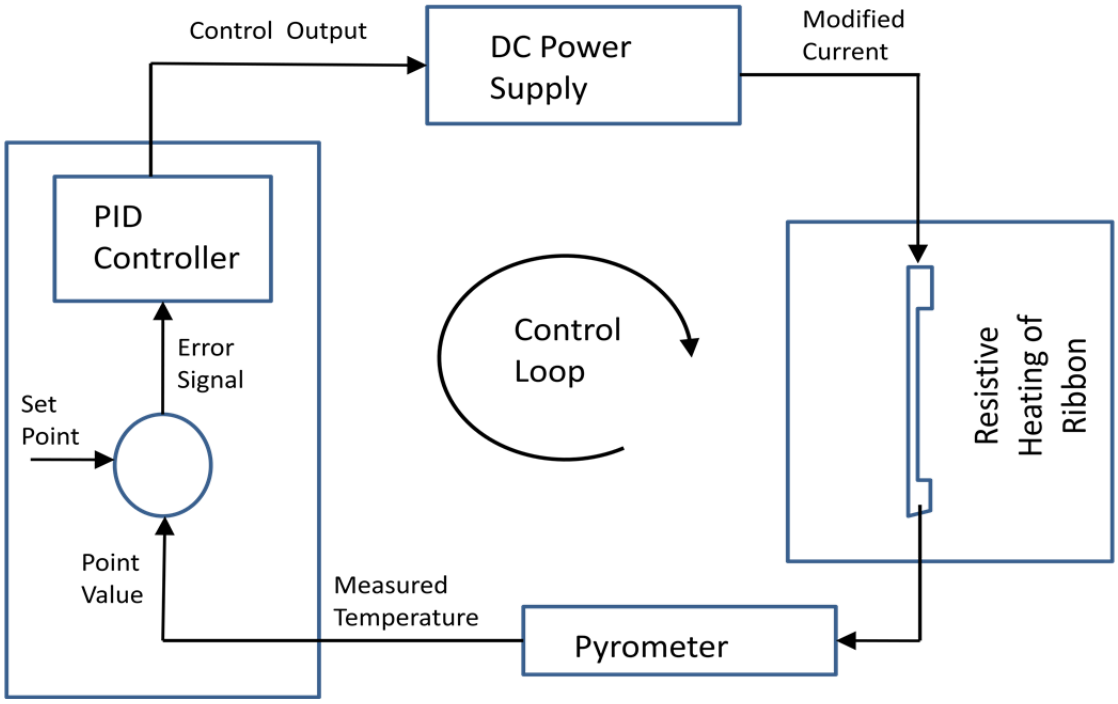

Figure 3.10: Temperature Control Loop with pyrometer to measure the temperature of ribbon and feed it to PID controller that sends corresponding error signal to DC power supply to modify the current for resistive heating of the ribbon.

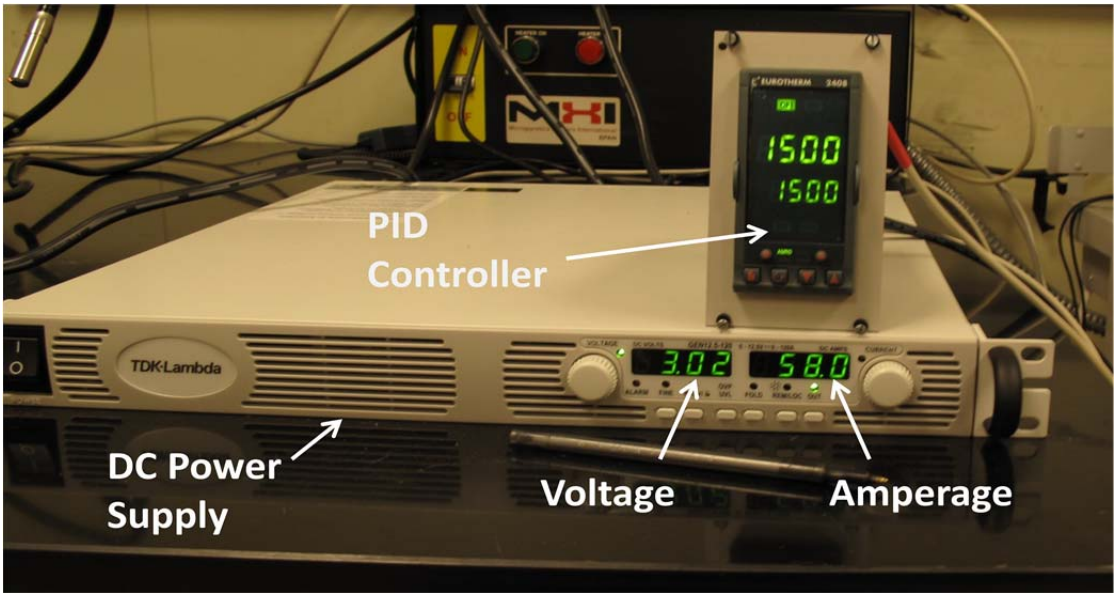

\

Figure 3.11: PID controller with DC power supply during a heating test at 1500 °C. Both the set value and the measured value indicate the same number since the steady state was reached.

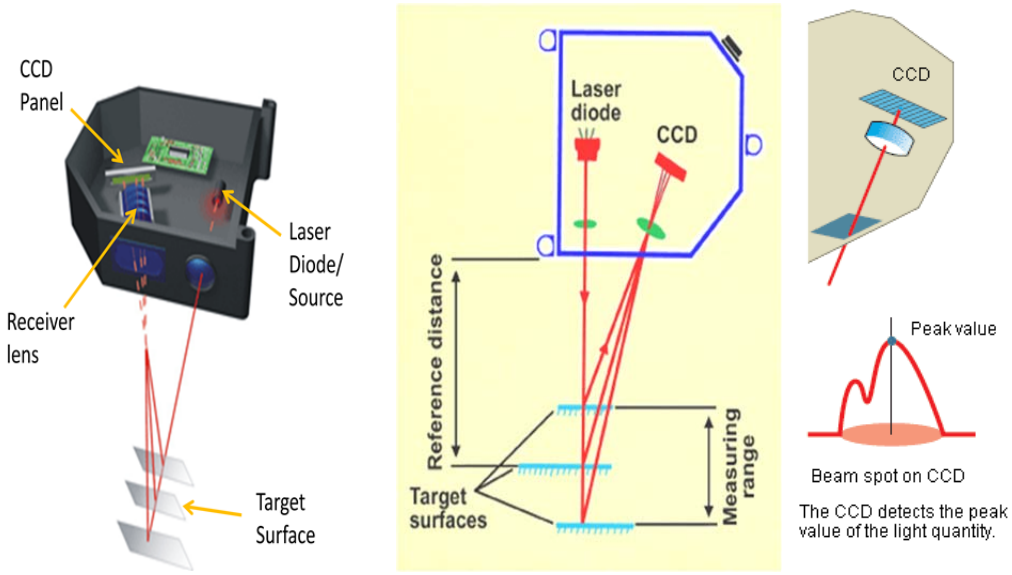

Figure 3.12: Schematics of a triangulation laser measurement system that can measure movement along the line of sight direction (Left). Reflected laser detection in a CCD (Right). [5-7]

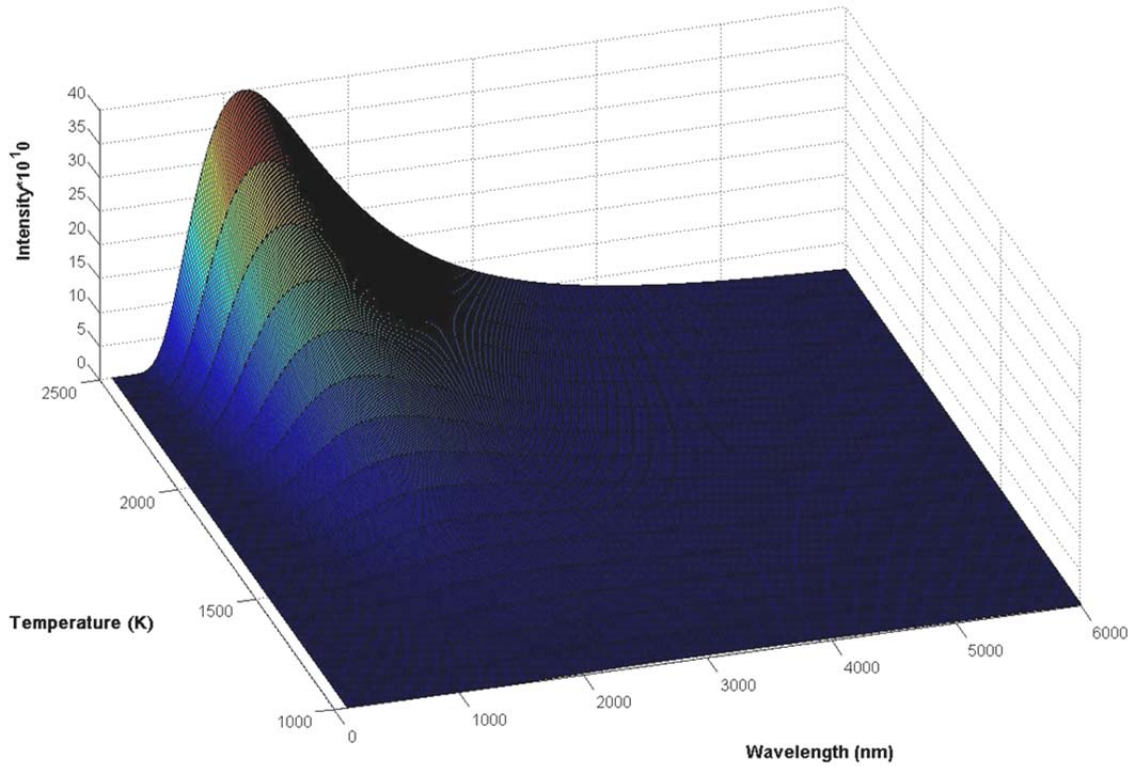

Figure 3.13: Matlab-generated surface plot of intensity as a function of temperature and wavelength.

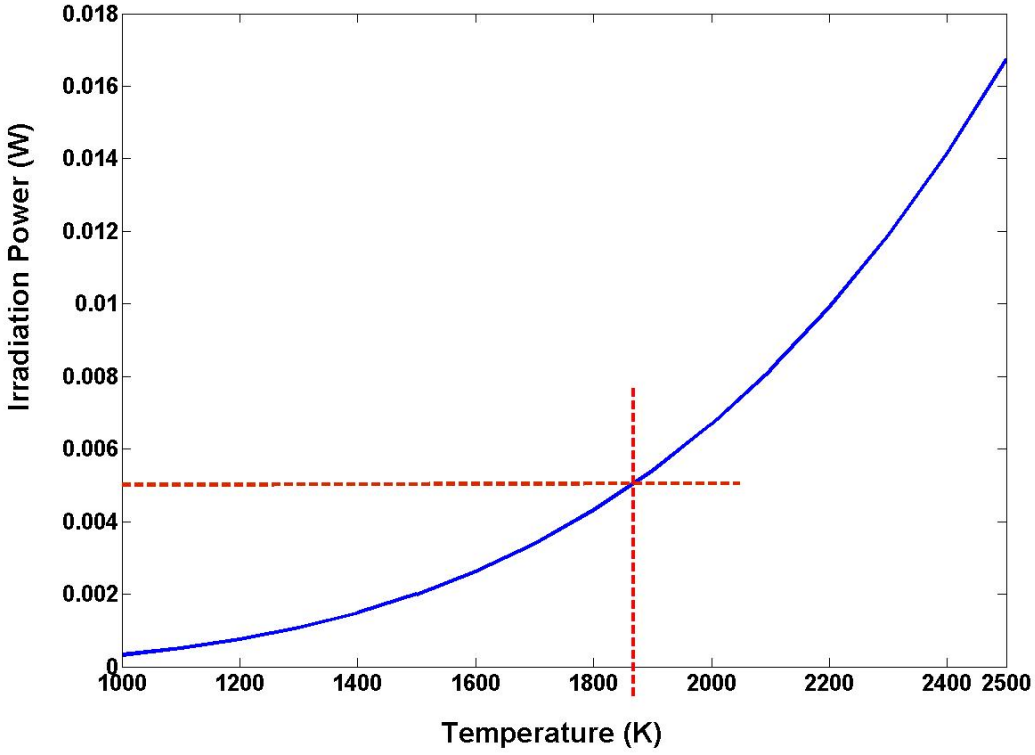

Figure 3.14: Incandescent radiation from hot sample in EMMA reaching the receiver in a laser micrometer at a working distance of 13.5mm, as a function of temperature.

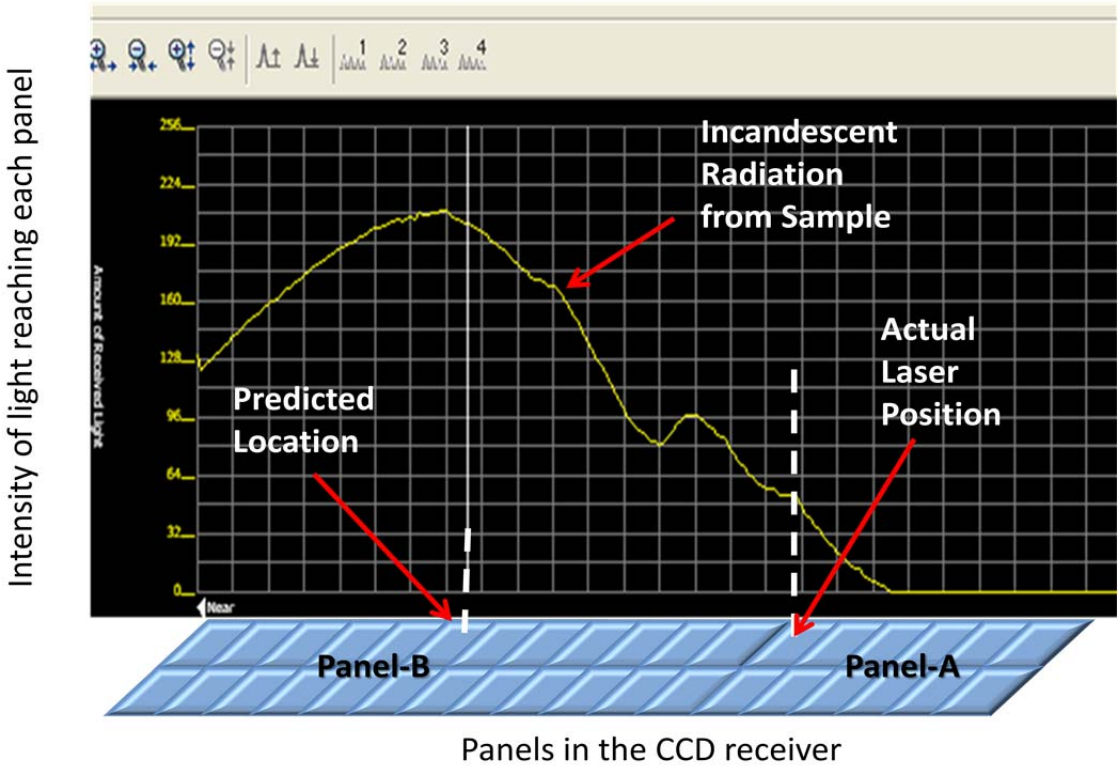

Figure 3.15: Snap shot of Intensities recorded by the array of pixels in the CCD receiver including a large incandescence as well as the reflected laser. The sample was 13.5mm away from the receiver and at a temperature of 1750 °C. The Figure also explains how the signal electronics predict the location of the sample corresponding to the panel-B receiving most of the incandescence instead of the reflected laser position.

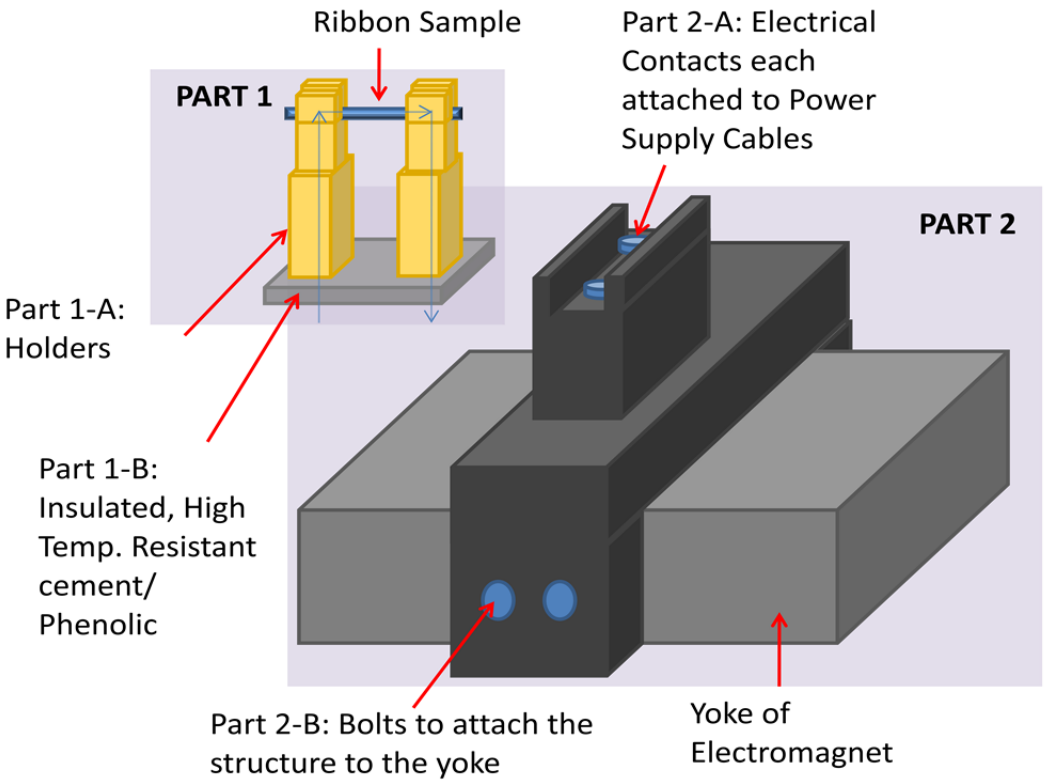

Figure 3.16: Schematics of the slide-in design of the new sample holder set up illustrating both the components, Part-1 and-2. Part-2 is attached to the yoke of the electromagnet where as Part-1 is detachable and can slide onto Part-2 surface with electrical contact points.

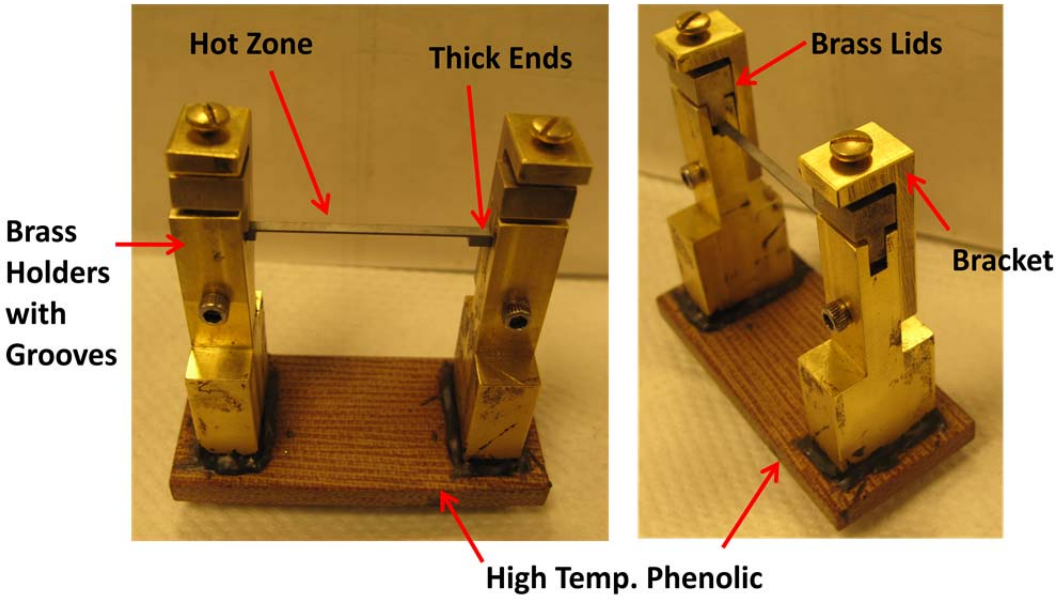

Figure 3.17: The first version of Part-1 made from brass support pillars and Phenolic. The grooves in the brass pillars fit the sample as well as the lids. The thumbscrew passes through the bracket, behaves like a c-clamp, and fastens the ribbon inside the groove.

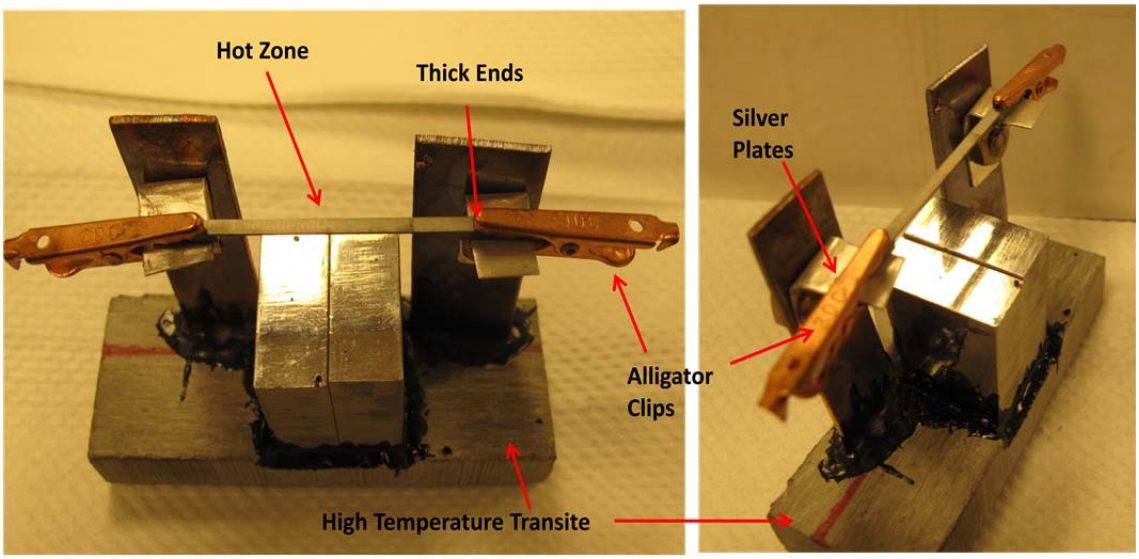

Figure 3.18: Version2 of Part-1 with reduced thermal conduction made from thin copper pillars with attached silver plates on which the ribbon is fastened with alligator clips.

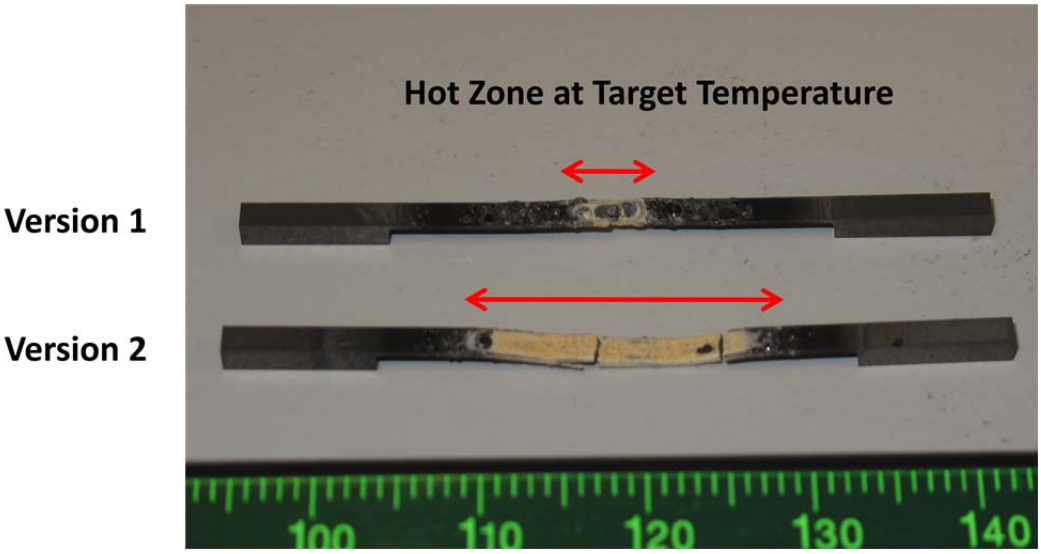

Figure 3.19: Photograph of ribbon samples after creep testing in air at 2000 °C in Version1 and Version2 to compare the length of the ribbon at target temperature. The white oxide scale forms only at ≥2000 °C and the oxide scale at lower temperatures looks very different, typically with bubbles.

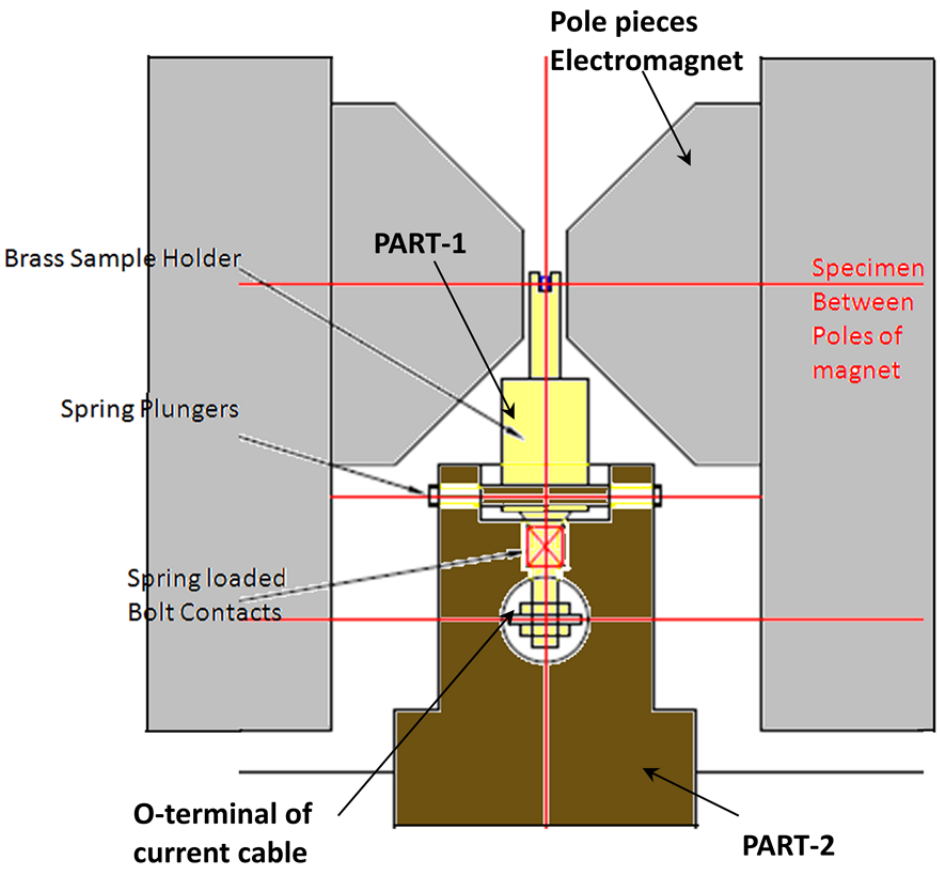

Figure 3.20: Schematic of side view of the sample holder set up in 10mm air gap between the pole pieces of the electromagnet in CAD.

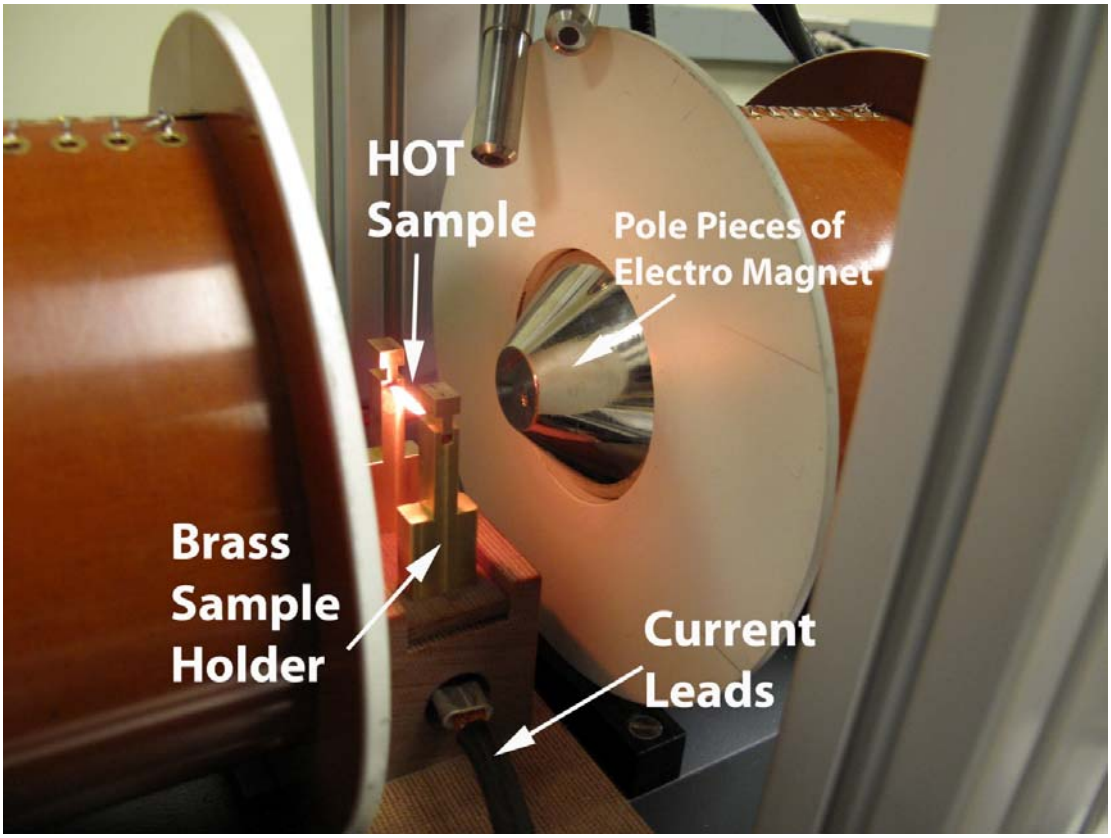

Figure 3.21: Photograph showing the sample holder set up while the ribbon is being resistively heated.

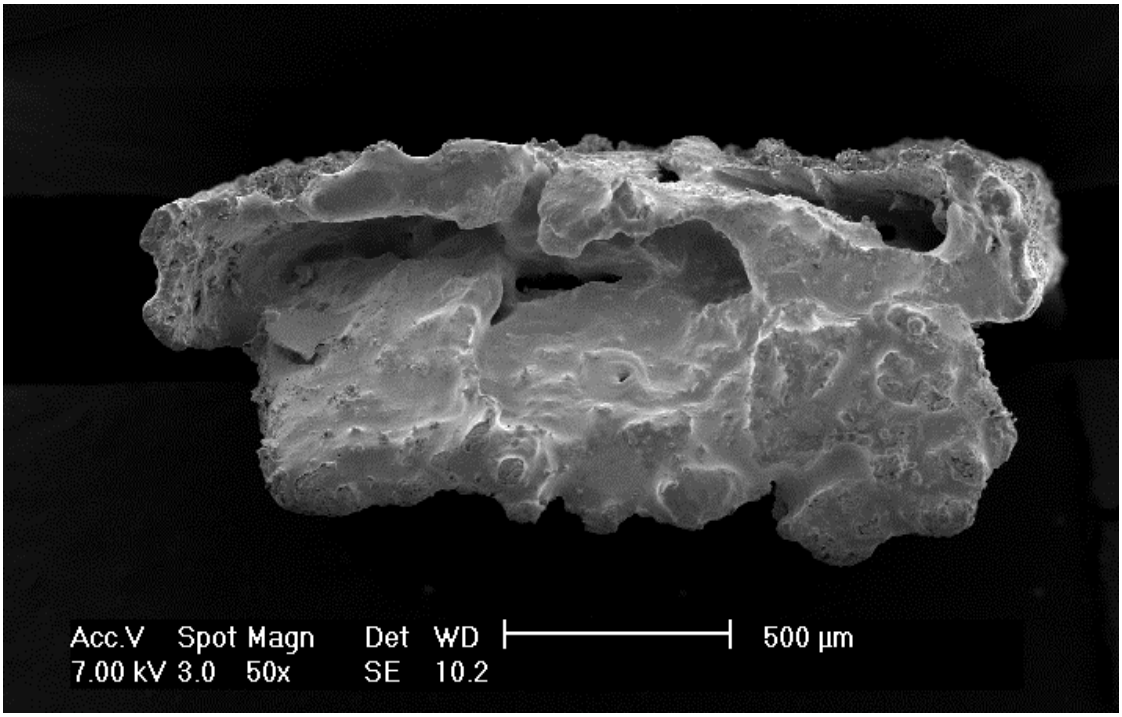

Figure 3.22: SEM image of the cross-section of a ribbon sample after 30 seconds of oxidative-creep testing at 2100 °C under a stress of 30 MPa

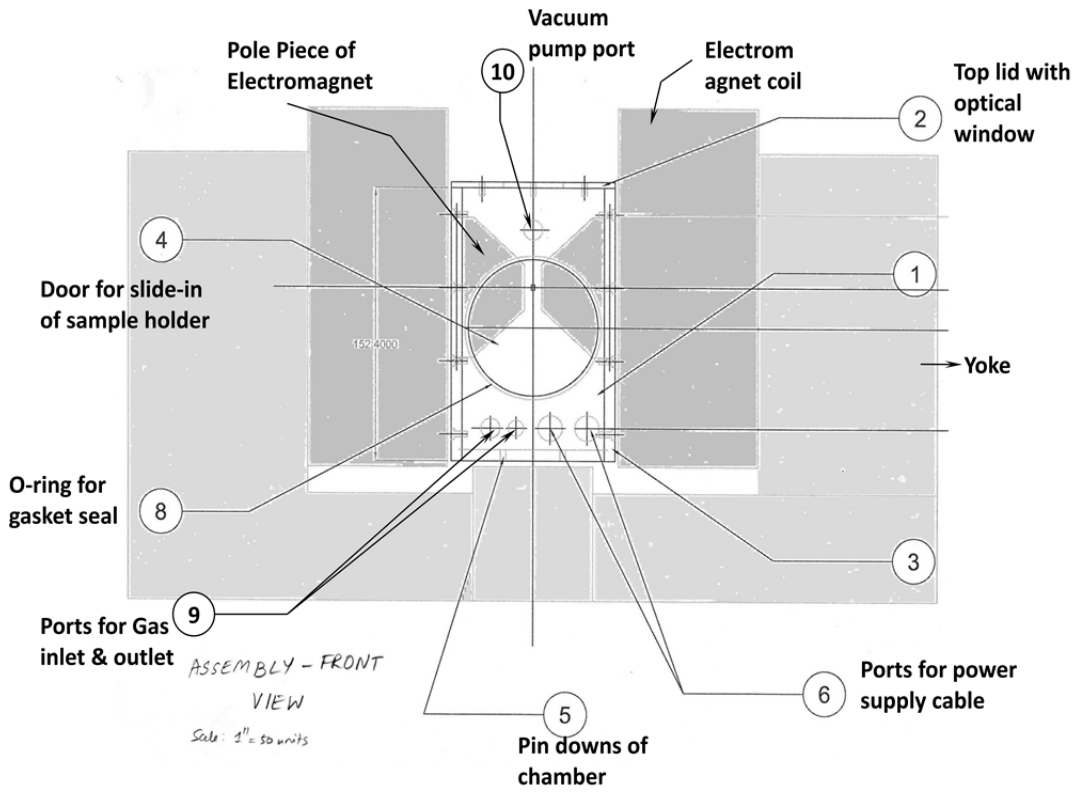

Figure 3.23: Color coded CAD image of the front view of the environmental chamber assembly. The pole pieces, yoke and the coils of the electromagnet are also depicted for better perception of the chamber dimensions. The several different ports to allow access for cables from power supply, gas inlet and outlet, vacuum pump and pole pieces are tagged. The slide-in sample holder is removed from this CAD image to avoid confusion, but presented in Figure 3.18 if the viewers intend to get the comprehensive picture.

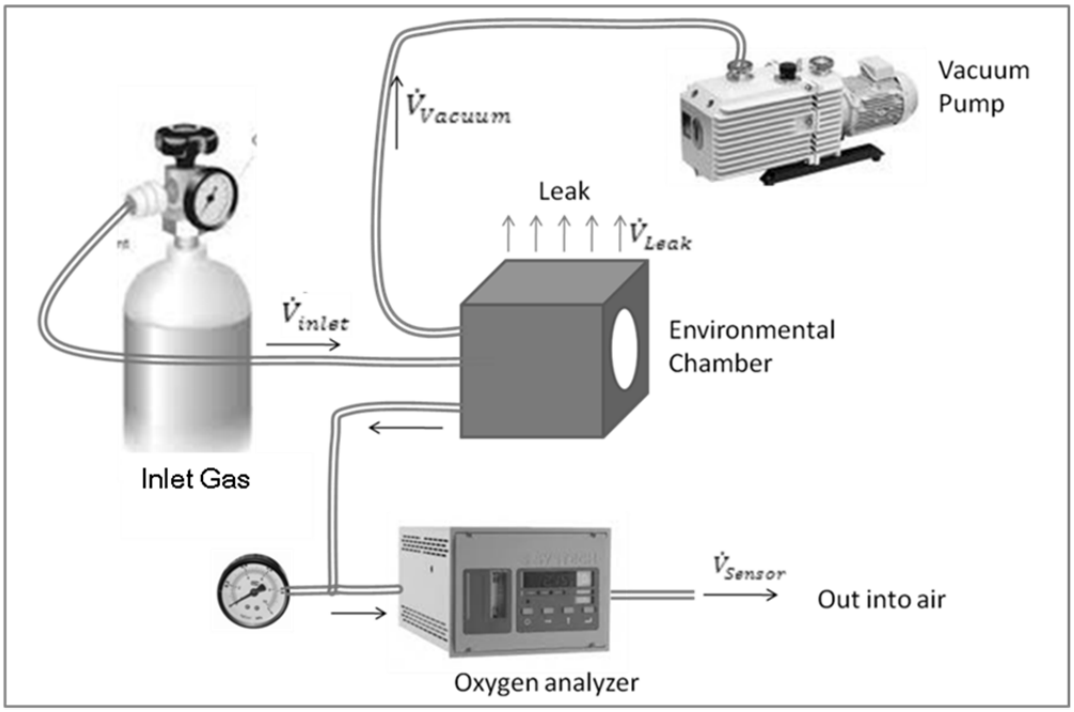

Figure 3.24: Set up -1 to purge oxygen inside the chamber

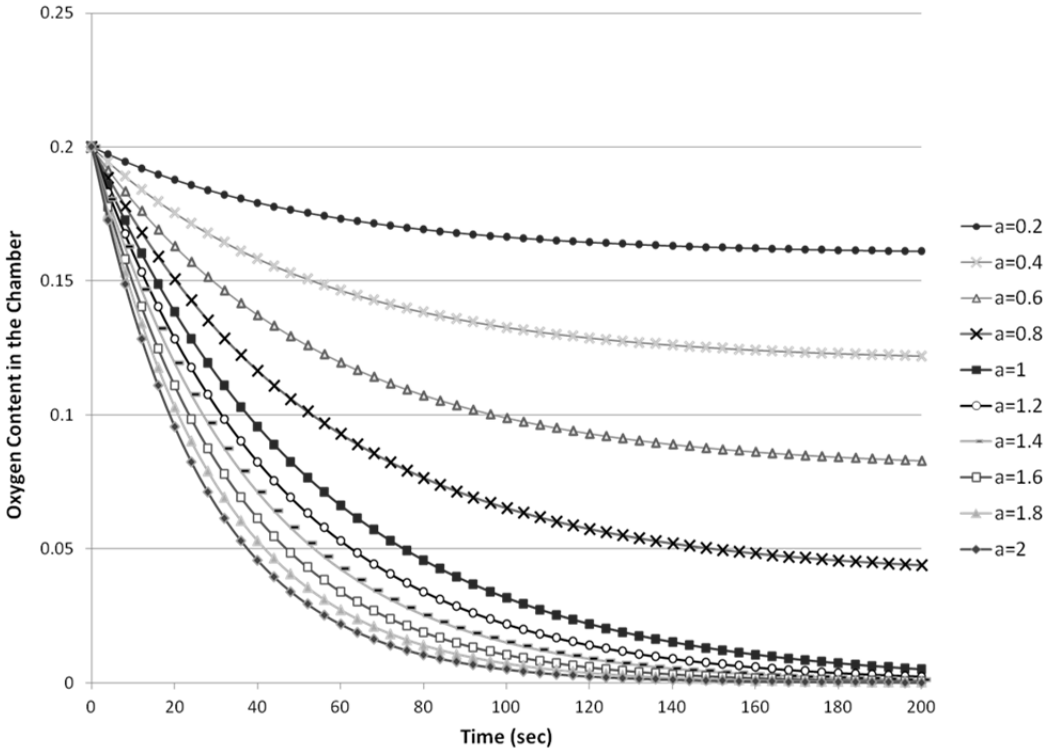

Figure 3.25: Oxygen concentration in the chamber as a function of time for various amounts of inlet gas flow rates where "a" is the ratio of gas inlet rate and vacuum pump suction rate, $a = \frac{\dot{V}_{inlet}}{\dot{V}_{Vacuum}}$.

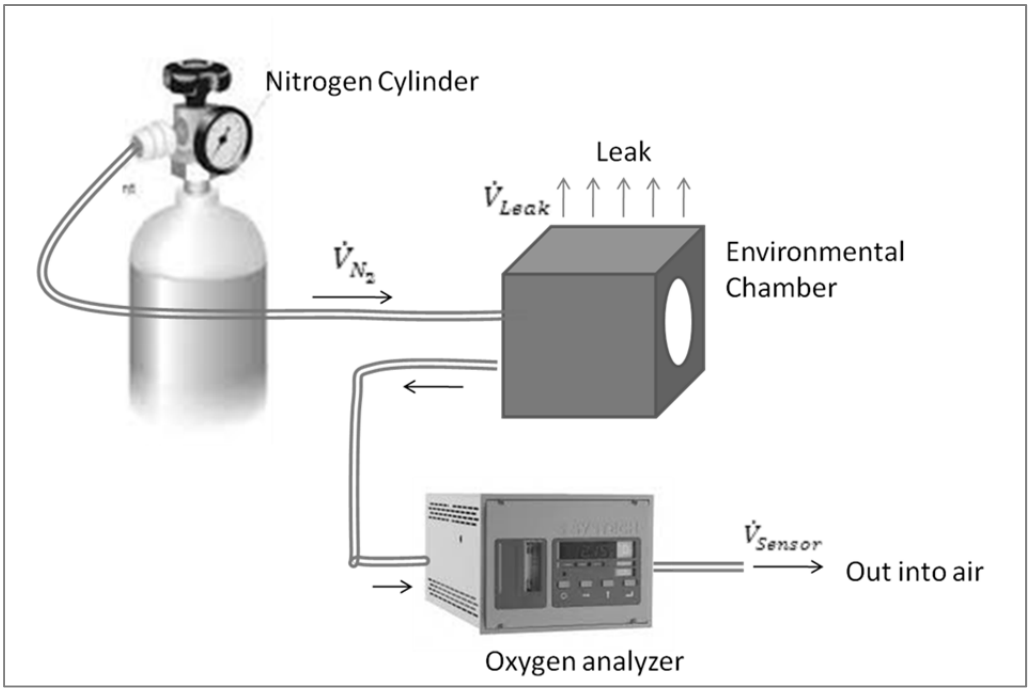

Figure 3.26: Set up -2 to purge oxygen inside the chamber

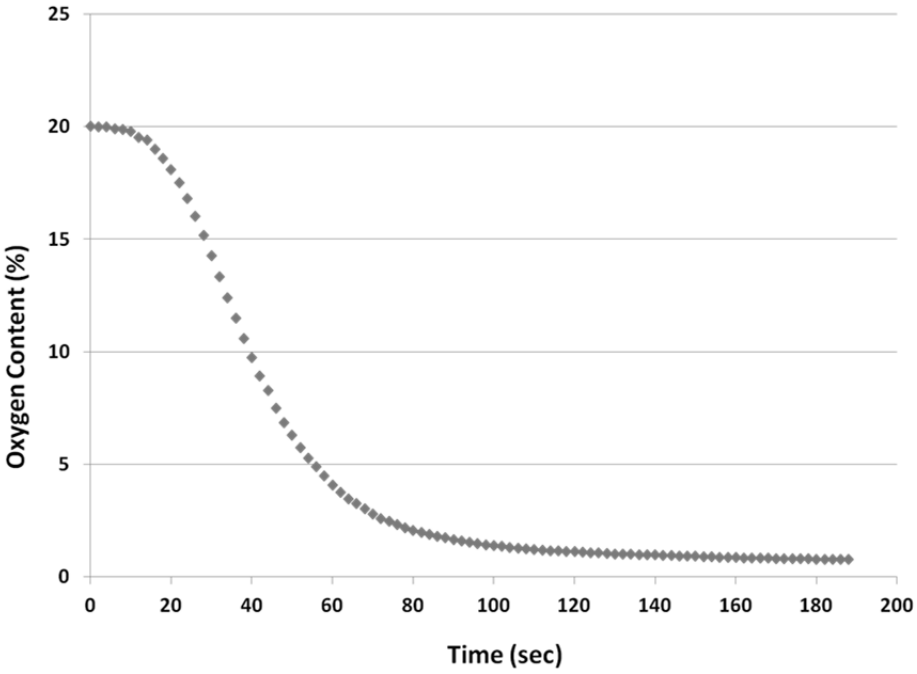

Figure 3.27: Measured oxygen concentration inside the chamber as a function of time with inlet gas flow rate = 6 SCFH.

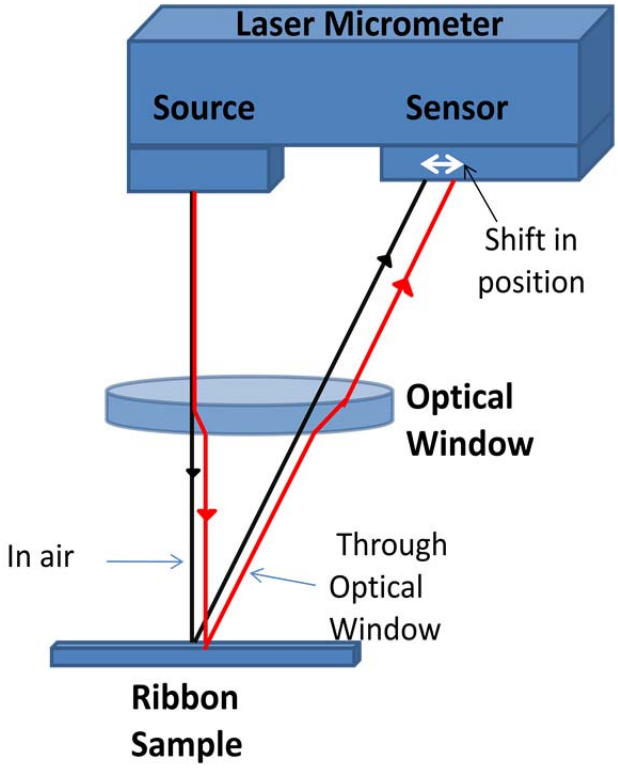

Figure 3.28: Comparison of optical paths followed by the laser light through air and through an optical window. The double diffraction at the two surfaces of the window leads to a shift in the location on the CCD sensor that the laser hits and a corresponding shift in the sample positioning is recorded.

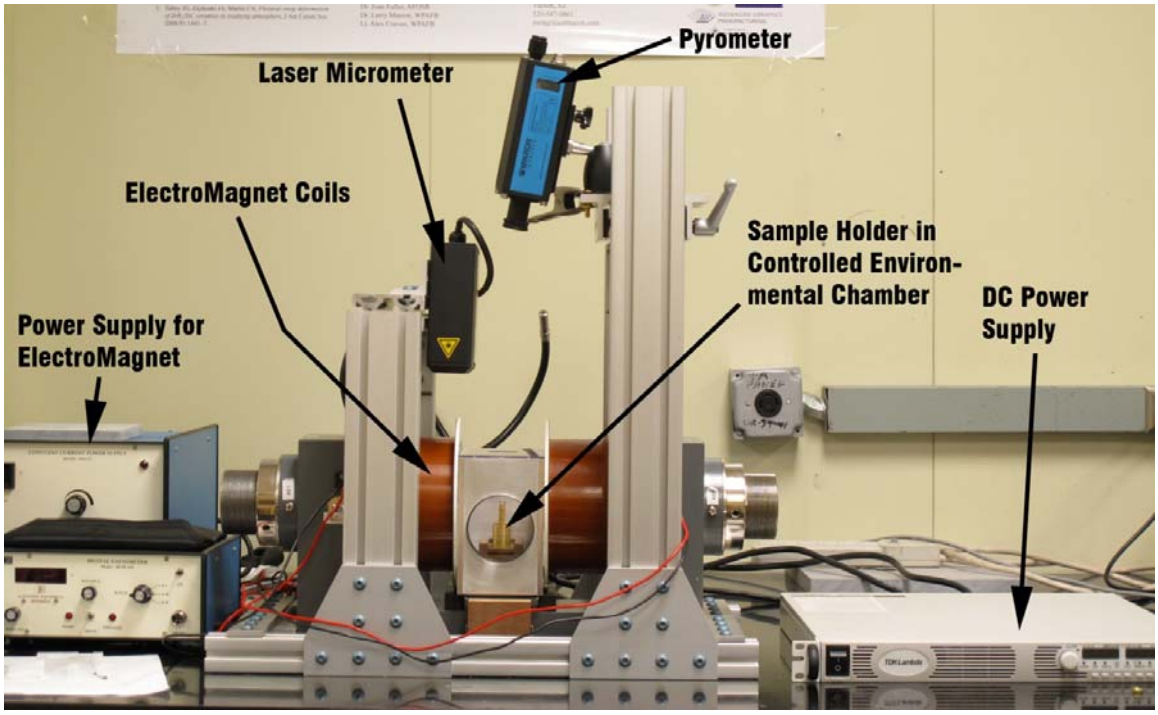

Figure 3.29: Entire beta version of the Electro Magnetic Mechanical Apparatus showing all the components.

References

1. http://www.kjmagnetics.com/proddetail.asp?prod=BY0X08%2DN52

2. S. Karlsdottir, J.W. Halloran, "Rapid Oxidation Characterization of Ultra High Temperature Ceramics" *J. Am. Ceram. Soc*., 90 [10] 3233–3238 (2007).

3. I.G. Talmy, J.A. Zaykoski, C.A. Martin, "Flexural Creep Deformation of ZrB2/SiC Ceramics in Oxidizing Atmosphere", *J. Am. Ceram. Soc*., 91 [5] 1441–1447 (2008).

4. http://svslabs.com/Products/ProductDetails1.aspx?ProductID=25&CategoryID=1

5. http://www.gisdevelopment.net/magazine/global/2007/september/images/51_1.jpg

6. http://www.me-sensor.com/glossar/_images/Laser-Triangulation.gif

7. http://archives.sensorsmag.com/articles/0702/laser/fig1.gif

8. G. B. Rybicki, A.P. Lightman, "Radiative Processes in Astrophysics", © John Wiley & Sons, New York, (1979).

9. Metrology Resource Co. www.**metrologyresource**.com

10. C. D. Irkus and D.R. Wilder, "High-Temperature Oxidation of Molybdenum Disilicide", *J. Am. Ceram. Soc*., 49, 173–177 (1966).

11. K. Yanagihara, T. Maruyama and K. Nagata, "High temperature oxidation of Mo-Si-*X* intermetallics (*X* = Al, Ti, Ta, Zr and Y)", *Intermetall*, **3** 243–251 (1995).

12. W.W. Webb, J.T. Norton, C. Wagner, "Oxidation of Tungsten", *J. Electrochem. Soc*., Volume 103 [2] 107-111 (1956).

13. P. Panjan, B. Navinsek, A.Cvelbar, A.Zalar and I.Milosev, " Oxidation of TiN, ZrN, TiZrN, CrN, TiCrN and TiN/CrN multilayer hard coatings reactively sputtered at low temperature", *Thin Solid Films* 281-282 (1996).

14. K.G. Denbigh, J.C.R. Turner, " Chemical Reactor Theory: An Introduction", Cambridge University Press, Cambridge (1965)

CHAPTER 4

ANALYSIS OF STRESS STATE IN EMMA WITH FINITE ELEMENT METHOD

4.1. Dynamically Evolving Stresses and Strains in EMMA

Conventional creep tests operate under constant load and register the resultant strain rates using structural mechanics with similar analysis as presented in Chapter 2. The moment from the load is calculated to estimate the maximum flexural stress experienced in the outer fibers, which is reported. However, the stress and strain conditions in EMMA have to be explored beyond these elastic solutions because of two important issues:

1. After the initial load is placed on the ribbon specimen, it will deform. The shape of the thin section is no longer a straight horizontal line, but a curved shape. The current passing through the cross section will follow the direction of this curved material. This has two implications:
    1A. The direction of current flow at each location will be different because of the curvature. Thus the direction of the load, I×B will also change

across the span. The load will now have a vertical component w_z as well as a horizontal component w_x.

1B. The deformation of the ribbon will now depend on this new load condition. However, at the next instant as the deformation of the ribbon changes, the load conditions will also change. Therefore the load conditions and the ribbon shape are both interdependent and dynamically evolving.

2. At high temperatures the strain is not simply elastic but also visco-plastic. Therefore the strain rate consists of the elastic component from change of stress states and a plastic component that arises even from constant stress.

4.2. Simulations using Finite Element Method (FEM)

Due to the above issues, the behavior of the samples in EMMA is more complex than conventional techniques and cannot be analytically calculated. Therefore the modeling is broken down into individual steps each concerning only one of the above issues, 1A, 1B and 2.

Issue-1A involves the change of load conditions across the ribbon span. Therefore a 1-D Finite Element Analysis is mandatory with the ribbon divided along its length into several tiny segments/elements. Issue- 1B concerns evolving loads, therefore the model has to accommodate another dimension to track these time variations. So, a 2-D Finite Element Model with one of the dimensions along the length of the ribbon and the second

dimension being time is employed. The behavior across the cross section is assumed to be uniform. The length of the beam is divided one dimensionally into "N" number of elements. If the length of the ribbon is "L", then each element is of length "dL" given by:

$$dL = \frac{L}{N}$$

Since the behavior concerned in this section is elastic, there would be no time factor involved in the physics; therefore the length of each time element is unidentifiable. So we will count time in terms of instants only. Each instant of time is noted as one element. In real time the entire simulation period will be nearly infinitesimally short.

This model will predict the response of an elastic beam under the dynamically changing load conditions of EMMA. Next we will add the visco-plastic behavior to the same FEA using Maxwell's model, to solve Issue-2. The simulation algorithm and results are presented in the following sections 4.3-4.4.

4.3. Elastic Beam under Dynamic Load

The approach to solve for the moment of each element of FEM is traditional in the sense that it utilizes a free body diagram on an entire section as in conventional structural mechanics. The model slices the beam at the element position we are interested in, say the "n"th element. Then it employs free body diagram of the entire section of beam left to that element. Such a section is depicted in Figure 4.2. Then it balances the forces and the moments in that section, to find the moment experienced by "nth" element. Once

the moment is known, the stresses and deformation of that element can be derived, as discussed in Chapter 2.

The reaction forces also keep evolving as the load conditions are changing and hence are a function of time. The load condition on the ribbon changes not only with time but also depending on location, hence they are functions of both time and element number. The forces at the cross-section of the section, F_x and F_y represent the tension and the shear forces respectively. The applied load components on the element "n" will depend on its inclination at that moment, angle Θ (n,t).

$$w_y(n,t) = IB.\cos(\Theta(n,t)) \quad ---(1)$$

$$w_x(n,t) = IB.\sin\big(\Theta(n,t)\big) \quad ---(2)$$

The reaction forces balance the vertical and horizontal load components on all the elements. Since there are two supports, the vertical and horizontal forces are given by:

$$R_y(t) = \sum_{n=1}^{N} w_y(n,t).dx(n,t) \quad ---(3)$$

$$R_x(t) = \sum_{n=1}^{N} w_x(n,t).dy(n,t) \quad ---(4)$$

where *dx* and *dy* are the distances spanned by the elements in x and y directions respectively.

The reaction moment is not as straightforward, but has to be derived from equating the summation of all moments across the beam to zero. For now, let us consider

$M_R(t)$ an unknown. Thus the bending moment at the n^{th} element is given by balancing all the moments in the above free body diagram as in equation **(5):**

$$M(n,t) - \sum_{n'=1}^{n}\left[\left(w_y(n',t).\sum_{n"=n'}^{n} dx(n",t)\right)+\left(w_y(n',t).\sum_{n"=n'}^{n} dy(n",t)\right)\right] + R_y(t)\sum_{n"=1}^{n} dx(n",t) + R_x(t)\sum_{n"=1}^{n} dy(n",t) + M_R(t) = 0 \quad ---(5)$$

$$M(n,t) = \sum_{n'=1}^{n}\left[\left(w_y(n',t).\sum_{n"=n'}^{n} dx(n",t)\right)+\left(w_x(n',t).\sum_{n"=n'}^{n} dy(n",t)\right)\right] - M_R(t) - R_y(t)\sum_{n"=1}^{n} dx(n",t) - R_x(t)\sum_{n"=1}^{n} dy(n",t)$$

And the summation of the moments across the beam must equal zero [1],

$$\sum_{n=1}^{N} M(n,t) = 0$$

$$0 = \sum_{n=1}^{N}\sum_{n'=1}^{n}\left[\left(w(n',t).\sum_{n"=n'}^{n} dx(n",t)\right)+\left(h(n',t).\sum_{n"=n'}^{n} dy(n",t)\right)\right] - N.M_R(t) - R_y(t)\sum_{n=1}^{N}\sum_{n"=1}^{n} dx(n",t) - R_x(t)\sum_{n=1}^{N}\sum_{n"=1}^{n} dy(n",t)$$

Thus we can derive the Reaction Moment to be **(6):**

$$M_R(t) = \frac{1}{N}\left\{\sum_{n=1}^{N}\sum_{n'=1}^{n}\left[\left(w(n',t).\sum_{n"=n'}^{n} dx(n",t)\right)+\left(h(n',t).\sum_{n"=n'}^{n} dy(n",t)\right)\right]\right.$$
$$\left. - R_y(t)\sum_{n=1}^{N}\sum_{n"=1}^{n} dx(n",t) - R_x(t)\sum_{n=1}^{N}\sum_{n"=1}^{n} dy(n",t)\right\} \quad ---(6)$$

Then we can plug this reaction moment into equation **(5)**

$$M(n,t) = \sum_{n'=1}^{n}\left[\left(w(n',t).\sum_{n"=n'}^{n} dx(n",t)\right)+\left(h(n',t).\sum_{n"=n'}^{n} dy(n",t)\right)\right]$$
$$- R_y(t)\sum_{n"=1}^{n} dx(n",t)$$
$$- R_x(t)\sum_{n"=1}^{n} dy(n",t)$$
$$- \frac{1}{N}\left\{\sum_{n=1}^{N}\sum_{n'=1}^{n}\left[\left(w(n',t).\sum_{n"=n'}^{n} dx(n",t)\right)+\left(h(n',t).\sum_{n"=n'}^{n} dy(n",t)\right)\right]\right.$$
$$\left. - R_y(t)\sum_{n=1}^{N}\sum_{n"=1}^{n} dx(n",t) - R_x(t)\sum_{n=1}^{N}\sum_{n"=1}^{n} dy(n",t)\right\}$$

Since, the elastic deformation curvature at any location is directly related to the bending moment at that location as: $\frac{d^2y}{d^2x} = M(x)/EI$. [1] The same applies within FEM,

$$\frac{d^2y}{d^2x}(n,t) = M(n,t)/EI \quad ---(7)$$

From Differential calculus, the curvature at any location is given by the differentiation of the slope,

$$\frac{d^2y}{d^2x}(n,t) = \frac{\frac{dy}{dx}(n,t) - \frac{dy}{dx}(n-1,t)}{dx(n,t)}$$

Therefore to obtain the slope at any point, these steps are reversed,

$$\frac{dy}{dx}(n,t) = \frac{d^2y}{d^2x}(n,t).dx(n,t) + \frac{dy}{dx}(n-1,t)$$

$$\frac{dy}{dx}(n,t) = \sum_{n'=1}^{n} \frac{d^2y}{d^2x}(n',t).dx(n',t) + \frac{dy}{dx}(1,t)$$

$$\frac{dy}{dx}(n,t) = \sum_{n'=1}^{n} M(n',t).dx(n',t) + \frac{dy}{dx}(1,t) - - - (8)$$

The boundary conditions for fixed ends dictate the slope at the ends to be zero, $\frac{dy}{dx}(1,t) = 0$. [1] With other kind of edge supports, the boundary conditions may dictate different end slopes. But by integrating the moments across the length, the slope at a given location is determined. The slope of each element gives the inclination of that element,

$$\Theta(n,t+1) = \frac{dy}{dx}(n,t)$$

This obtained inclination is taken to be the inclination at the next instant. The new inclination implies new load condition, and the entire process from Equation 2 is repeated. Similar to this computation of slope from integration of curvature, deflection can be computed by integrating the slopes:

$$y(n,t) = \sum_{n'=1}^{n} \frac{dy}{dx}(n',t).dx(n',t) + y(1,t) - - - (9)$$

The boundary conditions dictate a beam would not move with fixed supports, so $y(1,t) = 0$. And the shape of the beam at any given time point based purely on elastic deformation can be obtained.

The result of this simulation is the deflection profile of the ribbon, y (n,t). Since the ribbons are horizontal initially, deflection at this time, y (n,0) = 0. Therefore the deflection profile also reflects the actual shape of the ribbon. The shape of the ribbon at any given time can be read by a following the contour of the surface along the line representing any particular time point. Time=0 represents the flat profile at the beginning. Time=1000 is the last time point in this algorithm.

Figure 4.3 is thus a surface plot of evolution of deflection profile/ ribbon shape with time. It reflects the prompt elastic deformation of a ribbon when a current of 50 amperes heats it to 1600 °C and a magnetic field of 1 Tesla is applied across. The Lorentz load experienced by the ribbon is therefore 50 N/m. The dimensions of the ribbon were taken to be 25mm × 2mm × 0.5mm. In such a ribbon the 50N/m load causes an initial maximum flexural stress of 15.6 MPa. The elastic modulus of the material was chosen to be E = 400 GPa.

At the very next instant, the ribbon shape changes significantly to accommodate the distributed load placed on it. The deflection is the largest at the center of the ribbon,

as predicted. After this point, deflection graph looks quite steady with time i.e. the ribbon seems to obtain its final shape very fast. This signifies that the loading conditions reached a balance with ribbon geometry. And thus the loading conditions in EMMA with distributed loads are similar to conventional testing techniques with pointed loads.

The maximum deflection predicted by the model is 0.6mm which is much smaller than the length of the ribbon = 25mm. Therefore the angle subtended by the deflection is also not large with the horizontal load component much smaller than the vertical load component. So it is not surprising that the resulting deflection does not vary with time later.

4.4. Visco-Elastic Beam under Dynamic Load

Thus far, only the elastic strain/deformation has been considered. At high temperatures, due to material creep, there is another strain component, the visco-elastic strain. The behavior of such a visco-elastic material under stress can be simulated by use of two rheological elements, a spring and a dashpot. The spring represents elastic behavior and the dashpot the viscous behavior. The spring element has stiffness equal to E, the Young's modulus. The dashpot is assigned a linear coefficient of viscosity λ, also known as the coefficient of traction, which is directly related to coefficient of viscosity, η, by the relation:$\lambda = 3\eta$. In the elastic element, the stress and strain are related by Hooke's law as:

$$\sigma_e = E.\varepsilon_e \qquad ---(10)$$

In the viscous element the relation is derived from Newton's law for viscous flow,

$$\sigma_v = \lambda . \frac{d\varepsilon_v}{dt} \quad ---(11)$$

There are several rheological models with different combinations of these two elements. The simplest of these is Maxwell model [2], which combines the two elements in series. In this model, the same amount of stress acts on both the elements,

$$\sigma = \sigma_e = \sigma_v \quad ---(12)$$

The total strain is summation of the two individual strains,

$$\varepsilon = \varepsilon_e + \varepsilon_v \quad ---(13)$$

To derive the total deformation/deflection in the ribbon (Y) from the strain (ε), we will use the theory of simple bending. At any section of the ribbon, assuming that the cross-sectional plane normal to the axis of the ribbon remains planar and there is no asymmetry in the rates of tensile and compressive creep (ZrB_2-SiC has not shown evidence of asymmetric creep as discussed in the next chapter, Chapter 5 Section 5.6), the following relation still holds true:

$$\varepsilon = c . \frac{d^2Y}{dx^2} \quad ---(14)$$

where c is the distance from the neutral axis. Differentiating Equation **(13)** by time gives,

$$\dot{\varepsilon} = \dot{\varepsilon_e} + \dot{\varepsilon_v}$$

$$\dot{\varepsilon} = \frac{\dot{\sigma_e}}{E} + \frac{\sigma_v}{\lambda} = c.\frac{d^2\dot{Y}}{dx^2}$$

Since the stress on both elements is same in Maxwell model, as given in Equation **(12)**.

$$\dot{\varepsilon} = \frac{\dot{\sigma}}{E} + \frac{\sigma}{\lambda} = c.\frac{d^2\dot{Y}}{dx^2}$$

Multiplying both sides by c.dA (dA is elemental area of cross-section of the ribbon and c is the distance from the neutral axis) and integrating over the cross-section area:

$$\frac{1}{E}\int \dot{\sigma}.cdA + \frac{1}{\lambda}\int \sigma.cdA = \frac{d^2\dot{Y}}{dx^2}\int c^2 dA$$

Now the bending moment is defined as, $\int \sigma.cdA = M$ and second moment of inertia as, $\int c^2 dA = I$. [3] Therefore equation **(12)** becomes,

$$\frac{\dot{M}}{E} + \frac{M}{\lambda} = \frac{d^2\dot{Y}}{dx^2}.I \quad ---(15)$$

Writing in terms of 2-D FEM:

$$\frac{d^2\dot{Y}}{dx^2}(n,t) = \frac{M(\dot{n},t)}{EI} + \frac{1}{\lambda I}.M(n,t)$$

In this new algorithm the time factor clearly becomes more prominent and the time step "*dt*" is a parameter in the iterations. Figure 4.5 shows the deflection plot Y(n, t) or the visco-elastic ribbon profile evolution with similar load conditions as those used in

the elastic ribbon problem before. The coefficient of traction λ was taken to be: 5×10^{13} Pa-s.

At time zero the ribbon is completely flat and at the next instant, the ribbon undergoes immediate elastic deformation. This elastic deflection seems to the equal to that observed in section 4.3 for fixed ended elastic ribbon. Later, the deflection seems to increase with time. Since the model the previous section predicts the elastic deflection not to change over time, whatever the change in deflection/ribbon profile is observed after the first few moments must be purely creep.

4.5. Correlation between Maxwell and Norton-Arrhenius Models

An attempt has been made to justify the use of Maxwell's visco-elasticity model to characterize the creep behavior. Conventionally, the creep rate has been defined using the Activation energy as:

$$\dot{\varepsilon} = A.\exp\left(-\frac{Q}{RT}\right).\sigma^{n} \quad ---(16)$$

where Q is the apparent activation energy, and n is the stress exponent. The creep experiments have shown that the data fits this trend well with a Q = 350 kJ/mol and n = 1.4. If the stress exponent "n" is approximated as 1, the above creep rate equation becomes similar to Maxwell's viscous element in Equation **(11).**

$$\dot{\varepsilon} = A.\exp\left(-\frac{Q}{RT}\right).\sigma = \frac{\sigma}{\lambda}$$

The coefficient of traction, λ, is given by:

$$\lambda = \frac{\exp\left(\frac{Q}{RT}\right)}{A}$$

The normalizing constant A was also chosen from the existing creep data ~ 10^{-6} 1/Pa-s which gives the coefficient of traction $\lambda = 5 \times 10^{13}$ Pa-s at the temperature of 1600 °C where the simulation is calculated.

4.6. Summary

In EMMA, the electromagnetic forces that are used to deform the specimens are themselves subjected to change with deformation. Thereby the dynamically evolving load conditions are not easy to visualize and a simulation model is necessary to be able to interpret the empirical results. There were altogether four programs written. The first two assume only elastic behavior with two different kinds of end conditions, fixed or free. The latter two assume visco-elastic behavior which includes the plastic deformation along with the elastic component. Maxwell's model was employed because of its simplicity. Both the elastic and the visco-elastic beams with free ends showed significantly different behavior from the fixed ends indicating the key role played by the reaction moments in maintain the balance of dynamic load and ribbon shape.

The purely elastic material with fixed ends is predicted to reach its steady state profile in an infinitesimal time. That indicates that the loading conditions and the

resultant deformation reach their balance and maintain it, making the loading conditions in EMMA comparable to conventional techniques except that we utilize distributed loads instead of pointed loads.

The visco-elastic behavior seems to predict a continually increasing deflection in the ribbon, reflecting creep. Another conclusion of this is that the load conditions in EMMA are estimated not to become catastrophic. However, it is possible that Maxwell's model is too simple and more accurate predictions will need more complicated models.

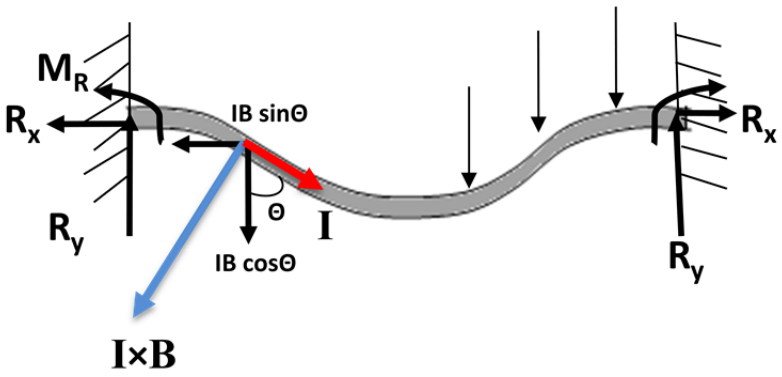

Figure 4.1: Free body diagram of the entire ribbon - Loading conditions after the first initial time frame. Note now there are both vertical and horizontal I×B components.

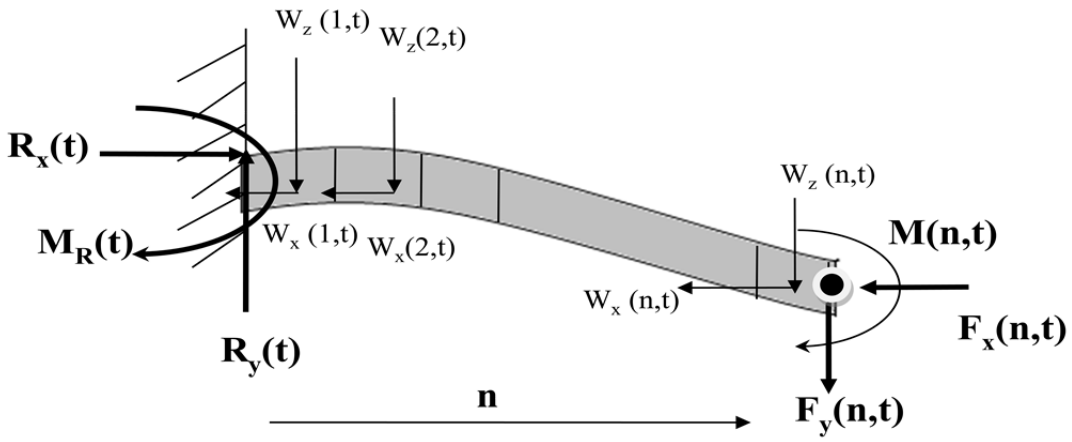

Figure 4.2: Free body diagram of the left Section of the ribbon depicting all the forces and moments.

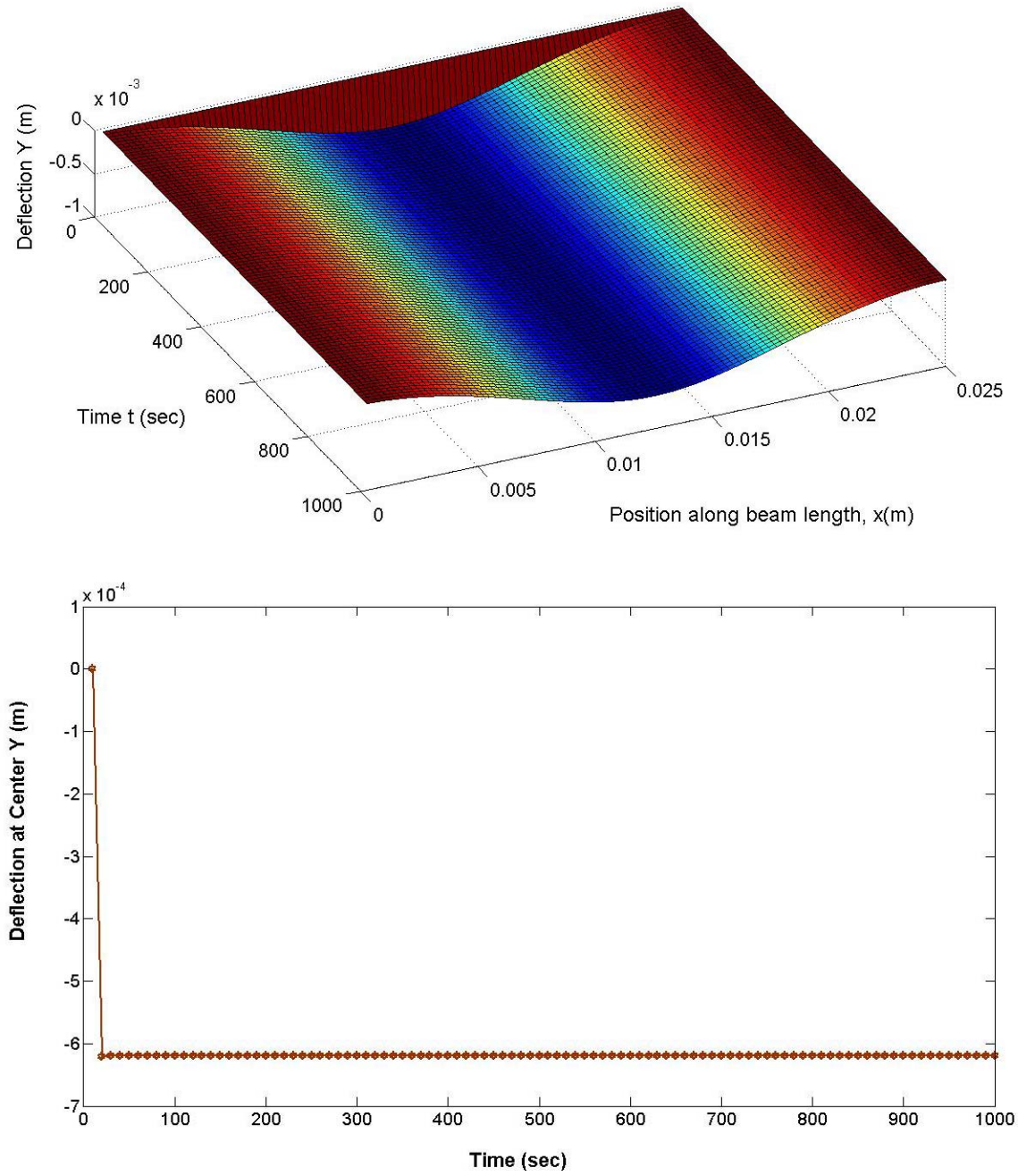

Figure 4.3: Elastic deformation of the ribbon under 50 N/m Lorentz load. Top: Deflection surface plot y(n,t), for fixed ends. It represents the evolution of ribbon profile with time – which turned out to reach a steady state instantly. Bottom: The midpoint deflection or the deflection at the center – taken from the surface plot above - as a function of time. It shows the steady state deflection to be 0.6mm.

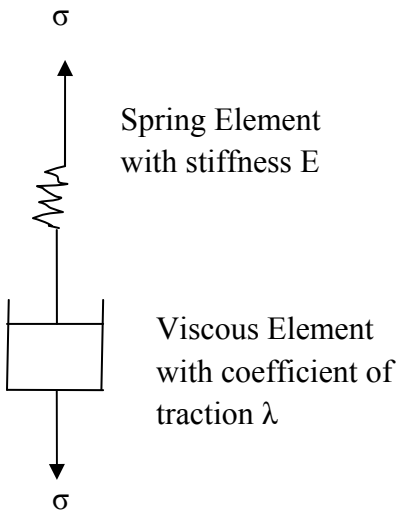

Figure 4.4: Maxwell model of visco-elastic behavior

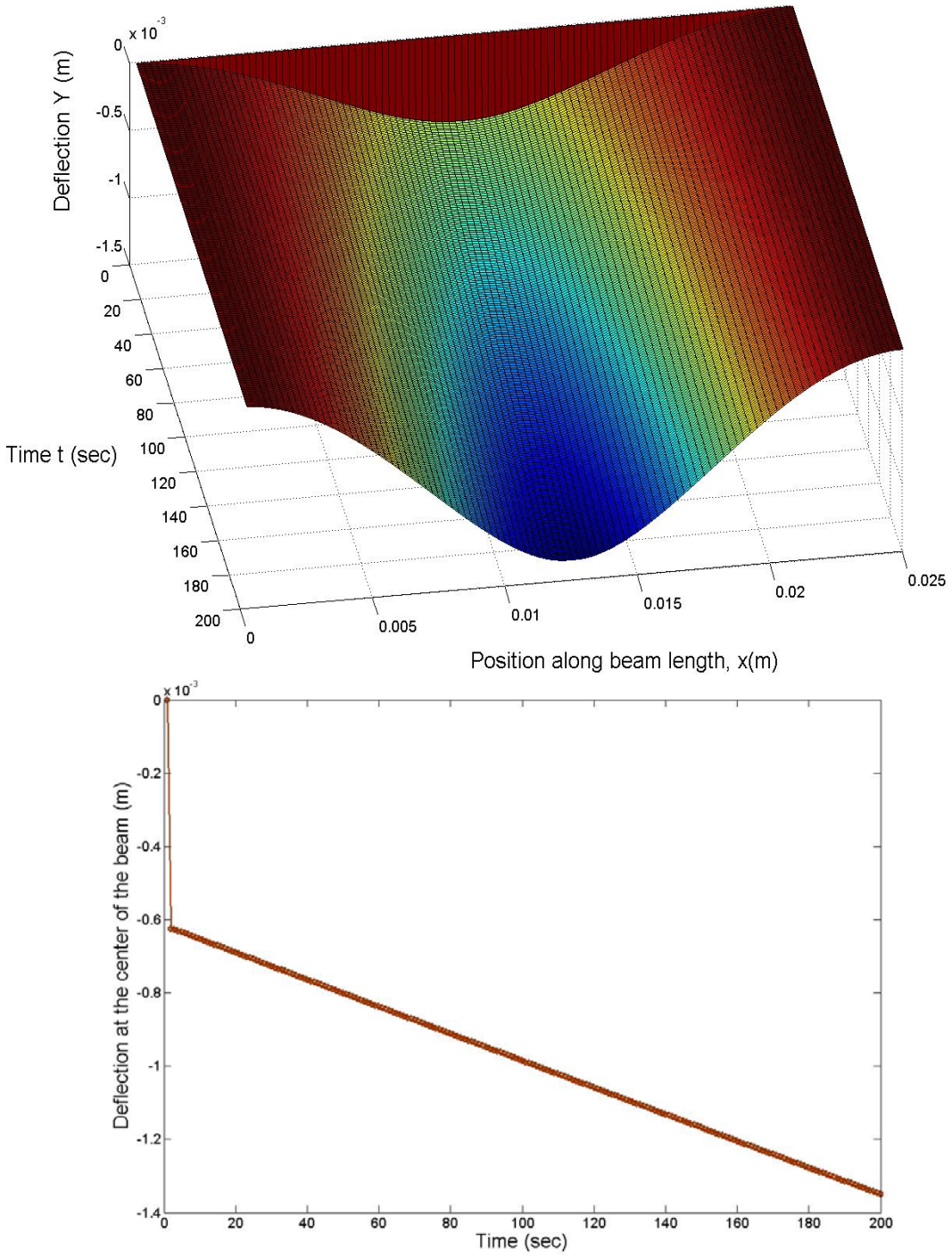

Figure 4.5: Visco-elastic deformation of the ribbon under 50 N/m Lorentz load. Top: Deflection surface plot y(n,t) representing the evolution of ribbon profile with time which predicted a time-dependent increase in the deflection besides the initial instantaneous deformation. Bottom: The midpoint deflection/deflection at center vs time shows the initial instantaneous deflection 0.6mm same as the elastic beam along with a linearly increasing time dependent deflection.

References

1. Harry West, “Analysis of Structures: An integration of classical and modern methods”, second edition, 1989, John Wiley and Sons, Inc.

2. D. Lenczner, “Deflections of Beams and Composite Subject to Creep”, *Build. Sci.* Vol. 6, pp-45-51.

3. R. C. Coates, M. G. Coutie, F. K. Kong “Structural Analysis“, 3rd Edition, © *Chapman and Hall, London*, UK (1997).

4. I.G. Talmy, J.A. Zaykoski, C.A. Martin, “Flexural Creep Deformation of ZrB2/SiC Ceramics in Oxidizing Atmosphere”, *J. Am. Ceram. Soc*., 91 [5] 1441–1447 (2008).

CHAPTER 5

CREEP TESTING USING EMMA THROUGH 2200 °C

5.1. Creep Testing Atmospheres

Ultra High Temperature Ceramics (UHTCs) are considered potential candidates for structural components such as nose cones and leading edges in future generation hypersonic and supersonic vehicles, [1] where temperatures can go higher as 2000 °C. Creep deformation is inevitable during their application [2] at high use temperatures. Transition to creep behavior [3] and nonlinearity in stress strain curves [4] have been observed at high temperatures in ZrB_2-SiC. Thus creep resistance is an important criterion for the selection of materials in addition to other properties including oxidation resistance and retained strength at use temperatures. Creep testing is done at ultra high temperatures on ZrB_2-30%SiC in 1700–2200 °C range, over a stress range 20-50 MPa. Creep experiments were performed in air as well as Nitrogen with 0.25% O_2.

Creep testing of ZrB_2-SiC in air at high temperatures is inevitably accompanied by oxidation of the material which leads to formation of complex oxide scales. [5,6,7] These oxide scales are an outer layer of Silica acting as a protective film, a columnar

layer of Zirconia and a porous ZrB_2 layer where the SiC has selectively oxidized and flowed out. As a result the direct mechanical properties of the UHTC will not be reported from these creep experiments but instead the mechanical properties of the UHTC along with the oxide layers.

Another disadvantage associated with oxidation is that the oxide scales are electrically nonconducting. So at high temperatures, > 2000 °C, the time duration of a test has to be much shorter to avoid variation in the current required to resistively heat the thin (350 μm thickness) ribbon specimens. If the tests are longer than a few minutes duration, the current value will decrease since the current conducting portion thickness is reduced, as given by equation 2 in Chapter 2. If the test duration is too long, the ribbon can be oxidized through their thickness and then the current flow is stopped bringing the resistive heating to a halt. Therefore EMMA tests are ceased after only a short duration at very high temperatures.

Other consequences of oxidation includes a decrease in the thickness of the load-bearing unreacted material since the oxide scales are composed of large amounts of liquid silica and cannot endure significant stresses. [8,9] Therefore the oxide scales really do not contribute in stress bearing under the creep test load. So even while the applied load in EMMA is constant, the true stresses in the unoxidized ZrB_2-SiC substrate are higher. In the thin ribbon specimen, oxidation causes a significant reduction in the thickness of the remaining substrate. These higher stresses may lead to higher creep rates in air. To be able to report purely the mechanical response of the UHTC, oxidation has to be

suppressed. Suppression was accomplished by performing the tests inside the environmental chamber (described in Chap. 3, section 3.3.6.) in an atmosphere containing mainly nitrogen and a trace amount of oxygen < 0.25%.

While this data will be of interest for the designers who require the mechanical properties of the UHTC for modeling, creep testing in air is also important because it is closer to replication of the actual application environment for these materials such as reentry where presence of oxygen and associated oxidation are inevitable. Therefore creep experiments were performed in air as well as in Nitrogen with small amount of O_2 and the creep rates from these two oxidizing and nonoxidizing environments were compared.

5.2. Material and Specimen Preparation

(a) Material:

Our specimens are made of ZrB_2- 30vol% SiC composite prepared by Advanced Ceramic Manufacturing (ACM) Inc., Tucson, AZ. [10] Raw materials were obtained from commercial sources: ZrB_2 (HC Stark Grade B) had a particle size 1.5-3 μm and SiC (H.C. Stark Grade UF10) had a particle size of 0.7 μm. Powders were ball milled in Isopropyl alcohol for 24 hours using WC milling media. Powders were dried in a convection oven and sieved prior to firing. Samples were fired in a resistively heated, uniaxial, graphite hot press at 2100 °C in vacuum of ~11 Pa in a heating rate of 5°C/min, a pressure of 28 MPa, and a soak time of 30 minutes.

(b) Specimen Geometry:

The sample dimensions were chosen to ensure a relatively large portion of the thin section will have uniform temperature, as discussed in Chapter 2 section 2.2. The samples were made in ribbon geometry with ribbon dimensions: 37.5 mm × 2 mm × 0.35 mm and the thick ends of length 6mm each. The test bars were abrasively machined to size, while maintaining the neutral axis of bar perpendicular to the compaction axis during hot pressing. Samples were rough machined using a 100 grit diamond wheel and finished to size using a 380 grit diamond wheel. The ribbon geometry is shown in Figure 1. During resistive heating, the thin section of this sample reaches ultra high temperatures while the thicker ends supporting it remain below 200 °C. The central 25mm of the hot zone/thin section has uniform temperature ± 25°C with sharp gradients towards the end. (The temperature gradients are addressed in detail in Chap. 2, section 2.2.) So this unique geometry of our specimens makes them self supported.

(c) Material Properties:

The microstructure processed material was studied under the electron microscope and grain size measurements were taken. There was no porosity observed. The average grain size of ZrB_2 was 2.52 ± 0.45 μm and SiC grain size was 1.61 ± 0.28 μm. The room temperature flexural strength of this material was measured using four point flexure following ACM ASTM C1161 test procedure in an Instron Materials Testing Load Frame (Model 3369) to be 664 ± 18 MPa. This was comparable to the flexural strength of similar composites prepared and tested by Sciti et al at CNR-ISTEC and Fahrenholtz et al

at UMR. [11,12] Electrical resistivity is also another critical property since EMMA employed resistive heating and the four point resistivity of this material was measured to be 2.66×10^{-7} Ω-m.

5.3. Experimental Conditions – Directly Controlled and Creep Relevant Variables

All the creep tests in flexure are performed using the second generation Electro Magnetic Mechanical Apparatus described in Chapter 3 section 3.2. Unlike the conventional techniques such as three point or four point flexures, EMMA applies flexure with uniform load. A current of 45 – 65 Amps was required to heat these UHTC samples to temperatures 1600 – 2200 °C. Since the current requirement varies with temperature (to be able to apply similar loads at different temperatures), the magnetic field is adjusted accordingly. Further, to apply different loads at a given temperature the magnetic field again is altered. The applied magnetic flux density was 0.2 – 0.5 Tesla and was maintained uniformly across the entire length of the ribbon.

The directly controllable variables are current and magnetic flux through which temperature and stress are indirectly controlled. The temperature is measured using the pyrometer, while the stress is calculated as discussed in Chapter 2.

$$\sigma_{\max} = \chi \frac{L^2}{Yt^2}\left(I_x B_y\right)$$

where χ is a fraction 0.25-0.75 depending on the type of end supports. The result of the creep experiments is the permanent deformation δ_{max} of the specimen which is measured using the laser micrometer from which the strain is derived.

$$\varepsilon = \gamma \frac{\delta_{max} t}{L^2}$$

where γ is a number 4.8 or 6.5 or 8 depending on whether the supports are fixed-fixed or fixed-pinned or pinned-pinned type. Table 5.1 summarizes all the test conditions of creep experiments in the ambient and the low oxygen atmospheres.

5.4. Creep Deflection Profile and Strain Rates

The geometry of the thin section of the ribbon with its length relatively much longer than its thickness ensures that the deflection in these specimens at even small strains will be easily perceptible. The strains in the post creep specimens were calculated to be in the range of 0.15-0.87%. But due to the geometry, the deformations were significant and usually of the order of 1mm. Figure 5.1 shows a post creep specimen tested at 2150 °C and 20 MPa stress in nonoxidizing atmosphere with a deflection of 1.25mm corresponding to a strain of 0.28%. The deformation was in fixed-fixed end type and hence has a deformation profile where the slope of deflection goes to zero at the ends. It may be noticed that even such a low strain induces appreciable deformation in the long thin ribbons.

The deflection profile is the locus of the deformed ribbon shape, i.e. the deflection from the horizontal/initial position at a given location along the length of the ribbon. Deflection profiles were measured for all the post creep samples and the strain is derived from the maximum deflection (δ_{max}) and the profile shape, as discussed in Chapter 2,

section 2.3. There were two major types of error possibilities in deriving δ_{max} from the deflection profile data.

a. The silver plates that support the thick ends of the ribbon specimen are not always on the same level. Often they are on levels that are vertically separated by a fraction of an mm. Although neither obvious for the visible eye nor significant to vary the electromagnetic load, this vertical separation induces considerable variation in the maximum deformation, which is itself of order of a millimeter in several creep tests. Such an error is demonstrated in Figure 5.2 by comparison of the raw and the corrected data of a deformed ribbon.
b. The second error can arise from including the contribution made by the thick ends to δ_{max} when the ribbon deforms in pinned – pinned ended manner (Chapter 2, section 2.3). Figure 5.3 shows image of a deformed ribbon (free-free ends) illustrating this error

These two errors were corrected in all the deformation profiles. Figure 5.4 plots the evolution of the corrected deformation profile of a sample undergoing creep at 1650 °C under 45 MPa stress. Measurements were taken using the laser micrometer after specific time durations to understand the evolution of the ribbon shape as a function of time. This sample behaved as a pinned – pinned ended beam and so the stress and strain were calculated by the formulae derived in 2.3.2 and 2.4.2 sections of Chapter 2. The maximum deformation, the deflection at the center was plotted as a function of time. The corresponding strains calculated as given in 2.4.2, were also plotted as a function of time

to derive the average creep rate. Figure 5.5 plots the deformation and strains in the same sample whose deformation profile is presented in Figure 5.4.

Notice that the measured δ_{max} increases linearly with time which is taken as evidence of steady state creep. The calculated strain rate from Figure 5.5 (b) is $1.7 \pm 0.1 \times 10^{-5}$ /sec with the uncertainty based on the largest and smallest slopes consistent with this data.

5.5. Creep Data in Ambient and Reduced Oxygen Atmospheres

Using the procedure described in the previous sections, the creep data over a range of temperatures starting from 1600 °C to as high as 2200 °C was collected at different levels of applied stress – 20, 30 and 50 MPa. For each stress level, experiments at 5 or 6 temperatures were conducted from 1700 – 2200 °C. For each temperature and stress condition, 2 specimens were tested. Figure 5.6 presents the creep strain rates in air of ZrB_2-30% SiC. The data is in Arrhenius representation with the logarithm of strain rate plotted as a function of inverse of temperature, to derive the activation energy from the slope. The general creep rate equation, $\dot{\varepsilon}$, is given by Norton-Arrhenius Equation:

$$\dot{\varepsilon} = A\sigma^n . e^{\left(\frac{-Q}{RT}\right)} \qquad -------(1)$$

where Q is the apparent activation energy for the dominant creep mechanism (J/mol), T is the temperature (K) , R is the universal gas constant (J/mol-K), σ is the applied stress (Pa), n is the stress exponent and A is the normalizing constant.

So the logarithm of this creep rate as a function of 1/T is expected to be a linear plot with slope – *Q/R* × *loge*.

$$\boldsymbol{log\dot{\varepsilon}} = \log(A) + n.\log(\sigma) - \boldsymbol{loge}.\frac{\boldsymbol{Q}}{\boldsymbol{RT}} \qquad -------(2)$$

The data fitted well with least squares regression lines and their coefficient of determination $R^2 > 0.99$. The corresponding residual sum of squares (RSS) values were used to estimate the standard deviation for the apparent activation energy derived from the slopes of these lines. The apparent activation energy was 321 ± 25 kJ/mol for 50 MPa, 313 ± 33 kJ/mol for 30 MPa and 322 ± 30 kJ/mol at 20 MPa, with the range of uncertainty calculated from the RSS. These values are statistically indistinguishable, so we can average them to estimate the apparent activation energy as 319 ± 30 kJ/mol.

The results were repeatable as observable from the small error bars which show the range of observed creep rates in the 2 independent experiments. The largest range was for 2200 °C/20 MPa experiment which ranged about 11%. The other experiments had smaller error bars in some cases no larger than the symbols.

The stress dependence of isothermal creep is presented in Figure 5.7 as plot of logarithm of strain rate as a function of logarithm of stress at different temperatures. The slopes of these graphs correspond to the stress exponent, n. Figure 5.7 shows that this plot of log ε vs. log σ is rather linear at all the temperatures with the stress exponent (n) being 1.37 at 1700 °C, 1.31 at 1800 °C, 1.38 at 1900 °C, 1.32 at 2000 °C and 1.61 at 2100 °C. Their average of n is 1.40 ± 0.20. Creep experiments by previous researchers showed a

value of n = 1 in ZrB_2 with 0-25% SiC. [13] The observed stress exponent from our creep experiments 1.4 ± 0.2 is close to this literature value. This suggests that lattice creep by dislocation motion, which usually has large stress exponents listed in Table 1.1, is not the dominant mechanism. It is more likely a grain-boundary or intergranular creep mechanism.

$$\boldsymbol{log\dot{\varepsilon}} = \log(A) + \boldsymbol{n}.\boldsymbol{\log(\sigma)} - log_{10}e.\frac{Q}{RT} \qquad ---------- (3)$$

While creep testing in ambient air ZrB_2-SiC oxidation occurs and to understand the mechanical response of the pure UHTC without the effects of oxidation, creep experiments were performed in reduced oxygen atmosphere. The oxygen content in this atmosphere was < 0.25%. In this environment, the oxidation of ZrB_2-SiC was suppressed. The test conditions were maintained similar to the experiments in air for the sake of comparison. The creep strain rates in this starved oxygen air are presented in Figure 5.8 in the temperature range of 1600 -2000 °C at two stress levels 30 and 50 MPa.

These also fit the linear Arrhenius plots well, with coefficient of determination R^2 > 0.99 and the slopes of the lines corresponded to activation energies of 343 ± 24 kJ/mol at 30 MPa and 344 ± 35 kJ/mol at 50 MPa. This apparent activation energy was higher than that the value obtained for creep in air, which was 344 ± 35 kJ/mol, which corresponds slightly lower strain rates in the absence of oxidation, as can be seen from comparison of creep rates in the two atmospheres at 50MPa stress presented in Figure 5.9.

Since creep in air involves oxidation and oxidation reduces the thickness of the load bearing portion resulting in higher stresses, as discussed in section 5.1 earlier in this chapter, the air creep rates need to be compensated for the increase in stress. This is done by measuring the oxide scale thickness and correcting the nominal stress, $\sigma_{nominal}$ with this geometric factor in thickness to find the true stress, σ_{true}.

$$\sigma_{true} = \sigma_{no\,min\,al} \frac{t^2}{(t - 2t_{oxide})^2} \quad \ldots\ldots\ldots\ldots (4)$$

where t is the thickness of the original ribbon and t_{oxide} is the thickness of oxide scale on each surface of the ribbon. Then the stress exponent "n" is used obtain the corrected creep rates, $\dot{\varepsilon}_{true}$ at the nominal stress value from the measured creep rates.

$$\dot{\varepsilon}_{corrected} = \dot{\varepsilon} \left(\frac{\sigma_{no\,min\,al}}{\sigma_{true}} \right)^n \ldots\ldots\ldots\ldots (5)$$

In the Figure 5.9 above these "corrected" creep rates in air are presented along with the measured creep rates in air and N_2 + 0.25% O_2 and it can be noticed that these values were found to closely match the creep rates in nonoxidizing atmosphere. Since the difference between the creep rates in air vs. 0.25% oxygen can be related to geometry, it likely that creep is not directly affected by atmosphere. A better estimate for the activation energy for creep would be the non-oxidizing value of 344 ± 35 kJ/mol.

5.6. Validation of Flexural Creep in ZrB_2-SiC

Weiderhorn et al showed that materials with glassy boundaries have much slower creep in compression, often a Norton power law, but much faster creep in tension. The

tensile creep is accompanied by cavitation and does not have a power law of stress dependence. If force-fit to a power law it has a non-physically large stress exponent. Examples of such materials are ordinary Alumina with silicate grain boundary phase and ordinary liquid phase Si_3N_4. [15-17]

When the load is flexural and the outer side experiences tensile stresses and the inner side experiences compressive stresses. In such asymmetric creep materials, since the creep laws are different on the tensile and compressive sides, the neutral axis shifts and the stress state becomes complicated. Often in these cases, force-fits to Norton laws result in poor fits are large apparent stress exponents.

EMMA is also a flexural testing technique and it is important to know if ZrB_2-SiC has symmetric creep (with same creep law in tension and compression where flexural creep is strictly valid) or asymmetric creep (with faster tensile creep).

One of the strong evidences suggesting ZrB_2-SiC has symmetric creep is that the observed stress exponent is close to 1, from the results presented in the previous subsection. The data points are also well fitting with the trend lines. This will not be possible if the material was creeping asymmetrically.

Another supporting evidence is the microstructure of the creep tested materials which did not show noticeable cavitation or macroscopic amounts of grain boundary glassy phases as shown in the Chapter 6. The UHTC research group at Imperial College

London have studied the TEM of the sintered 10%SiC composite and have also observed clean grain boundaries. [18] So the ZrB_2-SiC and ZrB_2- ZrB_2 do not seem to have the viscous phases that Si_3N_4 and such materials which is the root cause for the faster tensile creep and the resultant creep asymmetry.

5.7 Comparison with Conventional Data

Validation of the creep data collected using the Electro Magnetic Mechanical Apparatus and validation of the technique itself requires comparison of our data with conventionally acquired creep data of similar material with similar processing conditions. Talmy et al [13] at Naval Surface Warfare Center Carderock Division (NSWCCD) had earlier studied the creep behavior of ZrB_2-SiC composites through 4 point flexure in air as a function of temperature, stress and SiC composition. The drawback of this study was that it was limited to a rather narrow temperature range of 1300 -1500 °C which was also much lower than the expected application temperature. Nevertheless, our creep data was found to be highly linear with 1/T over a large temperature range 1600 °C – 2200 °C. The small stress exponent n = 1.4 indicates the creep mechanism might be diffusional. Talmy et al. also suggest a diffusional creep mechanism to be dominant in the temperature range they were testing. Thus it is reasonable to extrapolate the trend lines of our data to lower temperatures for comparison purpose.

Recently, K.W. White et al [19] at University of Houston also started working on creep of ZrB2-SiC using 4 point flexure in air as well as oxidation protected atmosphere

with Ar. Their temperature range was 1400-1800 °C which was certainly broader than NSWCCD. Finally the UHTC research group [20] at Harbin Institute of Technology in China found that their 30% SiC in 3-point flexure had a flow stress of 36 MPa at 1800 °C while deforming at a constant strain rate of 4.86×10^{-5} /s. While these researchers have achieved creep data at higher temperatures than Talmy's their highest temperature is still lower than application temperatures which are expected to be > 2000 °C. The comparison of creep data from EMMA with the conventional data from other researchers is presented in Arrhenius representation in Figure 5.10.

The comparison above shows that the high temperature data from Houston and the data point from Harbin group fall in the EMMA testing range. The data point from Harbin and the 1700 °C and 1800 °C data points from Houston almost overlap with EMMA data. The NSWCCD data by Talmy et al with different compositions of SiC all had similar creep rates in their temperature range of testing. The extrapolation of EMMA's 50 MPa stress line to lower temperatures shows that their data has very similar activation energy due to the similar slopes. But NSWCCD data was slower by half-an-order of magnitude.

On the other hand, the 2 Houston data points at lower temperatures was much slower than our predicted trend line and in fact slower even than NSWCCD data. These two data points suggest creep rates of ~ 2×10^{-9} /sec at 1400 °C and 10^{-8} /sec at 1500 °C. Their activation energy was much larger than EMMA and NSWCCD. While there are many possible reasons for why these small discrepancies, including the differences in

processing of the material, SiC composition, grain boundary phases etc., altogether the creep data from EMMA is comparable to conventionally acquired data.

5.8 Summary

Creep will be a dominant phenomenon in UHTCs at temperatures close to 2000 °C as we find through our creep experiments in this temperature range with large strain rates ~10^{-5}. Creep tests were performed both in air as well as reduced oxygen atmosphere with only <0.25% O_2 to compare the effect of oxidation.

The directly controllable test conditions in EMMA are current and magnetic flux density. These can be maneuvered to achieve creep tests over a wide range of temperatures, 1700 – 2200 °C under different stress conditions 20-50 MPa. This is the highest temperature of testing in the literature. Significant deformations were observed in the long thin ribbon specimens even at relatively low strains 0.1-1%. The deformation profile of the ribbons were tracked at the maximum deformation is monitored as a function of time to derive the creep rates.

The creep from EMMA fit well with the Norton-Arrhenius law, with strain rates ~10^{-6} at low temperatures to 10^{-4} at high temperatures. The activation energy of our 30% SiC composite was found to be 319 kJ/mol in air and 344 kJ/mol in Nitrogen. The higher activation energy in Nitrogen indicates creep rates will be faster in air. Creep testing in air caused oxidation of the UHTC and formation of oxide scales which did not support

the mechanical load. This caused higher true stresses in the remaining UHTC and hence faster creep. The corrected creep rates in air (for the higher true stresses from oxidation) and the creep rates in Nitrogen were found to be very closely matching. The other kinetic creep parameter, stress exponent was found to be 1.4.

Validation of this creep data and EMMA as a technique was done through comparison of EMMA creep data with conventional data. This comparison showed that the few data points other researchers had in our testing temperature range were similar and extrapolation of EMMA trend line to lower temperatures is also akin, thereby establishing EMMA as a functional technique for high temperature creep of UHTCs.

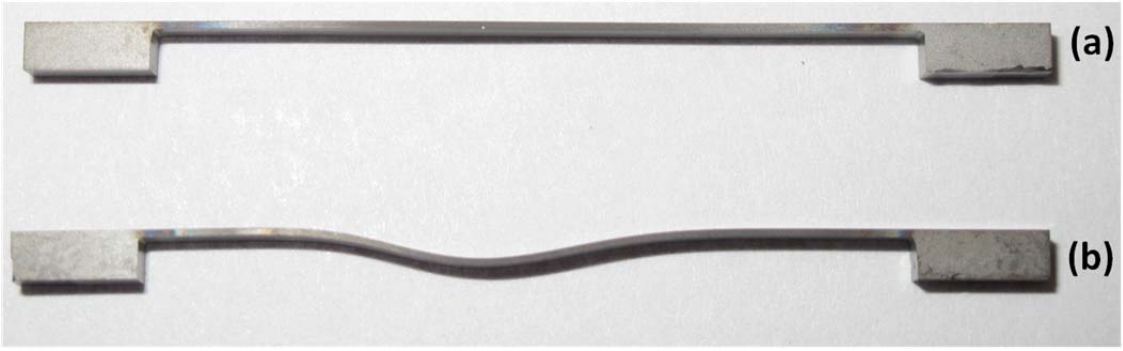

Fig 5.1: (a) Ribbon specimen before creep (b) Specimen after 8 seconds creep with 50 Amps and 0.36T corresponding to a temperature of 2150 °C and 20 MPa stress in nonoxidizing atmosphere. The deflection was 1.25mm corresponding to a strain of 0.28%.

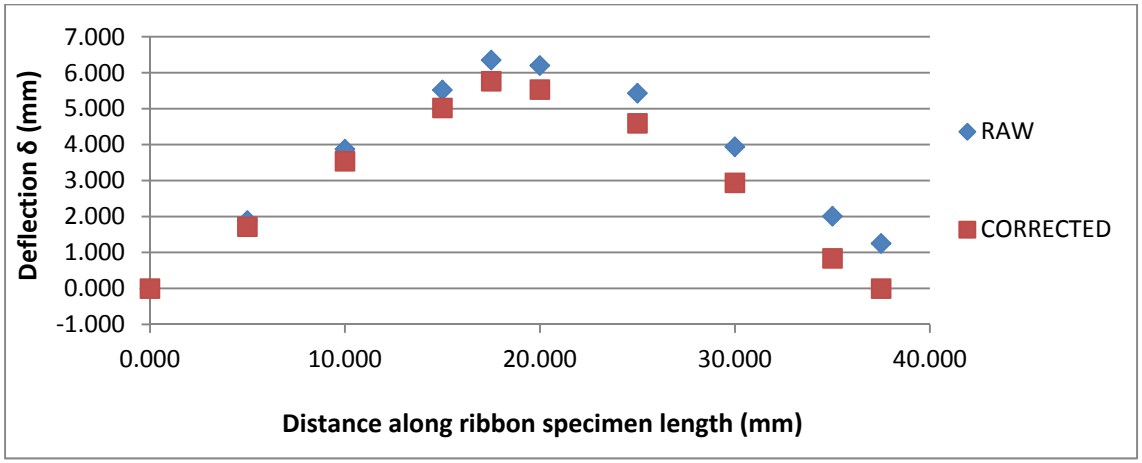

Figure 5.2: Raw and corrected profiles of post creep specimen tested at 2100 °C under 50MPa with pinned-pinned ends.

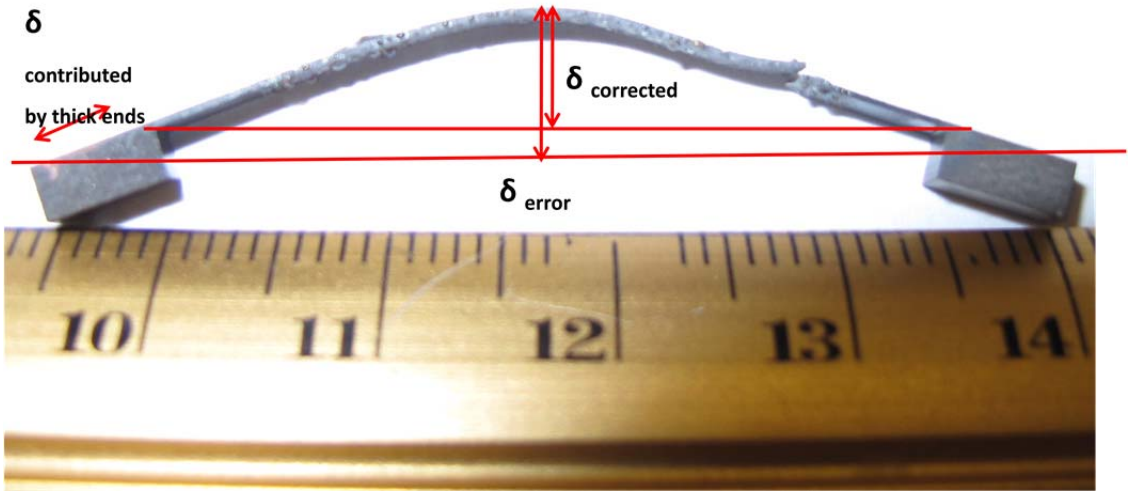

Figure 5.3: Image of deformed ribbon (free-free ends) illustrating the error caused by including the contribution from thick ends to the deflection calculation

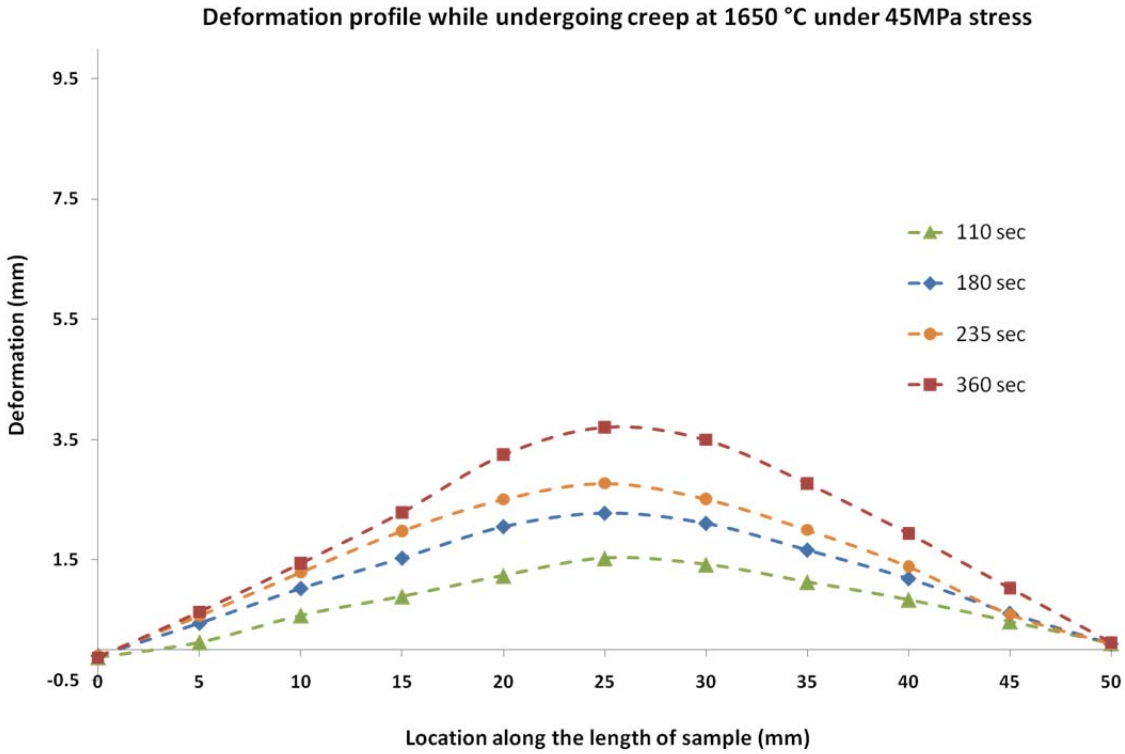

Figure 5.4: Deformation profile – deflection as a function of distance along sample length- of a sample while undergoing creep at 1650 °C under 45 MPa stress. Measurements were taken using the laser micrometer after specific time durations to understand the evolution of the ribbon shape as a function of time.

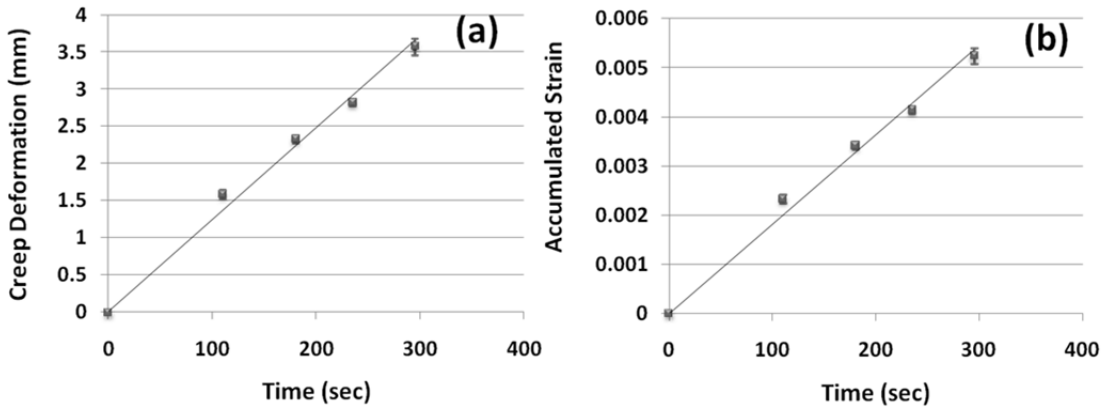

Figure 5.5: (a) Creep deformation, center deflection δ_{max} as a function of time in a specimen creep tested at 1600 °C under 45 MPa stress. (b) Corresponding plastic strain in the same specimen as a function of time – the slope of the graph was taken to be the creep strain rate of $1.73 \pm 0.1 \times 10^{-5}$ /sec.

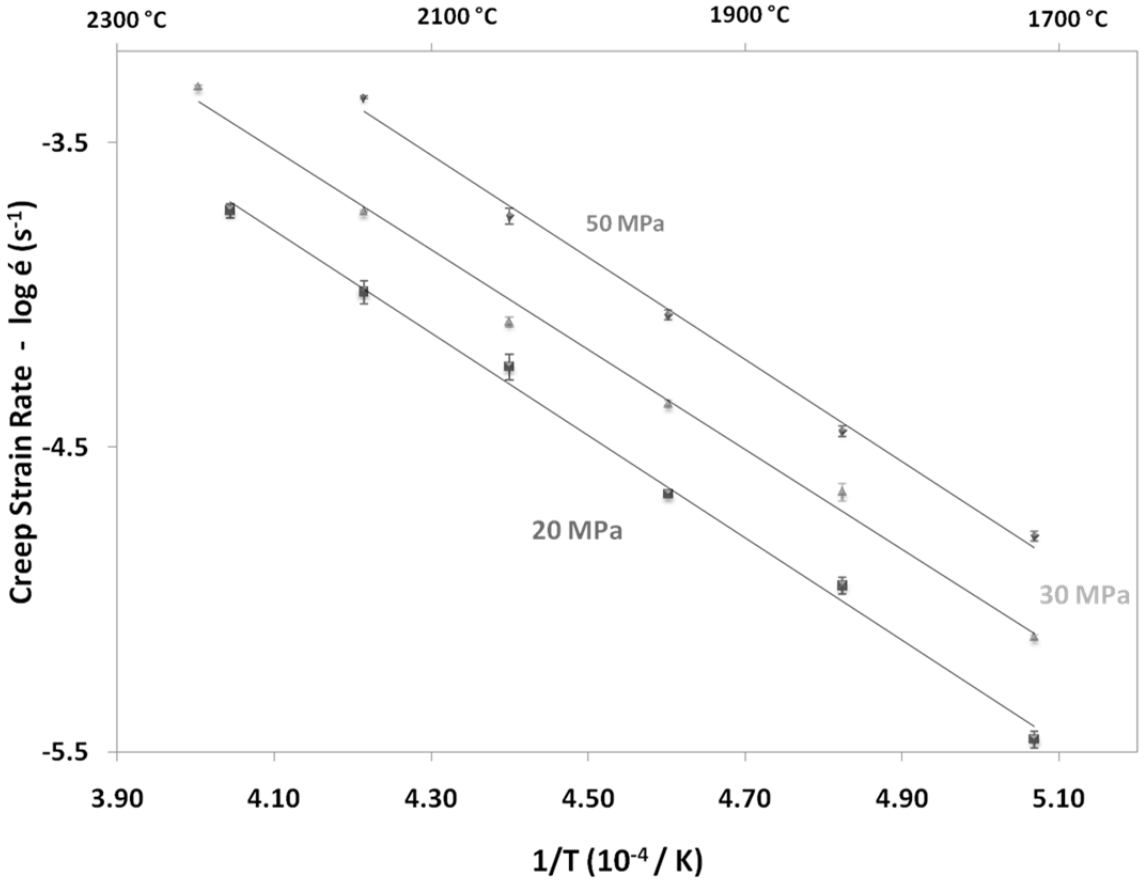

Figure 5.6: Creep strain rates of ZrB_2-30% SiC in air at 1700 – 2200 °C under 20-50 MPa

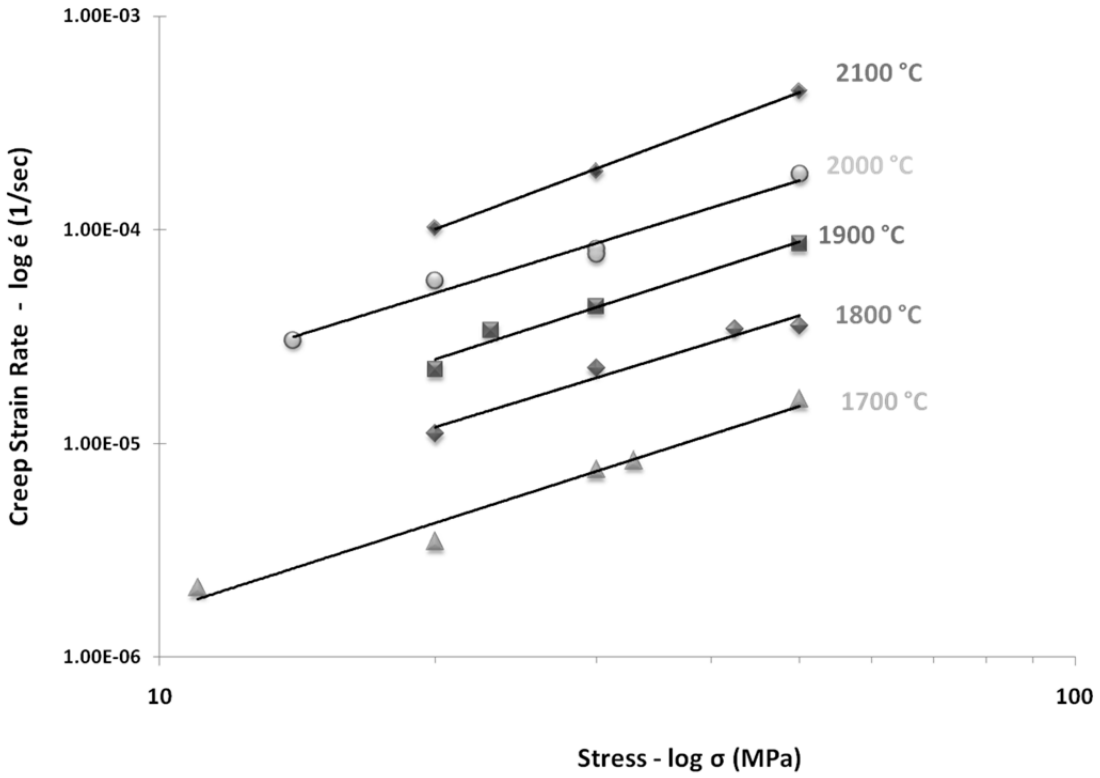

Figure 5.7: Logarithm of creep strain rates of ZrB_2-30% SiC in air at 1700 – 2200 °C as a function of logarithm of stress

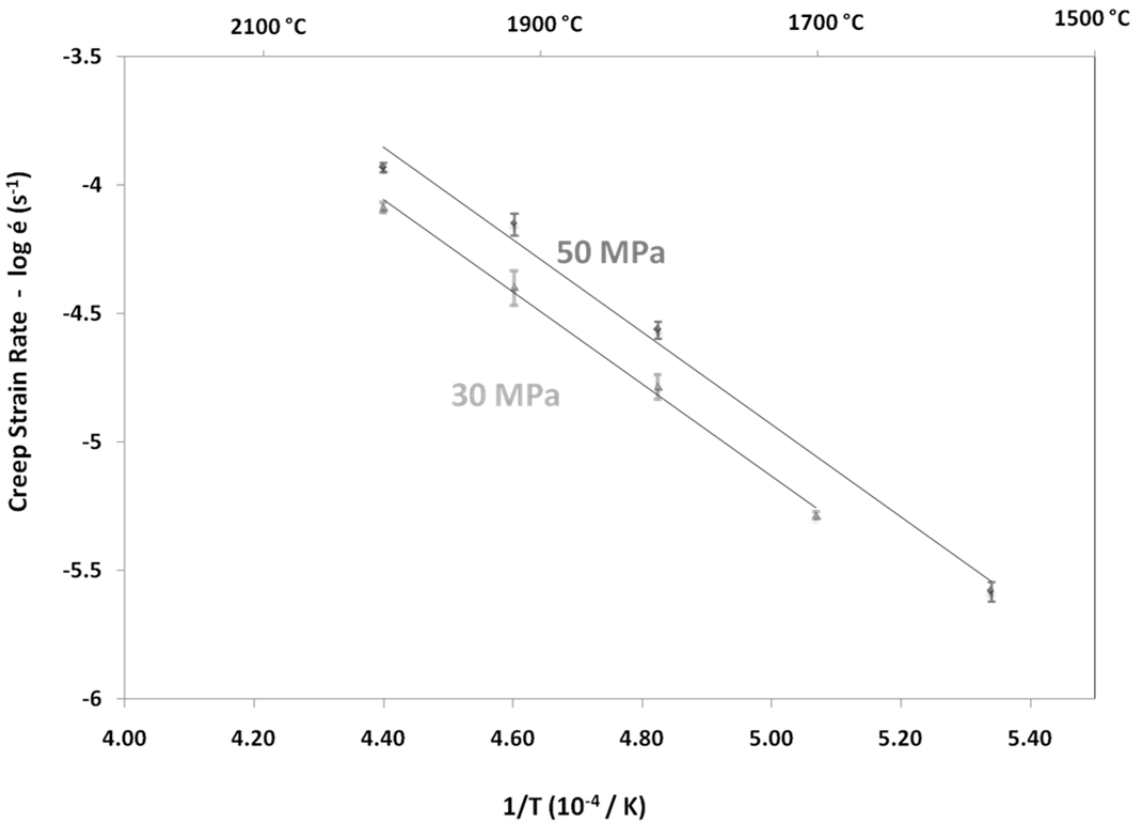

Figure 5.8: Creep strain rates of ZrB_2-30% SiC in oxidation suppressed atmosphere of N_2- 0.25% O_2 at 1600 – 2000 °C under 30 -50 MPa stress

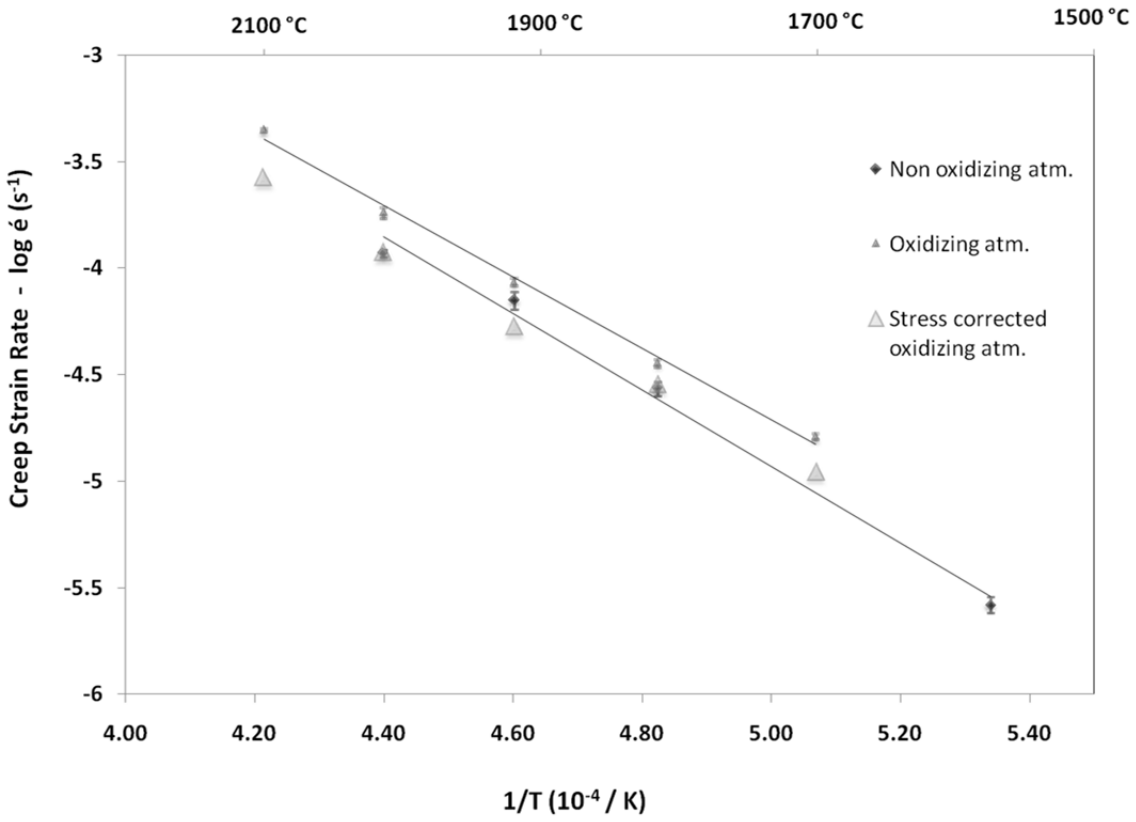

Figure 5.9: Comparison of creep strain rates of ZrB_2-30% SiC in oxidizing and non oxidizing atmospheres at 50 MPa stress. The creep rates in air corrected to compensate the higher true stresses are also marked.

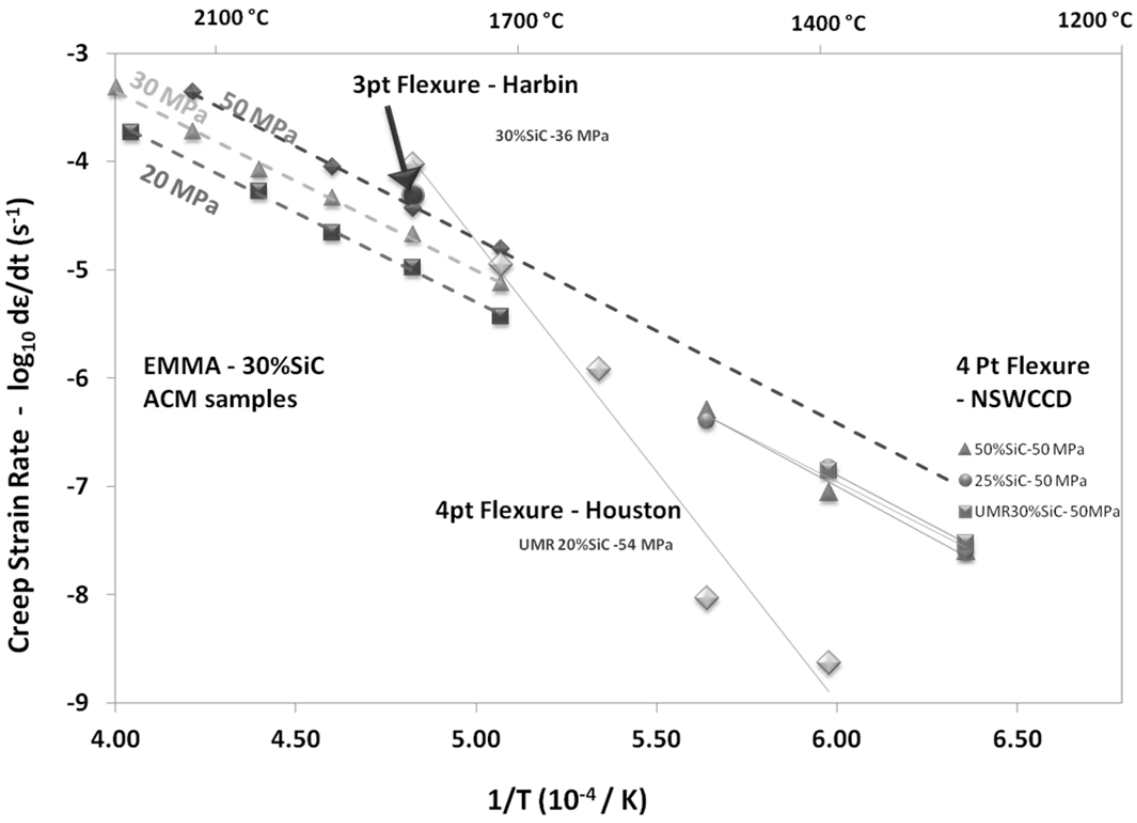

Figure 5.10: Comparison of EMMA creep data with conventional data acquired through 3-point and 4-point flexure

Table 5.1: Summary of the test conditions for creep experiments in EMMA. The directly controlled parameters such as current (I), magnetic flux (B) and time, the derived parameters stress and strain and the measured parameters temperature and deformation are all presented.

Test No	L (mm)	W (mm)	t (mm)	I (A)	B (T)	Time (s)	δ (mm)	T (°C)	Stress (MPa)	ε (%)
	Geometry			(Directly controlled)			Micro-meter	Pyro-meter	Elastic beam theory	
OXIDIZING ATMOSPHERE										
59	37.5	2.6	0.45	75	0.42	25	1.215	1900	50.4	0.205
61	30	2	0.37	43	0.45	80	0.673	1800	29.4	0.18
64	30	2	0.37	43	0.5	120	0.416	1800	19.84	0.135
71	37.5	2	0.42	50	0.45	33	0.804	2000	20.76	0.19
73	30	2	0.37	40	0.45	300	0.386	1700	21.2	0.105
74	30	2	0.35	43	0.45	49	1.537	2000	28.8	0.4
75	37.5	2.5	0.5	62	0.45	60	1.268	1800	49.1	0.215
80	37.5	2.5	0.5	55.5	0.46	275	2.75	1700	50.25	0.445
81	37.5	2.5	0.5	56.5	0.3	260	1.176	1700	29.7	0.195
88	37.5	2.5	0.5	59	0.22	70	0.825	1900	19.3	0.15
90	37.5	2.5	0.5	60	0.22	50	1.512	1900	30.65	0.22
91	37.5	2.5	0.5	62	0.36	60	2.355	2000	29.1	0.46
92	37.5	2.5	0.5	64	0.36	20	5.834	2100	50.0	0.89
93	37.5	2.5	0.5	64	0.36	18	4.361	2225	30.0	0.865
94	37.5	2.5	0.52	70	0.36	27	2.438	2100	30.0	0.505
95	37.5	2.5	0.52	77	0.28	23	1.859	2200	20.0	0.435
67	30	2	0.35	44.5	0.52	30	1.180	2100	20.0	0.305
72	37.5	2	0.42	45	0.45	300	1.254	1700	33.0	0.250
76	37.5	2.5	0.47	60	0.36	65	1.412	1800	42.5	0.220
82	37.5	2.5	0.52	58	0.20	180	0.225	1700	11.0	0.380
38	37.5	2.5	0.45	56.5	0.38	35	3.875	2000	50.0	0.580
68	37.5	2	0.40	45	0.45	53	0.857	1800	23.0	0.190
NON OXIDIZING ATMOSPHERE										
96	37.5	2.5	0.5	56	0.47	66	1.189	1800	51.73	0.18
101	37.5	2.5	0.5	61	0.36	90	4.173	1900	49.97	0.635
102	37.5	2.5	0.5	60.5	0.36	75	1.573	1900	31.08	0.305
105	37.5	2.5	0.5	62.5	0.36	75	6.015	2000	50.46	0.87
106	37.5	2.5	0.5	63.5	0.22	80	4.294	2000	28.95	0.66
108	37.5	2.5	0.5	53	0.	240	0.419	1600	48.95	0.065
111	37.5	2.5	0.5	57	0.39	150	0.37	1700	30.16	0.075
113	37.5	2.5	0.5	54	0.39	98	0.633	1800	28.78	0.165

References

1. M.M. Opeka, I.G. Talmy, and J.A. Zaykoski, "Oxidation-Based Materials Selection for 2000 °C + Hypersonic Aerosurface: Theoretical Considerations and Historical Experience", *J. of Mater. Sci.,* 39 [19] 5887-5904 (2004)

2. S. M. Wiederhorn, ''Particulate Ceramic Composites: Their High-Temperature Creep Behavior,'' *Key Eng Mater*, 267–87 (2000).
3. P. Hu, Z. Wang, "Flexural strength and fracture behavior of ZrB_2–SiC ultra-high temperature ceramic composites at 1800 °C", *J. Eur. Ceram. Soc.* [30] 1021-1026 (2010).

4. O.N. Grigoriev, B.A. Galanov, V.A. Kotenko, S.G. Ivanov, A.V. Koroteev and N.P. Brodnikovsky, "Mechanical Properties of ZrB_2-SiC ($ZrSi_2$) Ceramics", *J. Eur. Ceram. Soc.* [30] 2173-2181 (2010).

5. S. N. Karlsdottir, J.W. Halloran, F. Montervede, A. Bellosi "Oxidation of ZrB_2-SiC: Comparison of Furnace Heated Specimens and Self-Heated Ribbon Specimens" *Mechanical Properties and Performance of Engineering Ceramics and Composites III* (eds E. Lara-Curzio, J. Salem and D. Zhu), John Wiley & Sons, Inc., Hoboken, NJ, USA. (2008)

6. W. G. Fahrenholtz, "Thermodynamic Analysis of ZrB_2–SiC Oxidation: Formation of a SiC-Depleted Region", *J. Am. Ceram. Soc*, 90: 143–148. (2007).
7. W. L. Vaughn, H.G. Maahs, "Active –to- Passive Transition in the Oxidation of Silicon Carbide and Silicon Nitride", *J. Am. Ceram. Soc.*, 73 [6] 1540-1543 (1990).

8. I.G. Talmy, J.A. Zaykoski, M. M. Opeka, S. Dallek, "Oxidation of ZrB_2 ceramics modified with SiC and Group IV-VI transition metal diborides" Proceedings of the International Symposium on "High Temperature Corrosion and Materials Chemistry III" edited by M. McNallan and E. Opila, *The Electrochemical Society*, 12, p.144 (2001).

9. W.C. Tripp, H.H. Davis, and H.C. Graham, "Effect of SiC addition on Oxidation of ZrB2", *Am. Ceram. Soc. Bull*., 52 [8] 612-616 (1973).

10. S. Gangireddy, J.W. Halloran and Z.N. Wing, "Non-contact mechanical property measurements at ultrahigh temperatures", *J. Eu. Ceram. Soc.*, 30 [11] 2183-2189 (2010).

11. D. Sciti, M. Brach, A. Bellosi, “Long-term oxidation behavior and mechanical strength degradation of a pressurelessly sintered ZrB_2-$MoSi_2$ ceramic”, *Scripta Materialia* 53 1297-1302 (2005).

12. A. L. Chamberlain, W.G. Fahrenholtz and G. E. Hilmas “High Strength Zirconium Diboride – Based Ceramics”, *J. Am. Ceram. Soc.*, 87 [6] 1170-1172 (2004).

13. I.G. Talmy, J.A. Zaykoski, C.A. Martin, “Flexural Creep Deformation of ZrB2/SiC Ceramics in Oxidizing Atmosphere”, *J. Am. Ceram. Soc*., 91 [5] 1441–1447 (2008).

14. J.J. Melendez-Martinex, A. Dominguez-Rodriguez, F. Montervede, C. Melandri and G. de Portu “Characterization and high temperature mechanical properties of zirconium diboride based materials” *J. Eur. Ceram. Soc*., 22 [4] 2543-2549 (2002).

15. F. Lofaj, S. M. Wiederhorn “Creep processes in Silicon Nitride ceramics”, *J. Ceram. Pro. Res.*, 10 [3] 269-277 (2009).

16. S. M. Wiederhorn, B. J. Hockey and J. D. French “Mechanism of Deformation of Silicon Nitride and Silicon Carbide at High Temperatures”, *J. Eur. Ceram. Soc*., 19 [13-14] 2273 - 2284 (1999).

17. K. M. Fox and J .R. Hellmann “Microstructure and Creep Behavior of Silicon Nitride and SiAlONs” *Int. J. Appl. Technol.,* 5 [2] 138-154 (2008).

18. D. D. Jayaseelan, Y. Wang, G. E. Hilmas, W. Fahrenholtz, P. Brown and W. E. Lee “TEM investigation of hot pressed -10 vol% SiC-ZrB2 composite”, Adv. Appl. Cer., 110 [1] 1-7 (2011).

19. R.P. Aune, M.W. Bird, A.F. Thomas, P.F. Becher, K.W. White, “High Temperature Creep of ZrB2-SiC through 1800 °C”, *J. Am. Ceram. Soc*., (in progress).

20. P. Hu, Z.Wang, “Flexural strength and fracture behavior of ZrB2-SiC ultra high temperature ceramic composites at 1800 °C” *J. Eur. Ceram. Soc*.,30 [4] 1021–1026 (2009).

CHAPTER 6

MICROSTRUTURAL ANALYSIS OF POST CREEP MATERIAL

6.1. Motivation for Microstructural Investigation

There are several motives for investigating the microstructure of the material after creep experiments. The post creep specimens hold evidence of damage induced by mechanical loading during the test. The damage may be in the form of fissures or cracks in the interior of the material or grain elongation along the direction of the stress etc and can result in deterioration of the properties of the material. This is of interest for applications such as reusable thermal protection systems where the same component is expected to perform in more than one service. Even if the original material has the mechanical strength/resistance to sustain the initial use, if the material properties deteriorate during that service and the component might not be able to sustain later uses.

So while the microstructure of the post creep specimens is of interest for the mechanically induced damage, there are other motivational factors:

a. Wiederhorn et al found asymmetry in tensile creep and compressive creep rates which leads to shift in the neutral axis of the specimen under flexure. [1-3] Formation of cavitations at the grain boundaries in tension in SiN, Siliconized SiC and SiAlON materials caused the creep rates in tension to be much faster than in compression. Whether the ZrB_2-SiC will also suffer from this problem can be investigated through microstructural analysis.

b. Creep in air at high temperatures involves oxidation of the surface of the specimens. Researchers working on the oxidation resistance of the ZrB_2-SiC composite have discovered complex oxide scales including a silica liquid layer which induces a certain degree of oxidation resistance. [4,5] But the oxidation resistance of the material might deteriorate during the test due to the mechanical stresses involved. The load can cause cracks/fissures in the material exposing the material underneath the oxide scales to ambient oxygen.

c. EMMA testing is uniform loading in flexure, so there exist differntial stresses across the thickness of the sample, with the stresses being tensile on one surface and compressive on the other surface. The effect of the nature of the stresses, tensile or compressive, and the amount of the stress on the oxidation resistance can be explored. [6]

d. The creep experiments performed in the environmental chamber under reduced oxygen atmosphere can result in a different kind of oxidation. The lower partial pressure of oxygen can lead to active oxidation of silicon carbide forming silicon monoxide gas. [7] During oxidation in air, it is the passive oxidation of SiC forming silica that acts as a protective film over the surface preventing excessive oxidation. In the absence of the silica oxide scale, the oxidation resistance will be lower. On the other hand, the partial pressure of the oxygen could be too low for the oxidation of ZrB_2. So the result of these two countering effects of lower oxygen partial pressure can be studied.

6.2. Sample Preparation

The surface of the post creep specimens is covered in oxide scales which are formed during the testing. To access the internal microstructure, the ribbon sample was sectioned to obtain two types of cross sections – one across the length (axial) and one cut along the length (transverse). Both sections are made near the middle of the ribbon where the stresses are highest. Figure 6.1 illustrates the two cross sections in a schematic. Both cross sections can be used to compare the compressive and tensile side of the sample and to seek evidence of damage from mechanical loading in the interior sample beneath the oxide scales.

The axial cross section shows microstructure along the two dimensions, thickness (t) and width (W), both of which experience no stresses in ideal flexure. The transverse cross section on the other hand shows microstructure along the length direction (L) which experiences maximum stress at the middle of the ribbon. Therefore this cross section can be utilized to explore the damage induced by the stresses in the form of grain elongation. If the mechanical loading during the testing at high temperature caused grain softening and eventual grain elongation, it can be quantified using the ratio of the length of the grains along the length dimension and the grain length along thickness dimension near the tensile surface.

These cross sections are cold mounted in low temperature (80 °C) curing epoxy and polished down to 0.25 μm using traditional procedure. From each of these two types of cross sections obtained from a given sample, three areas of 25μm × 25μm size were selected from tensile, center and compressive sides of the ribbon specimen for measurement of ZrB_2 and SiC grain lengths. Figure 6.2 is a schematic of the transverse sectioning of ribbon specimen and the grain size measurement procedure. These cross sections were studied using FEI Quanta 200 3D Scanning Electron Microscope.

6.3. Post Creep Specimens' Microstructure - Air

The specimens tested in air had the typical oxide scales [8-10] such as shown in Figure 6.3. This is a post creep specimen exposed 300 seconds in air at 1800 °C under 38 MPa stress. There is an outer silica glass layer 10 μm thick, a primary ZrO_2 layer 27 μm

thick and porous ZrB_2 layer of 33 μm thickness which is SiC depleted. The ZrO_2 and ZrB_2 have similar contrast and appear in brighter shade in the secondary electron image. The SiC and SiO_2 with lower atomic weight appears in darker contrast. The void spaces in the porous ZrB_2 appear in a much darker contrast.

In these post creep specimens tested in air, cracks were observed in the oxide scales between the ZrO_2-Silica glass scale and porous ZrB_2 in the SiC-depleted layer, as shown in Figure 6.4. The cracks are not associated with the mechanical loading in creep, since they are present even in the specimens simply resistively heated with no magnetic field. In the latter samples only oxidation occurred without any mechanical load. Figure 6.5 shows the cross section of the sample with similar crack located precisely between ZrO_2-Silica glass scale and porous ZrB_2 in the SiC-depleted layer.

The cracks are not associated with thermal shocks from the exceeding fast heating and cooling rates from the ribbon method, since they also are seen resistively heated with slow ramp rates (30 °C/s). A plausible explanation for occurrence of cracks between the zirconia oxide scale and the ZrB_2 substrate is the phase transformation of Zirconia from tetragonal, the stable phase at the temperatures of creep test, to monoclinic crystal structure during cool down. [11] Evidence in Figure 6.5 supports this possibility since the cracks developed into a delamination where the delaminated portion is longer than the substrate, indicating expansion in the oxide scale.

The crystalline phase of ZrO_2 in the oxide layer was confirmed to be monoclinic Zirconia through X-ray diffraction (Rigaku Rotating Anode X-Ray Diffractometer). X-ray diffraction analysis of the surface of the ribbon specimens tested at lower temperatures in air had diffraction peaks corresponding to Monoclinic ZrO_2 (such as $(\bar{1}\,1\,1)$ at $2\theta = 28.2°$, $(1\,1\,1)$ at $2\theta = 31.5°$ etc. [12]) and an amorphous peak in 15-35° corresponding to Silica. [13] The large volume expansion associated with the tetragonal-monoclinic transformation during cooling is therefore concluded to be the cause for the cracks between the oxide scale and for the Zirconia oxide layer to detach/delaminate from the rest of the substrate.

6.4. Post Creep Microstructure – Reduced Oxygen Atmospheres

The samples tested in reduced oxygen atmosphere in the environmental chamber showed a surface layer very unlike the traditional oxide scales seen in the samples tested in air. It did not have any silica or the porous ZrB_2 layer. It showed a uniform dense microstructure of similar contrast as the ZrB_2 in the UHTC. It had a thickness of <5 μm much smaller than the 50-100 μm thick oxide scales seen in air. This crystalline phase had a grain size comparable to the original material and was identified using X-Ray Diffraction analysis of the surface of the ribbon specimen as ZrB_2. Figure 6.7. The pattern had diffraction peaks corresponding to ZrB_2 such as (101) at $2\theta = 41.6$ °, (100) at $2\theta = 32.6$ ° etc. [14] But compared to the specimen thickness this is only about 1.5% and would not affect creep behavior. Figure 6.8 shows a specimen tested in the 0.25% oxygen atmosphere at 2000°C under 50 MPa for 75 seconds, which had only a 5 μm thin scale of

ZrB_2 on its surface. This zirconium diboride surface scale could be a result of depletion of SiC from active oxidation of SiC [7] on the surface.

$$SiC\ (s) + O_2(g) \uparrow \quad \rightarrow \quad SiO\ (g) \uparrow + CO\ (g) \uparrow \qquad ----(1)$$

6.5. Post Creep Microstructure – Damage Evidence

In both the creep tests in air as well as in reduced oxygen atmosphere, the microstructure of the unreacted ZrB_2-SiC seemed unaffected. No evidence of internal damage such as cracks or fissures were observed indicating the material is resilient to creep strains up to 1%. Figure 6.9 is a secondary electron image of a region close to the tensile surface of the ribbon in the cross section cut along length. The specimen was creep tested at 2000 °C under 50 MPa stress in nonoxidizing atmosphere with a final strain of 0.86%, which is one of the largest total strains for our specimens.

In pure flexure where there is no strain in width/thickness, differential strains in the length direction are at maximum at the surface. Therefore the effect of flexural strain on the microstructure would be most noticeable at the tensile surface. However, there was no damage observed such as cracks or fissures or obvious grain elongation.

The absence of noticeable cavitation or macroscopic amounts of glassy phases at the grain boundaries indicates that the hot pressed ZrB_2-SiC behaves differently than the cavitation-prone Si_3N_4, siliconized SiC and SiAlONs studied by Wiederhorn et al. [1-3]

The ZrB_2-SiC will therefore be free from the issues of creep asymmetry that arises from cavitation and glassy phases. In fact the same researchers Wiederhorn et al have observed that non-cavitation tensile creep in Lu-doped Silicon Nitride showed similar creep rates on both sides of flexure. [15]

Although there was no change in the grain shape perceptible to the naked eye, creep could have elongated the grains in the tensile direction. To quantify the grain elongation, linear intercept measurements of ZrB_2 and SiC grain lengths as described in the earlier section 6.2. There was no verified directional elongation along length, as shown in Figure 6.10. ZrB_2 grains were about 2 ± 0.5 μm and the SiC grains were about 1.5 ± 0.5 μm in size.

The absence of grain elongation along the stress direction indicates the creep mechanism is not associated with intragranular flow or diffusion. While the small stress exponent indicates Newtonian flow, the secondary electron microscope images did not show observable cavitation or macroscopic amounts of glassy phase. Therefore it is not clear at this point as to what the main deformation mechanism is. Transmission Electron Microscopy (TEM) studies to investigate the grain boundaries will be required. But the scope of this project was to develop a technique that could perform creep tests at very high temperatures with similar results as a conventional flexure test, which was accomplished.

6.5.1 Eutectic Melting in ZrB_2-SiC:

Creep tests were not successful above a surface temperature of 2210 °C due to eutectic melting of the ZrB_2-SiC. Despite the high melting temperatures of the UHTC ZrB_2 (3246 °C), addition of SiC lowers the melting point of the composite by almost 1000 °C to 2270 °C. A phase diagram calculated by Kauffman [16] shows a eutectic in the ZrB_2 –SiC system at 2270 °C around 54 wt% ZrB_2. (Figure 6.11)

Above this eutectic temperature, these ZrB_2 -30vol% SiC composites should consist of proeutectic ZrB_2 solid with about 40% eutectic liquid. Figure 6.12 shows the microstructure in the sample heated to a surface temperature of 2210 °C and cooled down to room temperature. It displays a classic eutectic microstructure with lamellar eutectic zirconium diboride grains about 1 μm in thickness in a SiC matrix. Some of the ZrB_2 grains were still intact while many of them seem to have been partially reacted with the eutectic. All the SiC grains have lost their shape definition, suggesting that they were melted in the eutectic liquid. The melting caused the ribbon to rupture, ceasing current flow for the resistive heating. So while EMMA is capable of creep testing UHTCs at higher temperatures, it is the specimen melting which prevents creep testing at temperatures near the eutectic point.

6.6. Summary

The microstructure of post creep ZrB_2-30 %SiC specimens tested using EMMA at ultra high temperatures was studied for understanding the effect of oxidation as well as evidence of damage from mechanical loads.

Specimens tested in oxidative environment (ambient air) showed extensive oxidation resulting in complex oxide scales composed of an outer layer of Silica and Zirconia underneath which is a porous ZrB_2 layer formed from selective oxidation of SiC. The microstructure of the oxide layers was comparable to conventionally furnace tested specimens studied by other researchers. Cracking and delamination were observed in these oxide scales between the outer Zirconia layer and the inner porous ZrB_2 layer. They were discovered to originate from the phase transformation of Zirconia formed in tetragonal during high temperature of testing to monoclinic crystal structure during the cool down. Specimens tested in the environmental chamber in non-oxidative environment (Nitrogen and 0.25% O_2) confirmed oxidation suppression. No oxide scales were observed. Only a 5 μm thin outer layer of ZrB_2 was observed resulting from small amount of active oxidation of SiC from surface.

Investigation of inner microstructure of unreacted material was done through axial and transverse cross sections. No evidence of damage such as cracks or fissures was discovered. Grain size measurements comparing the grain length along the loading direction (length) with grain length along non-strain direction (thickness) were done. The

material showed no elongation of ZrB_2 or SiC grains in these specimens deformed to 1% strain and at very high temperatures 2100 °C. But the specimens tested above 2200 °C showed excessive damage from melting. The microstructure showed lamellae structures and pro-eutectic ZrB_2 grains indicating eutectic melting which was corroborated through the phase diagram of the ZrB_2-SiC composite. EMMA is capable of creep testing UHTCs at temperatures > 2200 °C but the test specimen composed of ZrB_2-SiC melted at these extreme temperatures.

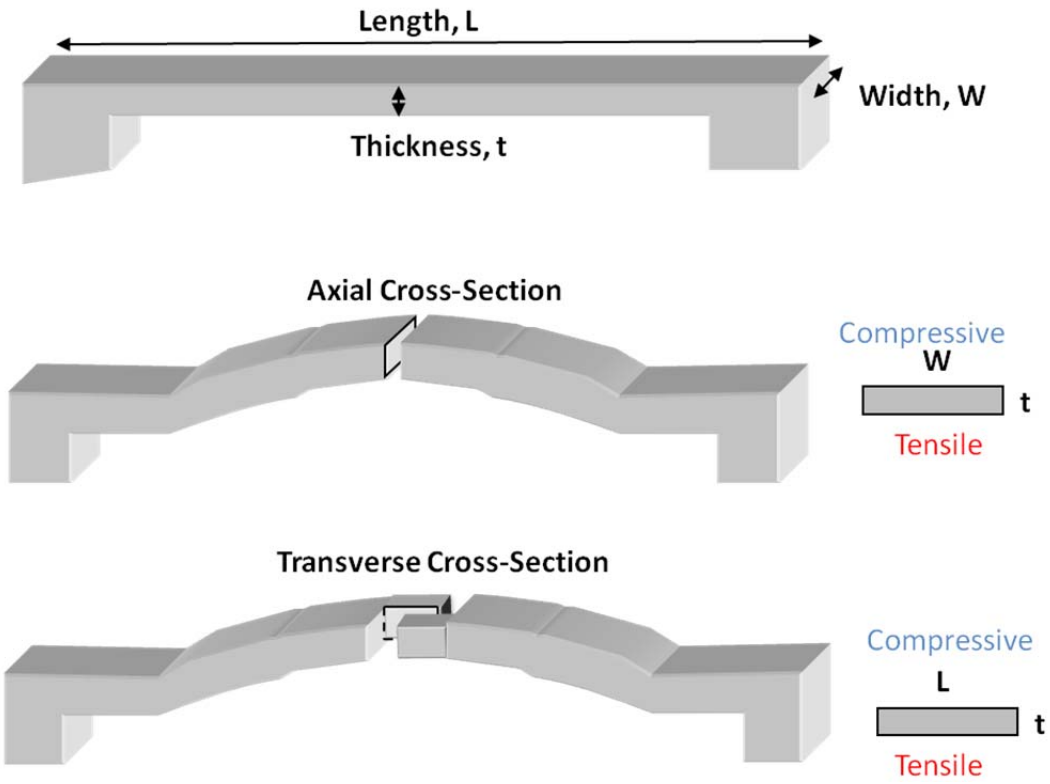

Figure 6.1: Schematic of axial and transverse cross sections in the ribbon sample

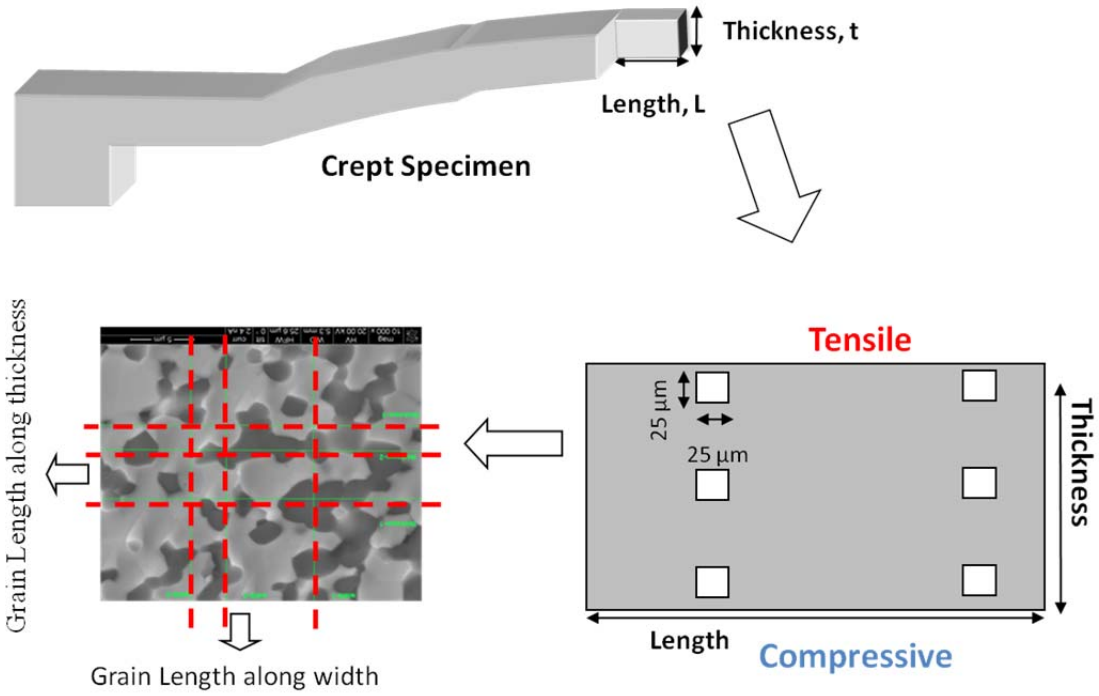

Figure 6.2: Schematic of post-creep specimen sectioned for study of interior microstructure and grain size measurements

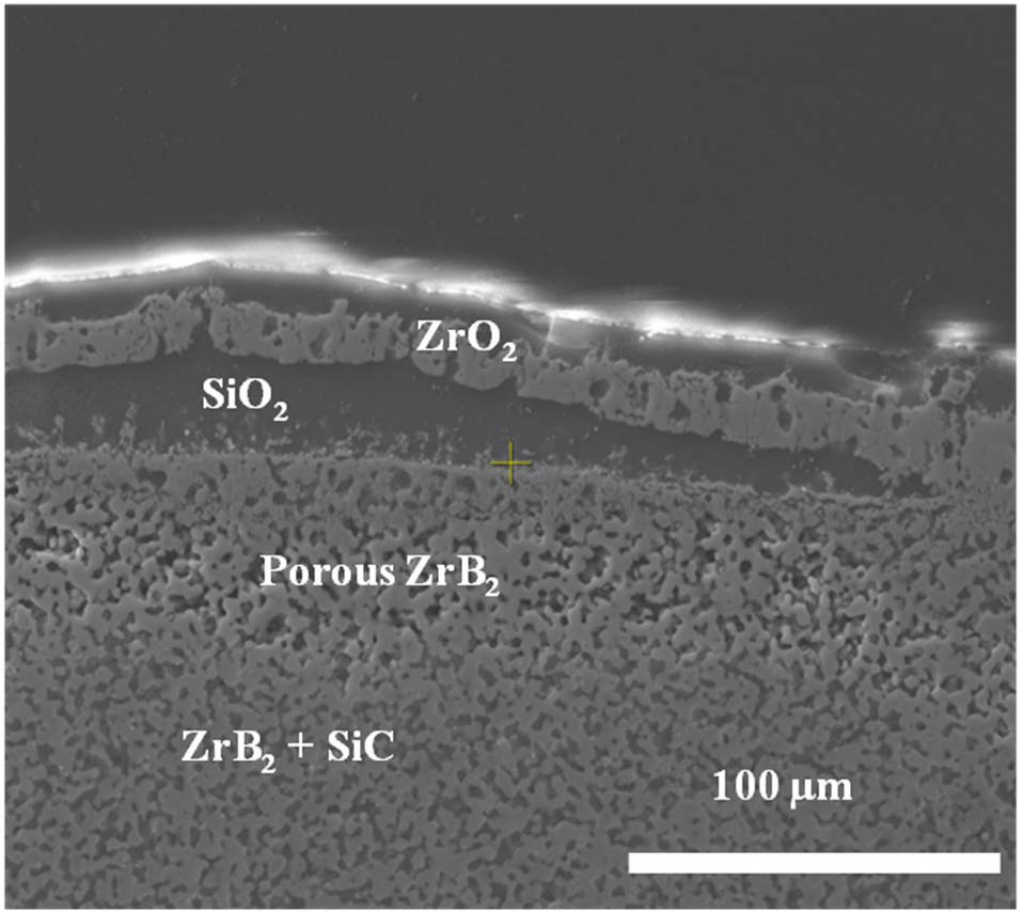

Figure 6.3: Secondary electron image of the oxide scale in a specimen creep tested at 1800 C under 38 MPa stress in Air for 300 seconds to a creep strain of 0.37%.

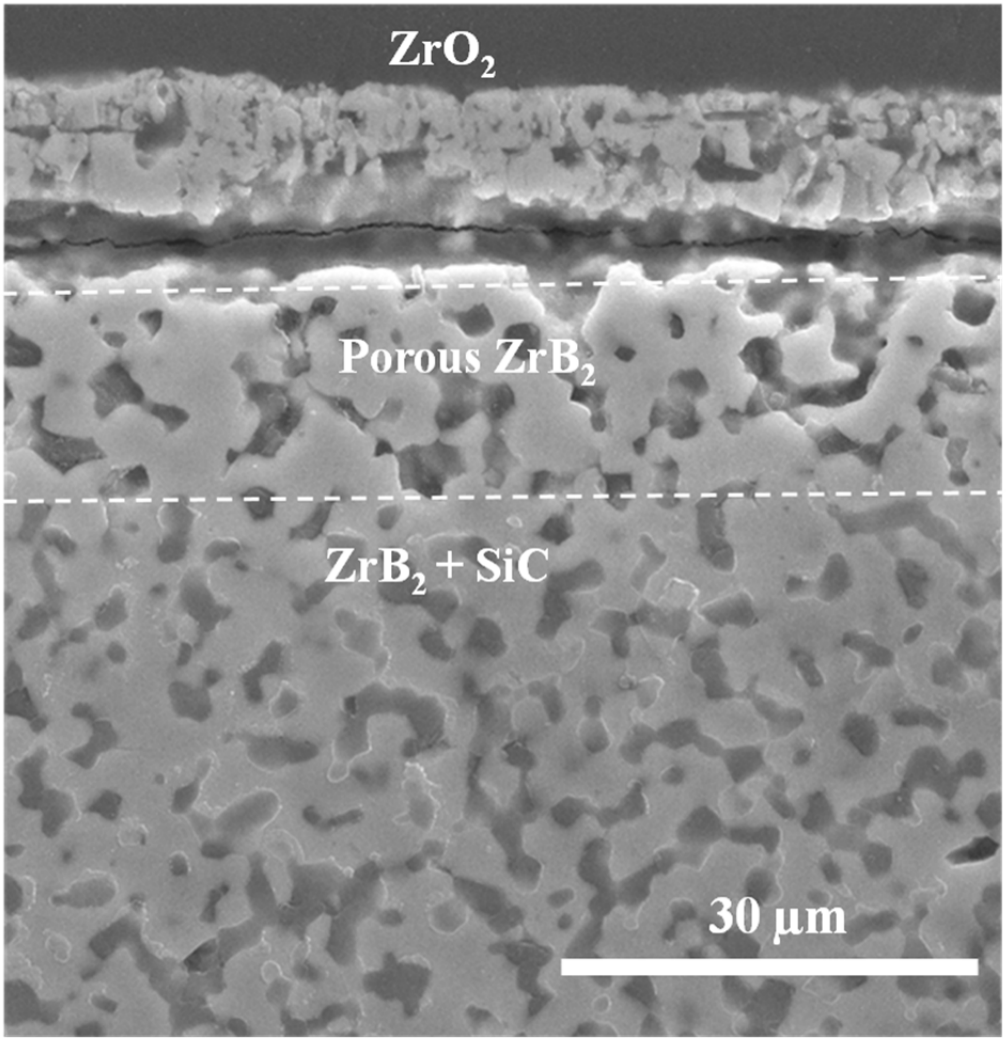

Figure 6.4: Cracks between ZrO_2 and porous ZrB_2 oxide scales of sample creep tested in air at 1700 °C under 30 MPa stress to a final strain of 0.445%.

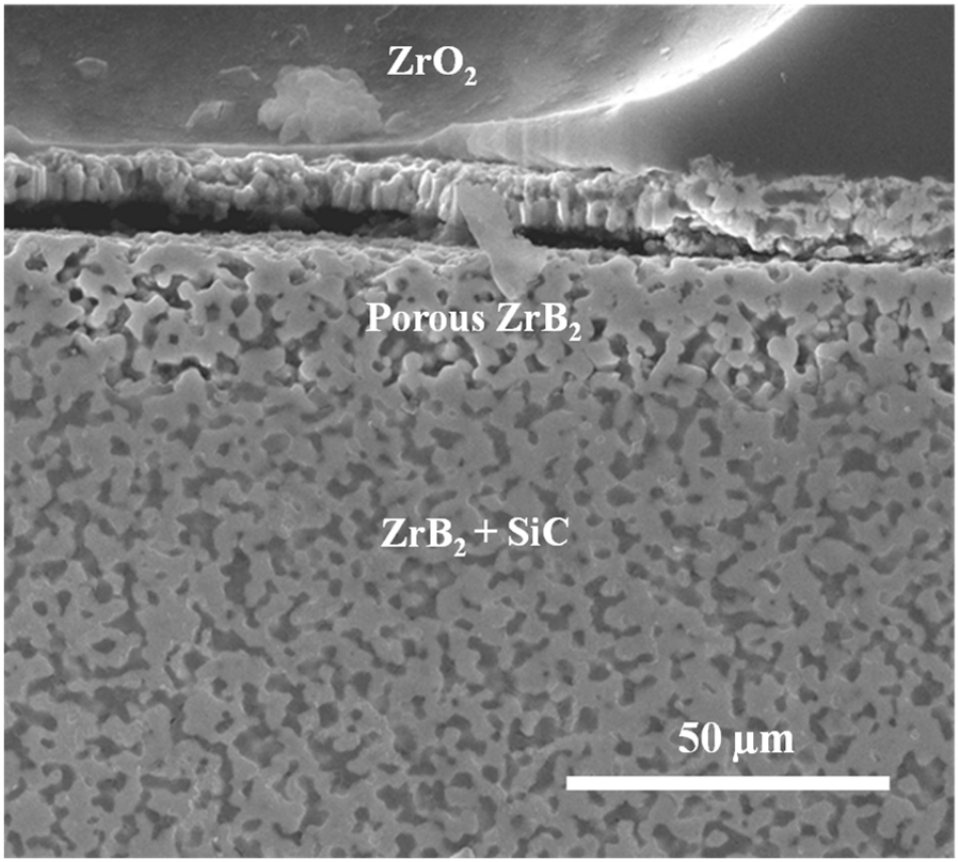

Figure 6.5: Cracks developing into delamination in the sample resistively heated in air to 2000 °C for 10 seconds

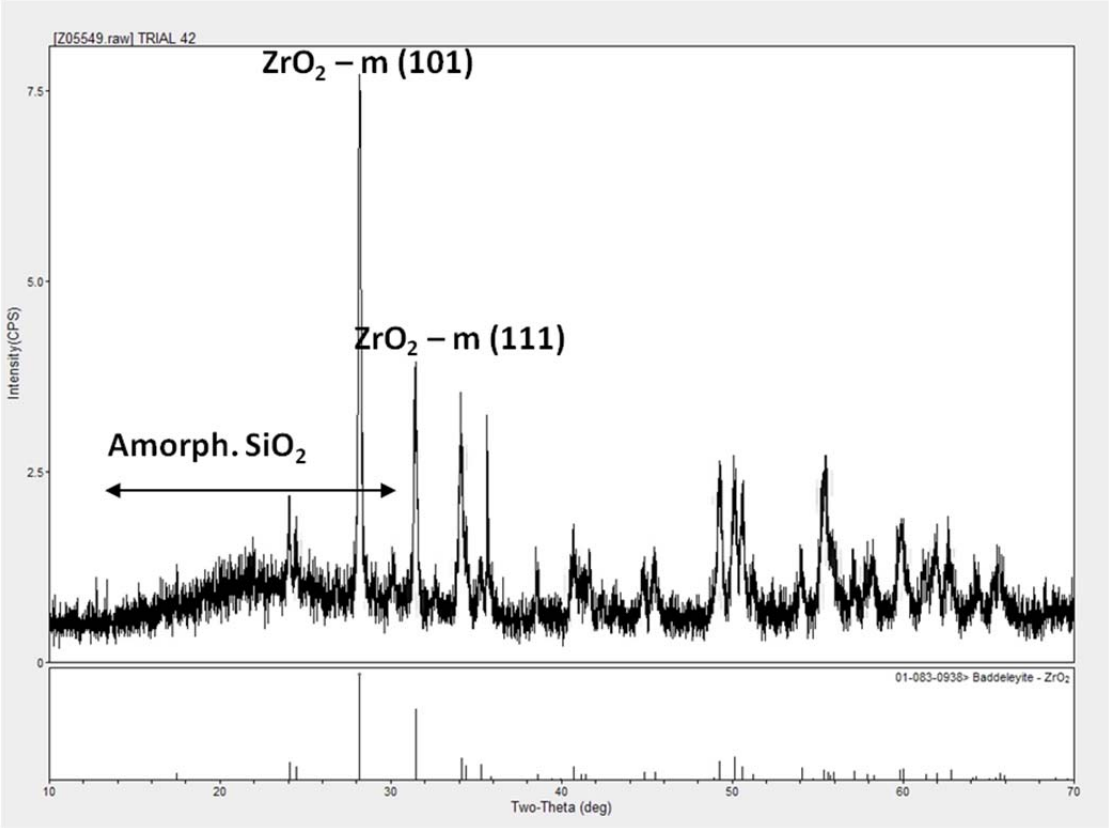

Figure 6.6: X-Ray Diffraction pattern of the surface of the oxide scale of a sample creep tested in air

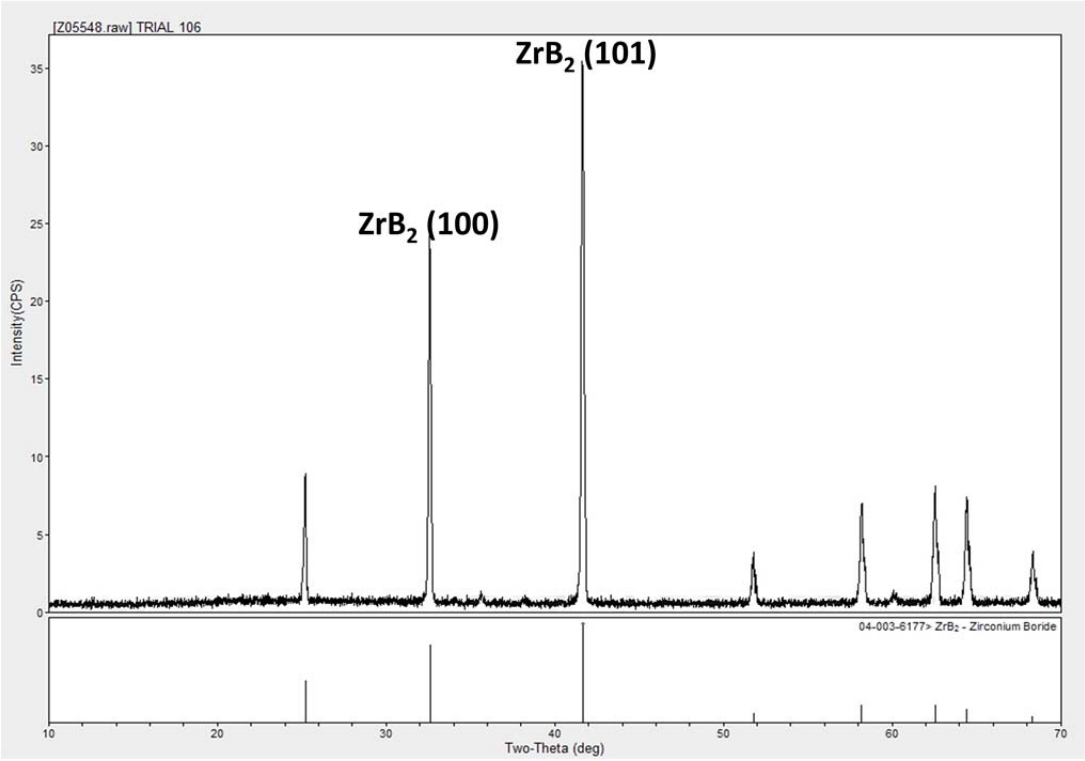

Figure 6.7: X-Ray Diffraction pattern of the surface of the sample creep tested in reduced oxygen atmosphere

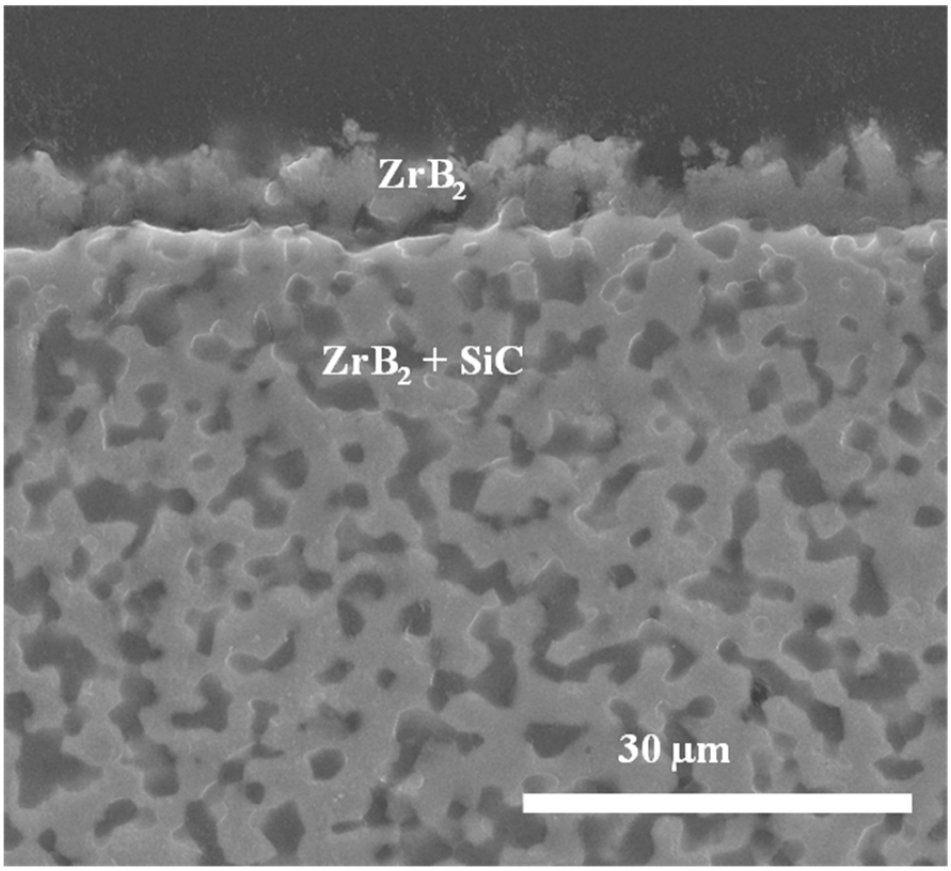

Figure 6.8: Specimen tested at 2000 °C under 50 MPa stress for 75 seconds to a final strain of 0.86% in air with 0.25% O_2.

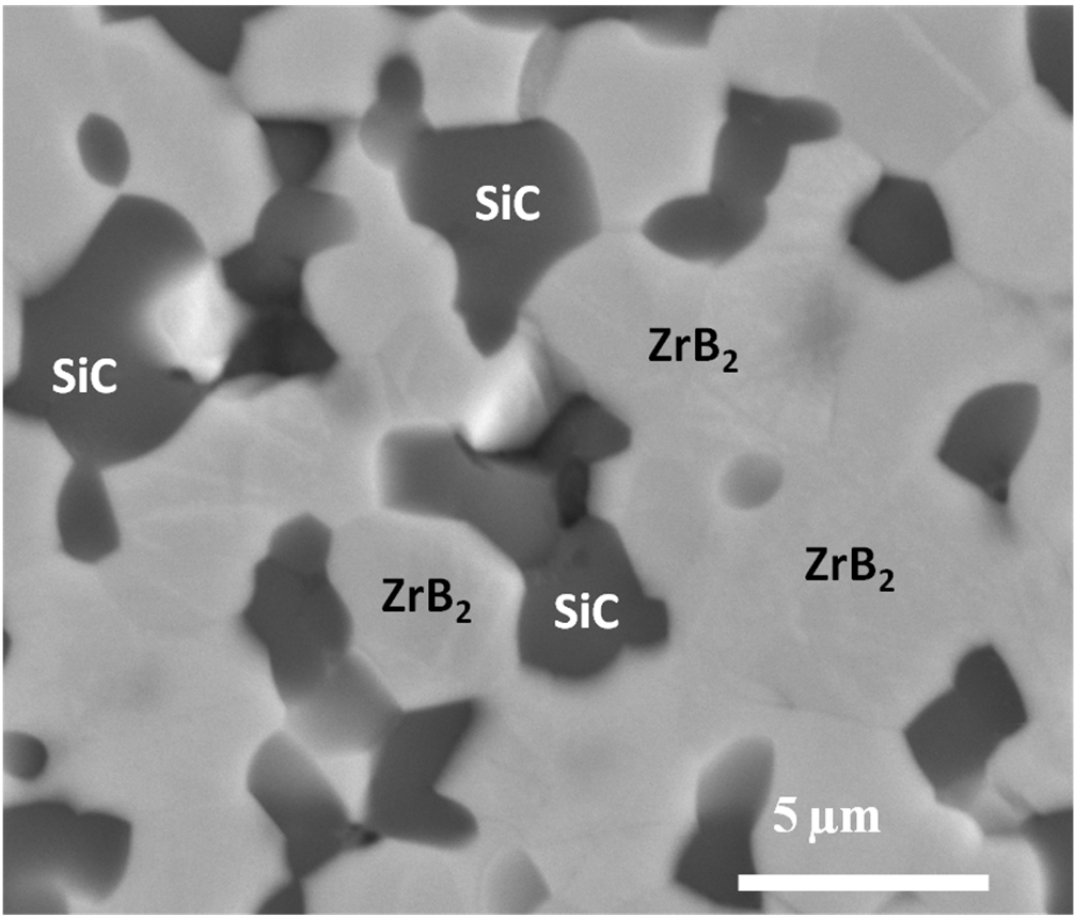

Figure 6.9: Secondary electron image of the cross section of sample creep tested at 2000 °C under 50 MPa stress in 0.25% O_2 to a final strain of 0.86% near tensile surface shows no damage in ZrB_2 or SiC grains

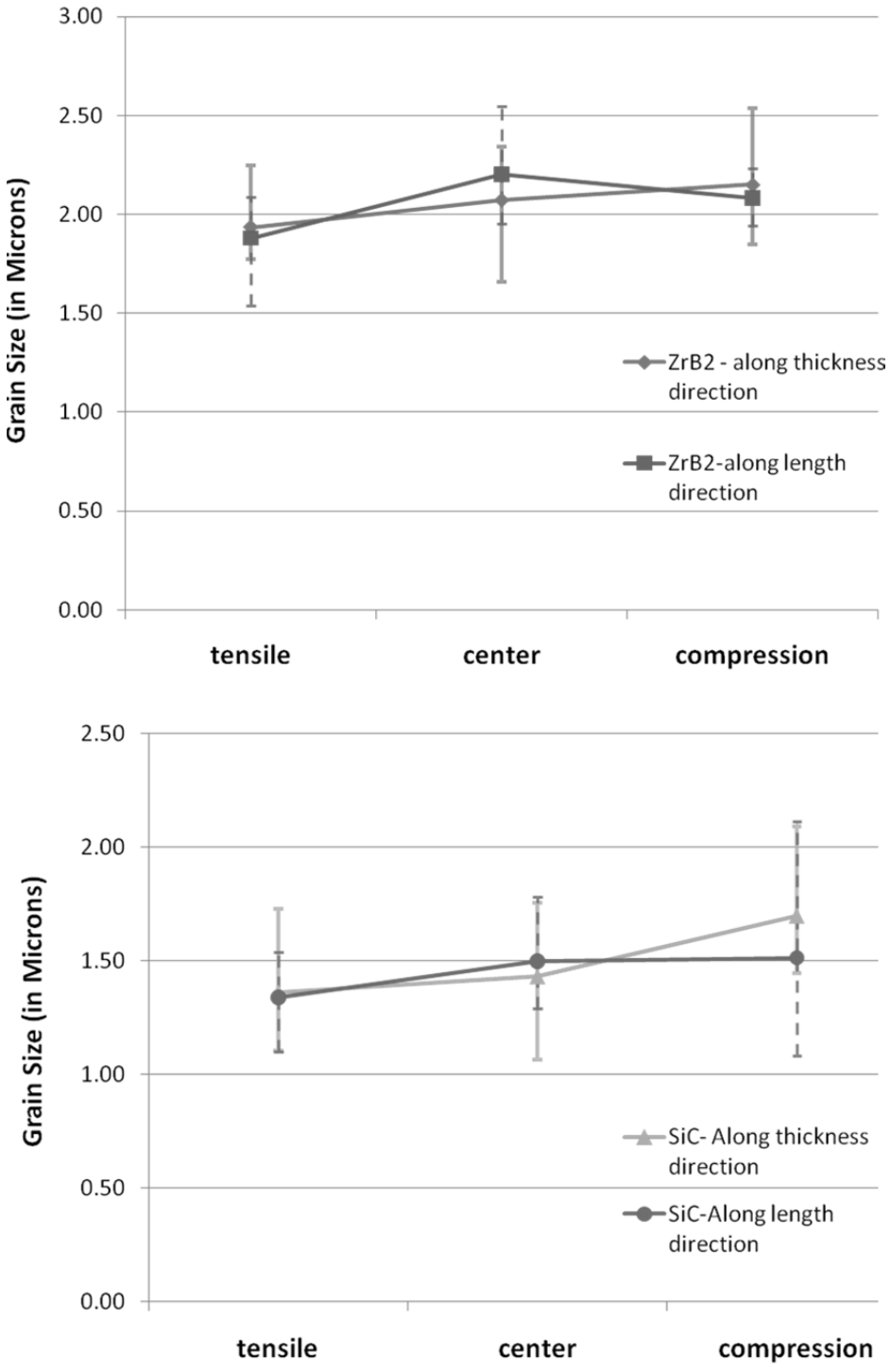

Figure 6.10: Grain lengths of ZrB_2 and SiC grains along thickness and length directions in tensile, center and compressive regions of the flexure.

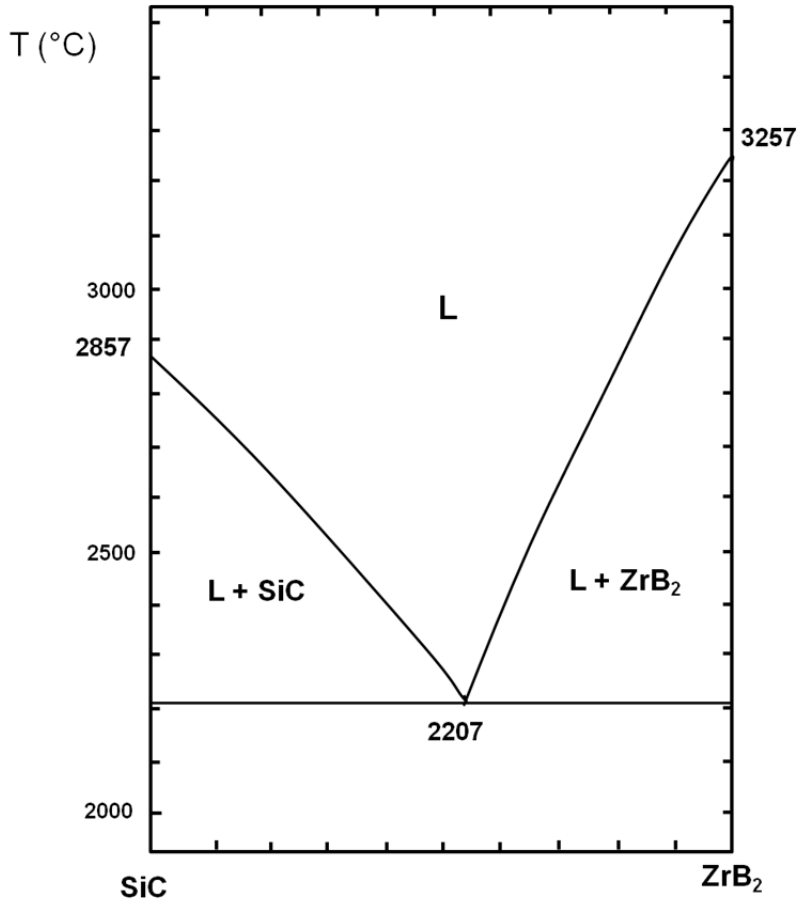

Figure 6.11: Eutectic in the ZrB2-SiC Phase Diagram at 2207 °C

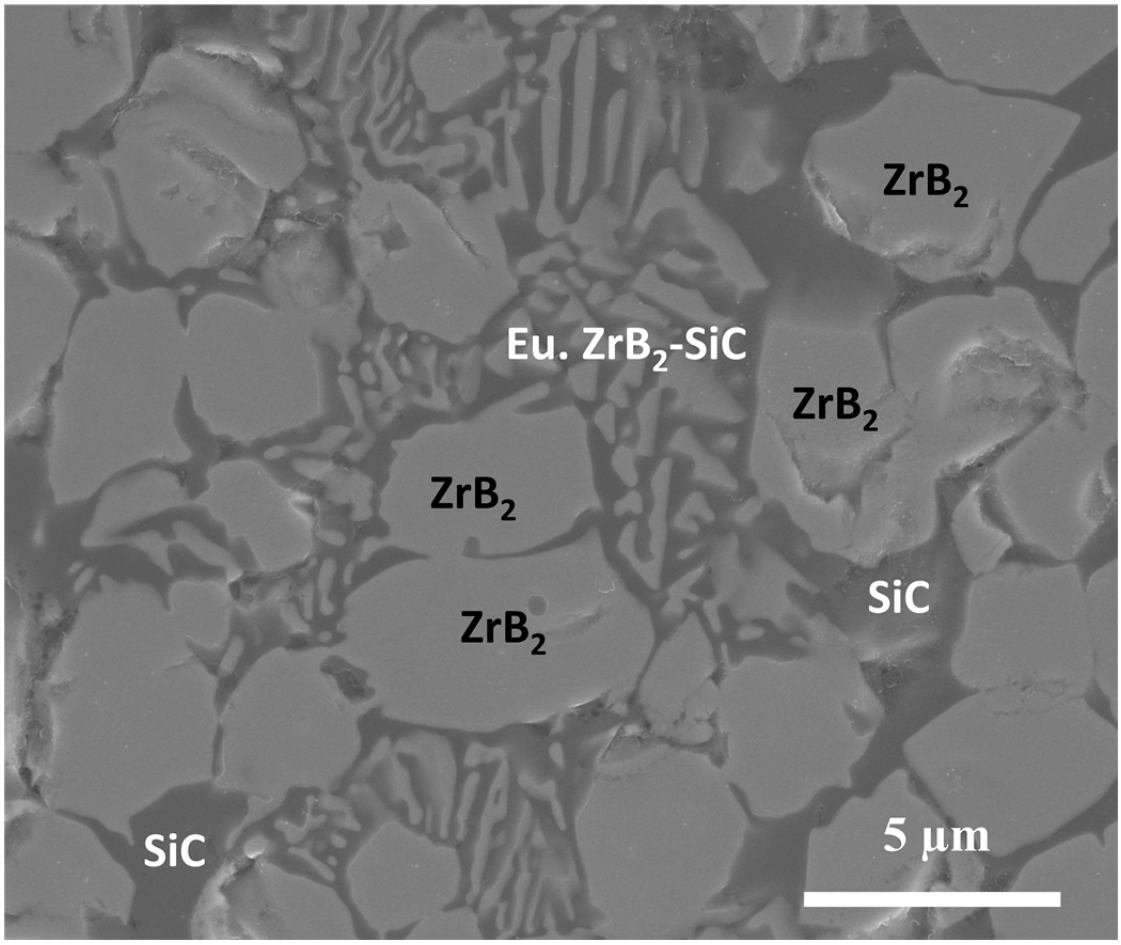

Figure 6.12: Secondary electron image of the lamellar microstructure from eutectic melting at 2210 °C.

Table 6.1: ZrB_2 and SiC grain size measurements in Transverse cross section of sample 2000 °C under 50 MPa stress in 0.25% O_2 with a final strain on 0.86%.

ZrB2				
	direction	Avg	Max	Min
tensile	thickness	1.93	2.25	1.77
	Length	1.88	2.07	1.74
center	thickness	2.07	2.34	1.66
	Length	2.20	2.65	1.72
compression	thickness	2.15	2.54	1.85
	Length	2.08	2.29	1.84
SiC				
	direction	Avg	Max	Min
tensile	thickness	1.36	1.73	1.11
	Length	1.34	1.54	1.10
center	thickness	1.43	1.75	1.06
	Length	1.50	1.78	1.29
compression	thickness	1.69	2.09	1.44
	Length	1.51	2.11	1.08

References

1. F. Lofaj, S. M. Wiederhorn "Creep processes in Silicon Nitride ceramics", *J. Ceram. Pro. Res.*, 10 [3] 269-277 (2009).

2. S. M. Wiederhorn, B. J. Hockey and J. D. French "Mechanism of Deformation of Silicon Nitride and Silicon Carbide at High Temperatures", *J. Eur. Ceram. Soc*., 19 [13-14] 2273 - 2284 (1999).

3. K. M. Fox and J .R. Hellmann "Microstructure and Creep Behavior of Silicon Nitride and SiAlONs" *Int. J. Appl. Technol.,* 5 [2] 138-154 (2008).

4. I.G. Talmy, J.A. Zaykoski, M. M. Opeka, S. Dallek, "Oxidation of ZrB_2 ceramics modified with SiC and Group IV-VI transition metal diborides" Proceedings of the International Symposium on "High Temperature Corrosion and Materials Chemistry III" edited by M. McNallan and E. Opila, *The Electrochemical Society*, 12, p.144 (2001).

5. W.C. Tripp, H.H. Davis, and H.C. Graham, "Effect of SiC addition on Oxidation of ZrB2", *Am. Ceram. Soc. Bull*., 52 [8] 612-616 (1973).

6. I.G. Talmy, J.A. Zaykoski, C.A. Martin, "Flexural Creep Deformation of ZrB2/SiC Ceramics in Oxidizing Atmosphere", *J. Am. Ceram. Soc*., 91 [5] 1441–1447 (2008).

7. W. L. Vaughn, H.G. Maahs, "Active –to- Passive Transition in the Oxidation of Silicon Carbide and Silicon Nitride", *J. Am. Ceram. Soc.*, 73 [6] 1540-1543 (1990).

8. S. N. Karlsdottir, J.W. Halloran, F. Montervede, A. Bellosi "Oxidation of ZrB_2-SiC: Comparison of Furnace Heated Specimens and Self-Heated Ribbon Specimens" *Mechanical Properties and Performance of Engineering Ceramics and Composites III* (eds E. Lara-Curzio, J. Salem and D. Zhu), John Wiley & Sons, Inc., Hoboken, NJ, USA. (2008).

9. W. G. Fahrenholtz, "Thermodynamic Analysis of ZrB_2–SiC Oxidation: Formation of a SiC-Depleted Region", *J. Am. Ceram. Soc*, 90: 143–148. (2007).

10. A. Rezaie, W.G. Fahrenholtz and G.E. Hilmas "Evolution of Structure during the Oxidation of Zirconium Diboride – Silicon Carbide in Air upto 1500 °C", *J. Eur. Ceram. Soc*., 27 2495-2501 (2007).

11. T. K. Gupta, J.H. Bechtold, R.C.Kuznicki, L.H.Cadoff and B.R. Rossing, "Stabilization of tetragonal phase in polycrystalline zirconia", *J. Mat. Sci.*, 12[12] 2421-2426 (1977)

12. H. Toraya, M. Yoshimura, and S. Somiya "Calibration Curve for Quantitative Analysis of the Monoclinic-Tetragonal ZrO_2 System by X-Ray Diffraction" *J. Am. Ceram. Soc* 67: C-119–C-121. (1984)

13. H.F. Poulsen, J. Neufeind, H.B. Neumann, J.R. Schneider and M.D. Zeidler, "Amorphous silica studied by high energy X-Ray Diffraction", *J. Non-Crystalline Solids*, 188[1-2] 63-74 (1995)

14. L .Zhang, D.A. Pejakovic and J. Marschall "Thermal and Electric Transport Properties of Spark Plasma Sintered HfB_2 and ZrB_2 Ceramics", *J. Am. Ceram. Soc* 94[8] 2562-2570 (2011)

15. F. Lofaj, S. M. Wiederhorn, G. G. Long, B. J. Hockey, P. R. Jemian, L. Browder, J. Andreason, U. Taffner "Non-cavitation tensile creep in Lu-doped silicon nitride", *J. Eur. Ceram. Soc* 22 2479-2487 (2002)

16. L. Kauffman, "Calculation of Multicomponent Refractory Composite Phase Diagrams", Manlabs, Cambridge MA Final rept. Naval Surface Weapons Center, NSWC TR-86-242, ADA192293, 1 June 1986.

Chapter 7

CONCLUSION

7.1. Summary

A novel method for non-contact mechanical testing was designed and built for testing ultra-high temperature ceramics at high temperatures close to their application environment in hypersonic and supersonic vehicle leading edges and thermal protection barrier. The methodology is very rapid, low cost, and enables testing at the highest temperatures recorded in the literature. A miniaturized self-supported ribbon specimen is resistively heated to target test temperatures while applying a transverse magnetic field. The resulting electromagnetic Lorentz forces are utilized to apply stress and deform the miniature ribbon. This method was named, EMMA (Electro-Magnetic Mechanical Apparatus).

EMMA enables mechanical testing at temperatures as high as 2200 °C with a power input of only 200-300W and without creating a difficult-to-manage heat load in the surroundings due to the small size of the specimen. Moderate amounts of current (40-65 Amperes) are required to heat the electrically conducting UHTC material to high

temperatures. Poles of an electromagnet are placed on either side of this ribbon specimen to apply a magnetic field 0.3-0.5 Tesla perpendicular to the current direction. An electromagnetic force of ~ 25 N/m acts as a distributed load all over the length of the sample. With the ribbon dimensions of 37 mm length, 2 mm width and 0.3-0.4mm thickness, this distributed force applies a maximum flexural stress of ~50MPa on the outer fibers of the specimen.

The self-heated and self-supported design prevents contact of the specimen in the hot zone with foreign material. The electromagnetic forces are also invisible and non-contact in nature and therefore EMMA does not suffer from issues of contamination even while operating at high temperatures.

Due to nature of their origin, stresses in EMMA are dependent on the shape of the deformed ribbon specimen. Therefore the stresses dynamically vary as the specimen deforms. The behavior of the stresses and the deflection profile are studied using the Finite Element Method and discovered to reach a steady state very rapidly. The load reached a steady state instantly and the deflection profile remains constant in an elastic material. The behavior of a visco-elastic material such as in creep was predicted using Maxwell's model and the deflection profile had both instant deflection from elastic strain and time dependent linear deflection rate from plastic strain. The loading conditions in EMMA were proved to reach a steady state and remain constant and are therefore comparable to a regular loading fixture.

The total cost of the apparatus was approximately $25,000 and included several components of equipment which were either procured from vendors or custom designed. Major components include an Electromagnet which can attain a magnetic field of 1.5 Tesla, a Digital Gaussmeter to monitor magnetic flux density, a programmable power supply with a PID controller, an Infrared Pyrometer to measure the temperature and a violet Laser Micrometer to measure deflection *in situ* which were purchased from manufacturers. Other important components such as slide-in sample holder set up structure, sample holders, environmental chamber and its components were precision designed using Computer Aided Design (CAD) and custom machined.

A DC current is coupled with a DC magnetic field to generate a constant electromagnetic load and perform creep experiments. Tests were performed on ZrB_2-30vol% SiC composite at temperatures from 1600-2200 °C under stresses ranging from 20-50 MPa in ambient air as well as Nitrogen. The UHTCs are prone to oxidation in ambient atmosphere. Therefore to obtain pure material response, tests were conducted in a non-reactive atmosphere, Nitrogen. These experiments were conducted inside an environmental chamber designed to enclose the sample holder surroundings. There was a trace amount of remnant oxygen < 2500ppm sufficient to suppress oxidation. Significant deformations were observed in the long thin ribbon specimens even at relatively low strains 0.1-1%.

The creep data fitted well with the Norton-Arrhenius law, with strain rates ~10^{-6} at low temperatures to 10^{-4} at high temperatures. The activation energy of the ZrB_2-

30vol% SiC composite was found to be 319 kJ/mol in air and 344 kJ/mol in N_2. The other kinetic creep parameter, the stress exponent, was found to be 1.4. The creep in air and starved air were comparable, although the creep rates in air were slightly higher than their counterparts in N_2. But the true stresses in air will be higher due to formation of oxide scales at the surface which do not support loads and so the creep rates in air were corrected for these higher true stresses using the empirical stress exponent. The corrected air creep rates matched closely with the creep rates in N_2. The atmosphere of testing otherwise did not affect the creep behavior.

Validation of this creep data and EMMA as a technique was done through comparison of EMMA creep data with conventional 3-pt and 4-pt flexure creep data from other researchers. This comparison showed that the few data points other researchers had in our testing temperature range were similar and extrapolation of EMMA trend line to lower temperatures is also akin, thereby establishing EMMA as a functional technique for high temperature creep of UHTCs.

The microstructure of the post creep ZrB_2-30 %SiC specimens tested using EMMA at ultra high temperatures were studied to understand the effect of oxidation as well as evidence of damage from mechanical loads. Specimens tested in an oxidative environment (ambient air) showed extensive oxidation resulting in complex oxide scales composed of an outer layer of Silica and Zirconia underneath which is a porous ZrB_2 layer formed from selective oxidation of SiC. The microstructure of the oxide layers was comparable to conventionally furnace tested specimens studied by other researchers.

Cracking and delamination were observed in these oxide scales between the outer Zirconia layer and the inner porous ZrB_2 layer. It was discovered that the cracks originated from the phase transformation of Zirconia transforming from tetragonal to monoclinic crystal structure during the cool down. Specimens tested in the environmental chamber in non-oxidative environment (Nitrogen and 0.25% O_2) confirmed oxidation suppression. No oxide scales were observed. Only a 5 μm thin outer layer of ZrB_2 was observed resulting from small amount of active oxidation of SiC from surface.

Investigation of inner microstructure of unreacted material was done through axial and transverse cross sections. No evidence of damage such as cracks or fissures was discovered. Grain size measurements comparing the grain length along the loading direction (length) with grain length along non-strain direction (thickness) were done. The material showed no elongation of ZrB_2 or SiC grains in these specimens deformed to 1% strain and at very high temperatures 2100 °C. But the specimens tested above 2200 °C showed excessive damage from melting. The microstructure showed lamellae structures and pro-eutectic ZrB_2 grains indicating eutectic melting which was corroborated through the phase diagram of the ZrB_2-SiC composite. So while EMMA is capable of creep testing UHTCs at temperatures > 2200 °C, it was the specimen melting which prevented it.

7.2. Future Applications

7.2.1. Other Mechanical Tests with EMMA

In its current configuration EMMA is designed for creep testing. However, with small changes to the experimental set up, various other mechanical tests could be performed using this technique.

(a) Fast Fracture

The conventional method to determine strength vs. temperature is to conduct a series of isothermal fracture tests, where a set of specimens is fractured and the fracture strengths recorded as σ_f. Temperature dependence is obtained by running a set of tests at a few discrete temperatures. Since fracture strength data tends to be scattered, a large data set is needed for each temperature. This consumes many specimens, and much time since the sample and fixture is typically heated and cooled for each strength point. Sometimes, one attempts to discover the Wiebull parameters characterizing the strength distribution for each temperature, which is costly and tedious. Conventional strength data tend to be easier to obtain at lower temperatures (where it is less interesting), and increasingly difficult to obtain at very high temperatures (where it is most interesting), for the practical reason that very high temperature strength measurements are challenging and expensive.

With EMMA, it might be more convenient to select a number of magnetic flux values *B* and sample geometries (L^2/Yt^2) and increase current until the sample fractures, recording the measured temperature at fracture Θ_f and the calculated stress at fracture σ_f. With multiple samples, one maps out the strength vs. temperature behavior with multiple $\{\sigma_f,\Theta_f\}$ points, one from each specimen for each value of magnetic flux and sample geometry. The scatter in the $\{\sigma_f,\Theta_f\}$ surface contains the Weibull information, which might be extractable by deconvolution. The EMMA method emphasizes very high temperatures, and would make strength data more common for higher temperatures, and less common for lower temperatures, so it is a very good compliment for the conventional methodology.

(b) Fatigue

Fatigue is conventionally done by seeking the S-N-Θ surface, defining cycles to failure (N_f) as a function of applied stress (S) and temperature Θ. The conventional method determines N_f at several discrete levels of stress at several discrete temperatures. Fatigue experiments are tedious and expensive. With the EMMA method, fatigue experiments can be accomplished most easily using a constant magnetic flux and replacing the current DC current with an AC electrical current. For example, an ordinary 60 Hz AC current would produce 10^5 fully reversed stress cycles in about 28 minutes. A set of experiments at constant current, for a particular value of magnetic flux *B* and sample geometries (L^2/Yt^2), will determine the N_f from the time it takes to fracture a specimen at constant S and Θ. With a different set of *B* and/or geometry, one gets N_f at

another value of S for a given temperature. It might be possible to map out the S-N-Θ with fewer specimens in a shorter time. Elaborate power supplies can also be used for testing at higher frequencies or cyclic creep using DC + AC current.

(c) Elastic Modulus and Mechanical Damping

Much can be inferred from the real part the complex modulus E′ (storage modulus or Young's Modulus) and the imaginary part of the complex modulus E″ (loss modulus for mechanical damping), since the Young's modulus is itself a critical property while the loss modulus reports the high frequency creep/plasticity behavior. This can be easily measured by the standard impulse excitation technique, using electromagnetic impulse created by quickly moving a small but powerful permanent magnet near the hot ribbon. During the brief transit of the magnet, the sample will experience a pulsed magnetic flux, which creates a transient force which will excite vibrations of the ribbon. These vibrations could be detected remotely with a laser vibrometer, or with an acoustic microphone pickup, which can be interpreted with standard commercial software. From the vibration frequency one infers the storage modulus E′ and the loss modulus E″ is inferred from the damping of the vibration.

7.2.2 EMMA for Other Materials

The applicability of this technique for other high temperature metals and ceramics is studied using a viability criterion based on the creep deformation rate $\dot{D}$. Besides

allowing non contact testing at ultra high temperatures, EMMA also permits the tests to be very swift. The rapid heating and cooling rates associated with resistive heating and the high creep strain rates at temperatures close to the melting point, allow the time duration of a creep test in EMMA to be on the order of a few minutes.

$$\dot{D} > 1\ \frac{mm}{min} \sim 1.66\ \times 10^{-5}\ \frac{m}{s} \quad ----(1)$$

The deformation rate is directly related to the creep strain rate ($\dot{\varepsilon}$), as discussed in Chapter 2 section 2.4 Equation (9):

$$\dot{\varepsilon} = \frac{4.8\ t\dot{D}}{L^2}$$

and the creep rate equation is generally considered to be an Arrhenius function, Chapter 5 section 5.5 Equation (1):

$$\dot{\varepsilon} = A\ e^{\frac{-Q}{RT}}\sigma^n$$

So

$$\dot{D} = \frac{A\ e^{\frac{-Q}{RT}}\sigma^n\ L^2}{4.8\ t} \quad ----(2)$$

where L is the length of the sample, t is the thickness, Q is the apparent activation energy, T is the temperature, σ is the stress, n is the stress exponent and A is the creep rate constant. In EMMA, the current (I) is related to the temperature due to the resistive heating.

The relationship is given by heat transfer as in Equation (2) of Chapter 2 section 2.2.

$$I = \left[\frac{2\varepsilon\sigma_c}{\rho}(w^2 t)\right]^{1/2} T^2$$

where ε is emissivity, σ_c is Planck's constant, ρ is resistivity and w is the width of the sample. The stress from the electromagnetic load (σ) is related to current (I) and magnetic flux density (B), Equation (3) of Chapter 2 section 2.3.

$$\sigma = 0.25 \frac{L^2}{w\, t^2}\, [IB]$$

Inputting these into equation (2) above, the criterion term can be rewritten as,

$$\dot{D} = \frac{L^2}{4.8\, t}\; A\, e^{\frac{-Q}{RT}} \left\{ 0.25 \frac{L^2}{w\, t^2} \left[\left(\frac{2\varepsilon\sigma_c}{\rho} (w^2 t) \right)^{1/2} T^2 B \right] \right\}^n$$

$$> 1.66 \times 10^{-5}\, \frac{m}{s} \qquad ----(3)$$

For a given material in consideration, the material properties A, Q, ε, ρ are fixed while the terms L, t, w, T, B can be varied with rational limitations such as:

(a) The testing temperature $T < T_{m.p.}$, melting point of the material,

(b) $B \leq 1$ Tesla since higher Bs would require expensive superconducting magnets

(c) To have reasonable dimensions such as $L \leq 100$mm, $t > 100\mu$m etc.

So these three variables T, B and dimensions can be altered to verify whether a given material can fit the viability criterion.

Figure 7.1 plots a Temperature – Stress map where different high temperature ceramics and metals exhibit similar creep deformation rate of 1mm/min. The dimensions

and the magnetic flux B are maintained constant in this map. The point ZrB_2 with the larger marker is a real data point from creep testing in EMMA. [18] The creep data for the other materials is collected from literature [19-38] (referenced in detail in Table1). The creep rate at the test conditions required for EMMA is then attained using the measured creep rates and extrapolating it through *Q* and *n*.

There were three types of materials observed, those with similar creep rates as ZrB_2; some with faster creep rates that can be tested even at lower temperatures successfully; and some with slower creep rates that have to be tested at higher temperatures to observe the required deformation rate. Additionally there was another class of high temperature metals (relatively lower (~ 1200-1500 °C) compared to the other UHTCs) which had a large threshold stress, such as NiMoNic which can also be tested in EMMA.

The materials with slower creep can be tested at lower temperatures with similar strain rates but at higher stress levels – which can be attained by increasing the magnetic flux and/or length. Figure 7.2 shows the required length of the sample to achieve 1mm/min creep deformation rate at 1900 °C under the same 0.5 T magnetic field with same width and thickness, 2mm and 0.5mm respectively.

The material properties of the suitable materials that can be tested in EMMA and their corresponding test variables are presented in Table 1. This wide range of applicability makes EMMA a generalized high temperature characterization technique.

Especially when expensive metals like Rhenium, Hafnium are involved, traditional dog bone samples' cost is prohibitive and EMMA's small sample size becomes advantageous.

The major limitation with EMMA is the requirement that the test specimens be electrically conductive. High temperature materials which are semiconductors cannot be tested in EMMA because the current requirement to heat these materials to high temperatures is much smaller. The electromagnetic load coupled from current and magnetic field is also therefore very low and insufficient to perform mechanical tests.

For example, the SiC-SiC or C-C Ceramic Matrix Composites are of recent research interest for high temperature applications in turbine blades. However due to their nonconductive nature, they would not be suitable to test in EMMA. Figure 7.3 demonstrates this by comparing with the electrically conductive ZrB_2-SiC UHTC. This plot is calculated stress vs. temperature condition for ZrB_2-SiC composite of conductivity 100,000 S/cm or 10^7 /Ω-m. The C-C composite of conductivity 200S/cm and SiC-SiC CMC of conductivity 5 S/cm will have very low stresses at any given temperature owing to I-Temp-Load relation in the electromagnetic force.

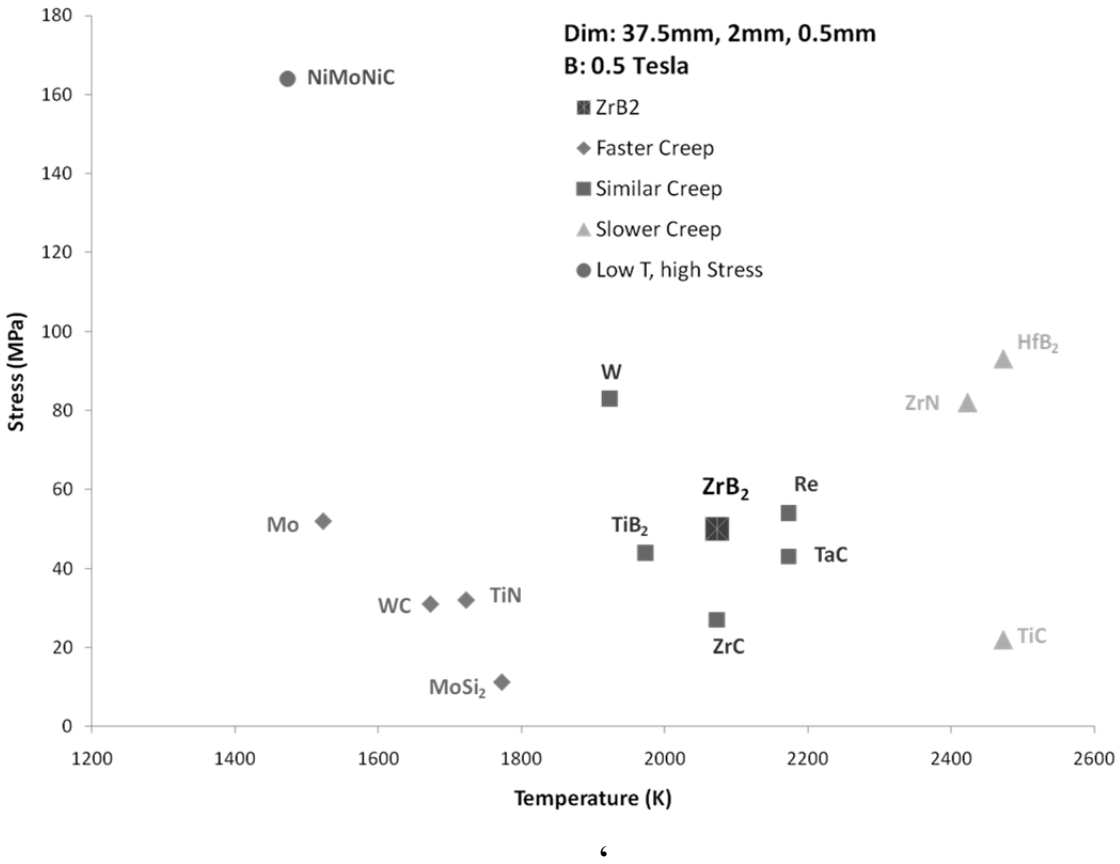

Figure 7.1: Temperature –Stress map for various high temperature ceramics and metals. The data relates the required temperature and stress conditions under which these materials will have a creep deformation rate of 1mm/min with fixed dimensions (37.5mm, 2mm, 0.5mm) and fixed magnetic field (0.5 Tesla).

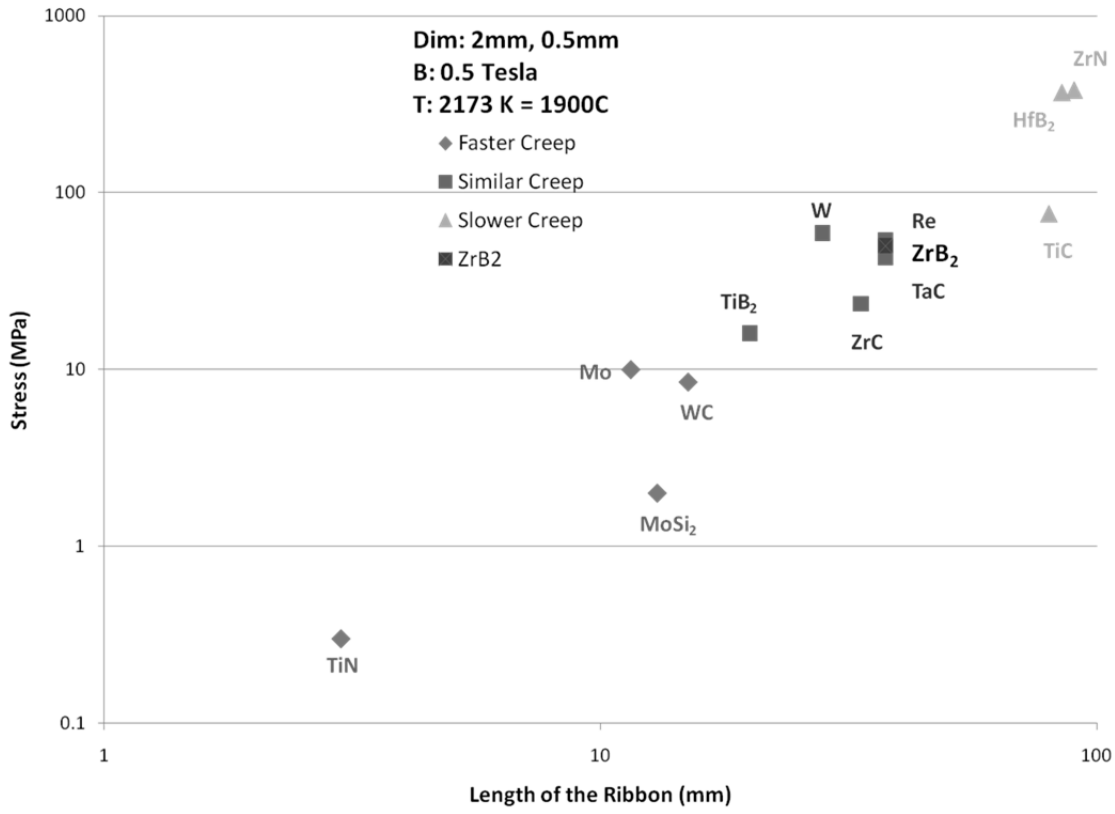

Figure 7.2: Sample Length–Stress map for 1mm/min creep deformation rate at 1900 °C with similar width (2mm) and thickness (0.5mm).

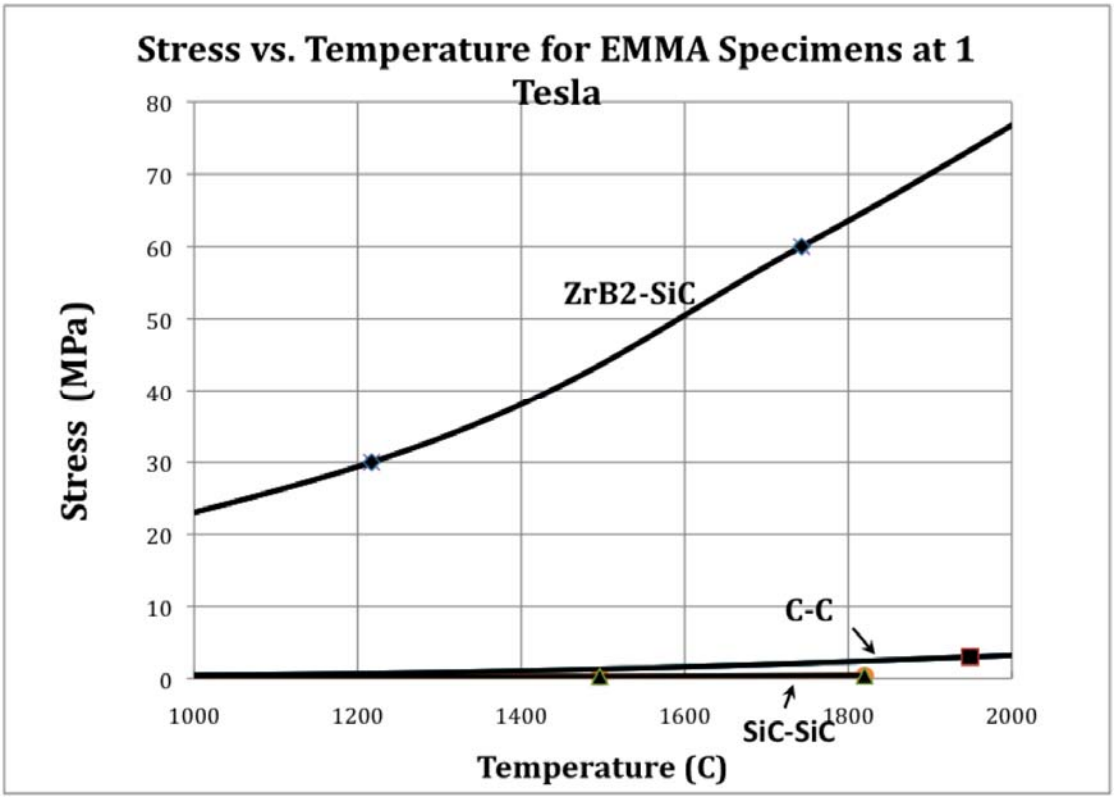

Figure 7.3: Comparison of Stress and Temperature conditions in EMMA for ZrB_2-SiC UHTC and C-C, SiC-SiC CMCs.

Table 7.1: The material properties and variable test conditions for the viability criterion to match the require 1mm/min deformation rate.

	MATL PROPERTIES				DIMENSION (mm)		TEST CONDITNS				Strain & Defm RATE		
	T_{mp} (K)	ρ (Ω-m)	Q (kJ/mol)	n	L	t	I (A)	B (T)	T (K)	σ (MPa)	$\dot{e}$ (1/s)	d' (mm/min)	
ZrB2	3313 [1]	2.0E-07	150	1.5	37.5	0.5	62	0.5	2073	50	3.7E-05	1.31	
Mo	2896 [7]	5.0E-08 [20]	440 [10]	5.1 [10]	37.5	0.5	148	0.5	1523	52	4.5E-05	1.6	FASTER CREEP
WC	3003 [1]	2.0E-07 [5]	217 [17]	1.3 [17]	37.5	0.5	89	0.5	1673	31	2.3E-05	0.83	
TiN	3223 [1]	2.2E-07 [1]	509 [13]	0.5 [13]	37.5	0.5	90	0.5	1723	32	2.8E-05	0.98	
MoSi2	2303 [4]	2.0E-06 [4]	433 [8]	1.9 [8]	37.5	0.5	31	0.5	1773	11.2	3.1E-05	1.09	
W	3695 [1]	5.0E-08 [1]	380 [11]	6.5 [11]	37.5	0.5	236	0.5	1923	83	2.9E-05	1.02	SIMILAR CREEP
TiB2	3253 [1]	2.0E-07 [4]	579 [15]	2 [15]	37.5	0.5	124	0.5	1973	44	3.2E-05	1.14	
ZrC	3813 [1]	6.5E-07 [3]	500 [14]	5 [14]	37.5	0.5	76	0.5	2073	27	1.9E-05	0.69	
TaC	4153 [1]	3.0E-07 [1]	710 [17]	3 [17]	37.5	0.5	123	0.5	2173	43	3.0E-05	1.05	
Re	3459 [7]	1.9E-07 [20]	300 [9]	3.5 [9]	37.5	0.5	155	0.5	2173	54	2.8E-05	0.99	
TiC	3623 [1]	2.0E-06 [4]	460 [16]	1 [16]	37.5	0.5	62	0.5	2473	22	3.6E-05	1.27	SLOWER CREEP
ZrN	3253 [1]	1.3E-07 [1]	588 [16]	1 [16]	37.5	0.5	232	0.5	2423	82	2.9E-05	1.05	
HfB2	3373 [1]	1.1E-07 [1]	500 [19]	1 [19]	37.5	0.5	264	0.5	2473	93	3.8E-05	1.3	
Nimo-nic 8A	1638 [6]	1.3E-06 [2]	462 [12]	4 [12]	75	0.3	21	1	1473	164	1.5E-05	3.6	

References

1. C.C. Wang, S.A. Akbar, W. Chen and V.D. Patton "Review: Electrical properties of high-temperature oxides, borides, carbides and nitrides", *J. Mat. Sci.*, 30, 1627-1641 (1995)

2. B. Roebuck, M.S. Loveday, M. Brooks, "Characterisation of Nimonic 90 by the use of miniaturized multiproperty mechanical and physical tests", *Int. J. Fat.,* 30, 345-351 (2008)

3. L. N. Grossman, "High-Temperature Thermophysical Properties of Zirconium Carbide", *J. Am. Ceram. Soc.*, 48[5] 236-242 (1965)

4. B. Basu, G.B. Raju and A.K. Suri " Processing and properties of monolithic TiB2 based materials", *International Mater Rev.,* 51[6] 353-374 (2006)

5. C. Kittel, "Introduction to Solid State Physics", Wiley-India, (1995)

6. M.J. Donachie, S.J. Donachie " Superalloys: A Technical Guide", ASM International – Technology and Engineering p.325 (2002)

7. Hammond, C. R. "The Elements, in Handbook of Chemistry and Physics" *81st ed*. CRC press (2004)

8. K. Sadananda, C.R.Feng and H. Jones," Creep of Molybdenum Disilicide composites", *Mat. Sci. & Engg.,* A155, 227-239 (1992)

9. W.R. Witzke and P.L. Raffo, "Creep Behavior of Electron-Beam-Melted Rhenium", NASA TN D-6291.

10. H. Clauer, B.A. Wilcox and J.P. Hirth, " Creep Behavior of Molybdenum Single Crystals", *Acta Metallurgica*, 18, 367-379 (1970)

11. S. L. Robinson and O.D. Sherby " Mechanical Behavior of Polycrystalline Tungsten at Elevated Temperature", *Acta Metallurgica*, 17, 109-125 (1969)

12. K.R. Williams and B. Wilshire "On the Stress- and Temperature – Dependence of Creep of Nimonic 80A", *Metal Sci Jounrnal*, 7, 176-179 (1973)

13. Yu. G. Gogotsi and G. Grathwohl “Creep of Silicon Nitride- Titanium Nitride Composites” *J. Mat. Sci*, 28, 4279-4287 (1993)

14. D. W. Lee and J.S. Haggerty, “Plasticity and Creep in Single Crystals of Zirconium Carbide”, *J. Am. Ceram. Soc.*, 52[12] 642-647 (1969)

15. M.S. Koval’chenko, L.F. Ochkas and V.B. Vinorkurov, “Hot Pressing of Binary Titanium-Chromium Diboride”, *Poroshkovaya Metallurgiya*, 5(209) 69-72 (1980)

16. I.I. Spivak, R.A.Andrievskii, V.V. Klimenko and V.D. Lazarenko “Creep in the binary sytems TiB2-TiC and ZrB2-ZrN” *Poroshkovaya Metallurgiya*, 8(140) 17-21 (1974)

17. H.A. Johansen and J.G.Cleary “The Ductile-Brittle Transition in Tantalum Carbide”, *J. Elec. Chem. Soc.*, 113[4] 378-381 (1966)

18. J.T. Smith and J.D. Wood “Elevated Temperature Compressive Creep Behavior of Tungsten Carbide- Cobalt Alloys” *Acta Metallurgica*, 16, 1219-1226 (1968)

19. D. Kalish, E.V. Clougherty and K. Kreder” Strength, Fracture Mode and Thermal Stress Resistance of HfB2 and ZrB2”, *J. Am. Ceram. Soc.*, 52[1] 30-36 (1969)

20. J. F. Shackelford and W. Alexander “Electrical Properties of Materials”, Materials Science and Engineering Handbook © CRC Handbook (2001).